Monthly Notices
of the
ROYAL ASTRONOMICAL SOCIETY

MNRAS **481,** 749–792 (2018)
Advance Access publication 2018 August 9

doi:10.1093/mnras/sty2195

Thermodynamic profiles of galaxy clusters from a joint X-ray/SZ analysis

Jennifer A. Shitanishi,[1]★ Elena Pierpaoli,[1] Jack Sayers,[2] Sunil R. Golwala,[2] Silvia Ameglio,[1] Adam B. Mantz,[3] Tony K. Mroczkowski,[4] Elena Rasia[5] and Seth Siegel[2,6]

[1]*Department of Physics and Astronomy, University of Southern California, Los Angeles, CA 90089-0484, USA*
[2]*Division of Physics, Math, and Astronomy, California Institute of Technology, Pasadena, CA 91125, USA*
[3]*Kavli Institute for Particle Astrophysics and Cosmology, Stanford University, Stanford, CA 94305-4085, USA*
[4]*ESO - European Organization for Astronomical Research in the Southern hemisphere, Karl-Schwarzschild-Str. 2, D-85748 Garching b. Munchen, Germany*
[5]*INAF, Osservatorio Astronomico di Trieste, via Tiepolo 11, I-34131 Trieste, Italy*
[6]*Department of Physics, McGill University, 3600 Rue University, Montreal, QC H3A 2T8, Canada*

Accepted 2018 August 9. Received 2018 August 8; in original form 2017 December 14

ABSTRACT

We jointly analyse the Bolocam Sunyaev–Zel'dovich (SZ) effect and *Chandra* X-ray data for a set of 45 clusters to derive gas density and temperature profiles without using spectroscopic information. The sample spans the mass and redshift range $3 \times 10^{14}\,\mathrm{M}_{\odot} \leq M_{500} \leq 25 \times 10^{14}\,\mathrm{M}_{\odot}$ and $0.15 \leq z \leq 0.89$. We define cool-core and non-cool core subsamples based on the central X-ray luminosity, and 17 out of 45 clusters are classified as cool core. In general, the profiles derived from our analysis are found to be in good agreement with previous analyses, and profile constraints beyond r_{500} are obtained for 34 out of 45 clusters. In approximately 30 per cent of the cool-core clusters, our analysis shows a central temperature drop with a statistical significance of $>3\sigma$; this modest detection fraction is due mainly to a combination of coarse angular resolution and modest signal-to-noise ratio in the SZ data. Most clusters are consistent with an isothermal profile at the largest radii near r_{500}, although 10 out of 45 show a significant temperature decrease with increasing radius. The sample mean density profile is in good agreement with previous studies, and shows a minimum intrinsic scatter of approximately 10 per cent near $0.5r_{500}$. The sample mean temperature profile is consistent with isothermal, and has an intrinsic scatter of approximately 50 per cent independent of radius. This scatter is significantly higher compared to earlier X-ray-only studies, which find intrinsic scatters near 10 per cent, likely due to a combination of unaccounted-for non-idealities in the SZ noise, projection effects, and sample selection.

Key words: galaxies: clusters: intracluster medium – X-rays: galaxies: clusters.

1 INTRODUCTION

Characterization of the gaseous intracluster medium (ICM) is important to the study of both cosmology and galaxy cluster astrophysics. For instance, measurements of the redshift-dependent halo mass function at cluster scales have produced tight constraints on a range of cosmological parameters, and ICM observables have played a central role in nearly all such surveys to date (e.g. Vikhlinin et al. 2009; Mantz et al. 2010a; de Haan et al. 2016; Planck Collaboration XXIV 2016b). These measurements rely on an accurate and well-understood connection between ICM properties and underlying halo mass. For example, at fixed mass, what is the average shape and intrinsic scatter of the ICM thermodynamic profiles as a function of radius? The answer to this question is influenced by a range of complex physical processes, such as the radiative cooling and feedback from active galactic nuclei (AGNs) that tend to be important in the cluster core and the active accretion that occurs in the outer regions of the cluster (Nagai, Kravtsov & Vikhlinin 2007; Lau, Kravtsov & Nagai 2009). The relative contributions of these physical processes to clusters' thermodynamic states are currently not well known, but can be studied with measurements of ICM density, pressure, and temperature profiles.

The ICM gas in clusters has foremost been studied through X-ray observations. Imaging and spectroscopy provide density and temperature profiles, respectively (Sarazin 1988). As a supplement to X-rays, recent improvements in instrumentation have enabled ob-

★ E-mail: shitanis@usc.edu

servations of the Sunyaev–Zel'dovich (SZ) effect to provide meaningful constraints on the ICM. The signal is proportional to the integrated pressure along the line of sight and pressure profiles can therefore be determined directly from SZ effect observations (Plagge et al. 2010; Planck Collaboration V 2013; Sayers et al. 2013b, hereafter S13). Due to the different dependences of X-ray and SZ signals on gas density and temperature, combining X-ray surface brightness maps with SZ maps allows the simultaneous recovery of both physical quantities (Ameglio et al. 2007). Moreover, the weaker dependence of the SZ signal on density results in an observed brightness profile that falls more slowly with radius, which can often facilitate studies of a given cluster's outskirts.

There is a growing body of work based on joint X-ray and SZ fitting. Combining these multiwavelength data has yielded estimates of the cosmic distance scale (Bonamente et al. 2006) and smooth thermodynamic profiles (LaRoque et al. 2006). More recently, Eckert et al. (2013a) combined *ROSAT* gas density and *Planck* pressure profiles to find that entropy profiles continue to rise beyond $r_{200} \approx 1.5r_{500}$.[1] As another example, 'Joint Analysis of Cluster Observations' (JACO) was developed by Mahdavi et al. (2013) to combine X-ray, SZ, and weak lensing data to find cluster masses, and was most recently used on Cluster Lensing and Supernova survey with *Hubble* (CLASH) clusters to measure their mass and gas profiles (Siegel et al. 2018). In addition, X-ray and SZ surface brightness data have been combined to obtain precise thermodynamic profiles independent of X-ray spectroscopy in single clusters (Mroczkowski et al. 2009; Nord et al. 2009; Basu et al. 2010; Ruppin et al. 2017), in general finding good agreement with the spectroscopically derived results. Most recently, the *XMM–Newton* cluster outskirts project (X-COP) completed a joint analysis on the cluster Abell 2319 using *Planck* SZ maps and *XMM–Newton* X-ray surface brightness and spectroscopic measurements (Ghirardini et al. 2017).

In addition, numerous efforts, mainly using X-ray data, have been made to characterize the properties of ensemble-average thermodynamic profiles. Such analyses require clusters of different masses and redshifts to be scaled to a common reference, which is generally done based on the self-similar relations derived from the simplifying scenario of clusters forming from a purely gravitational spherical collapse (Kaiser 1986). These ensemble studies of many clusters can then show trends and/or scatter away from perfect self-similarity, thus revealing the degree to which non-gravitational physics occurs (e.g. departures from hydrostatic equilibrium).

For example, Vikhlinin et al. (2006) used *Chandra* exposures of 13 relaxed clusters at $z < 0.23$ to derive average density and temperature profiles. The density profile was found to be consistent with self-similarity with a scatter of approximately 15 per cent, while the temperature profile decreased beyond $0.2r_{500}$ and has even lower scatter. Leccardi & Molendi (2008), based on *XMM–Newton* exposures of a sample comprising both cool-core (CC) and non-cool-core (NCC) clusters at $z < 0.3$ with no evidence of recent merger activity, found an average temperature profile with a clear drop beyond $0.2r_{180} \approx 0.3r_{500}$ and an intrinsic scatter of 6 per cent . Eckert et al. (2012) used *ROSAT* to study 31 clusters at $0.04 < z < 0.2$, half CC clusters and the other half NCC. They found a 10–20 per cent scatter in the average density profile at intermediate radii, increasing to 30 per cent at $r_{200} \approx 1.5r_{500}$. McDonald et al. (2014), using *Chandra* observations of 80 clusters spanning a broad redshift range, compared results for cluster samples centred at $z = 0.46$ and $z = 0.82$. They found the higher redshift sample to have 30 per cent lower average temperatures near the core and a steeper drop in temperature at large radii. Morandi et al. (2015) stacked *Chandra* emission measure profiles of 320 clusters spanning a redshift range of $0.056 < z < 1.24$ to derive an average density and intrinsic scatter; they found a scatter of 20 per cent at r_{500}, which increases to 30 per cent at $r_{200} \approx 1.5r_{500}$. Mantz et al. (2016) constrained the mean density and temperature profiles and intrinsic scatters of a sample of 40 relaxed CC clusters using *Chandra* data, finding a temperature scatter of approximately 10 per cent at all radii. Furthermore, Bourdin et al. (2017) simultaneously fitted cluster pressure profiles to X-ray spectroscopic data and *Planck* SZ measurements, finding a 10 per cent intrinsic scatter within r_{500} and an increase at larger radii.

In sum, the small intrinsic scatters found in these and other observational studies indicate that cluster thermodynamic profiles are reasonably well approximated by a universal shape, at least for relatively relaxed clusters outside of the central core region. This conclusion is also supported by a range of numerical simulations (e.g. Nagai et al. 2007; Battaglia et al. 2012; Lau et al. 2015; Rasia et al. 2015; Biffi et al. 2017; Planelles et al. 2017). While this agreement is encouraging, simulations, while greatly improved recently, still cannot reproduce all of the small-scale physical phenomena that take place in the cluster core. In addition, the bulk of the observational constraints are focused on the inner regions of the cluster within r_{500}, although this situation is quickly changing (see, e.g., Bourdin et al. 2017; Ghirardini et al. 2017). Furthermore, at least one of the two primary X-ray telescopes used to study clusters (*XMM–Newton* and *Chandra*) has a significant spectral calibration bias (Schellenberger et al. 2015). Looking forward, joint SZ/X-ray analyses offer a promising tool to address the two latter issues. Specifically, they in general allow for studies to larger radii compared to analyses based solely on X-ray data, and they also allow for full thermodynamic constraints without the use of spectroscopic X-ray information.

In this work, we combine SZ images from Bolocam, a mm-wave bolometric imager that operated from the Caltech Submillimeter Observatory (CSO), with surface brightness maps from *Chandra*, NASA's flagship X-ray observatory, to recover density and temperature profiles for the BOXSZ sample of 45 clusters defined in Czakon et al. (2015). Markov chain Monte Carlo (MCMC) is used to fit smooth parametric models and a model consisting of concentric shells with uniform properties of the ICM density and temperature profiles of each cluster. In addition, sample mean profiles and the intrinsic scatter about these mean profiles are determined for both the full cluster sample and various subsamples. The standard flat lambda cold dark matter model is used, with $\Omega_m = 0.3$, $\Omega_\Lambda = 0.7$, and $H_0 = 70\,\mathrm{km\,s^{-1}\,Mpc^{-1}}$. The outline of the paper is as follows: Section 2 describes the cluster sample, Section 3 details the data reduction, and Section 4 reviews the modelling and fitting methods. Section 5 describes detailed consistency tests based on mock observations of smooth cluster models, Section 6 reviews the individual and joint cluster results, and Section 7 presents the overall conclusions.

2 CLUSTER SAMPLE

The Bolocam X-ray/SZ (BOXSZ) sample consists of 45 clusters observed by both Bolocam and *Chandra*, and Table 1 lists some important characteristics of the clusters. The sample includes the

[1] Throughout this paper, r_Δ denotes the distance at which the average density within is Δ times the critical density of the Universe at the redshift of the cluster.

Table 1. Observation information.

Cluster	z	r_{500} (Mpc)	M_{500} (10^{14} $M_\odot$)	NCC/CC	Disturbed	X-ray Obs ID	X-ray Exposure time (ks)	SZ S/N peak	SZ Obs time (hr)	r_{max} (r_{500})
Abell 2204	0.15	1.46 ± 0.07	10.3 ± 1.5	CC		6104	9.61	22.30	12.7	0.908
Abell 383	0.19	1.11 ± 0.06	4.7 ± 0.8	CC		2321	19.51	9.60	24.3	1.198
Abell 1423	0.21	1.35 ± 0.10	8.7 ± 2.0	NCC		538	9.87	5.80	11.5	1.182
Abell 209	0.21	1.53 ± 0.08	12.6 ± 1.9	NCC		3579	9.99	13.90	17.8	1.561
Abell 963	0.21	1.35 ± 0.06	6.8 ± 1.0	NCC		903	36.29	8.30	11.0	1.137
Abell 2261	0.22	1.59 ± 0.09	14.4 ± 2.6	CC		5007	24.32	10.20	17.5	1.213
Abell 2219	0.23	1.74 ± 0.08	18.9 ± 2.5	NCC		896	42.30	11.10	6.3	0.975
Abell 267	0.23	1.22 ± 0.07	6.6 ± 1.1	NCC	✓	3580	19.88	9.60	20.7	0.942
RX J2129.6+005	0.24	1.28 ± 0.07	7.7 ± 1.2	CC		552	9.96	8.00	16.0	0.721
Abell 1835	0.25	1.49 ± 0.06	12.3 ± 1.4	CC		7370	39.51	15.70	14.0	1.281
Abell 697	0.28	1.65 ± 0.09	17.1 ± 2.9	NCC		4217	19.52	22.60	14.3	1.269
Abell 611	0.29	1.24 ± 0.06	7.4 ± 1.1	NCC		3194	36.11	10.80	18.7	1.363
MS 2137.3−2353	0.31	1.06 ± 0.04	4.7 ± 0.6	CC		4974	57.38	6.50	12.8	1.675
MACS J1931.8−2634	0.35	1.34 ± 0.07	9.9 ± 1.6	CC		9382	98.92	10.10	7.5	0.959
Abell S1063	0.35	1.76 ± 0.09	22.2 ± 3.4	NCC		4966	26.72	10.20	5.5	1.493
MACS J1115.8+0129	0.36	1.28 ± 0.06	$8.6 \pm 1,2$	CC		9375	39.63	10.90	22.8	1.361
MACS J1532.9+3021	0.36	1.31 ± 0.08	9.5 ± 1.7	CC		1649	9.36	8.00	14.8	1.589
Abell 370	0.38	1.40 ± 0.08	11.7 ± 2.1	NCC	✓	7715	7.09	12.80	11.8	1.117
ZWCL 0024+17	0.39	1.00 ± 0.11	4.4 ± 1.6	NCC	✓	929	39.94	3.30	8.3	1.829
MACS J1720.3+3536	0.39	1.14 ± 0.07	6.3 ± 1.1	CC		6107	9.61	10.60	16.8	1.125
MACS J0429.6−0253	0.40	1.10 ± 0.05	5.8 ± 0.8	CC		3271	23.17	8.90	17.0	1.128
MACS J2211.7−0349	0.40	1.61 ± 0.07	18.1 ± 2.5	CC		3284	17.74	14.70	6.5	1.281
MACS J0416.1−2403	0.42	1.27 ± 0.15	9.1 ± 2.0	NCC	✓	10446	15.83	8.50	7.8	0.921
MACS J0451.9+0006	0.43	1.12 ± 0.06	6.3 ± 1.1	NCC	✓	5815	10.21	8.10	14.2	1.013
MACS J0417.5−1154	0.44	1.69 ± 0.07	22.1 ± 2.7	CC	✓	11759	51.36	22.70	9.8	1.806
MACS J1206.2−0847	0.44	1.61 ± 0.08	19.2 ± 3.0	NCC		3277	23.46	21.70	24.9	1.083
MACS J0329.6−0211	0.45	1.19 ± 0.06	7.9 ± 1.3	CC	✓	3582	19.85	12.10	10.3	1.103
MACS J1347.5−1144	0.45	1.67 ± 0.08	21.7 ± 3.0	CC		3592	57.51	36.60	15.5	1.084
MACS J1311.0−0310	0.49	0.93 ± 0.04	3.9 ± 0.5	CC		6110	63.21	9.60	14.2	0.995
MACS J0257.1−2325	0.50	1.20 ± 0.06	8.5 ± 1.3	NCC		1654	19.85	10.10	5.0	1.293
MACS J0911.2+1746	0.50	1.22 ± 0.06	9.0 ± 1.2	NCC		5012	23.79	4.80	6.2	1.280
MACS J2214.9−1359	0.50	1.39 ± 0.08	13.2 ± 2.3	NCC		3259	19.47	12.60	7.2	1.260
MACS J0018.5+1626	0.54	1.47 ± 0.08	16.5 ± 2.5	NCC		520	67.41	15.70	9.8	1.294
MACS J1149.5+2223	0.54	1.53 ± 0.08	18.7 ± 3.0	NCC	✓	3589	20.05	17.40	17.7	1.170
MACS J0717.5+3745	0.55	1.69 ± 0.06	24.9 ± 2.7	NCC	✓	4200	59.04	21.30	12.5	1.130
MACS J1423.8+2404	0.55	1.09 ± 0.05	6.6 ± 0.9	CC		4195	115.57	9.40	21.7	1.796
MACS J0454.1−0300	0.55	1.31 ± 0.06	11.5 ± 1.5	NCC	✓	902	44.19	24.30	14.5	1.393
MACS J0025.4−1222	0.58	1.12 ± 0.04	7.6 ± 0.9	NCC		10413	75.64	12.30	14.3	0.931
MS 2053.7−0449	0.58	0.82 ± 0.06	3.0 ± 0.5	NCC	✓	1667	44.51	5.10	14.3	0.867
MACS J0647.7+7015	0.59	1.26 ± 0.06	10.9 ± 1.6	NCC		3584	20.00	14.40	11.7	1.377
MACS J2129.4−0741	0.59	1.25 ± 0.06	10.6 ± 1.4	NCC	✓	3595	19.87	15.20	13.2	1.283
MACS J0744.8+3927	0.69	1.26 ± 0.06	12.5 ± 1.6	NCC	✓	6111	49.50	13.30	16.3	1.008
MS 1054.4−0321	0.83	1.07 ± 0.07	9.0 ± 1.3	NCC	✓	512	89.17	17.40	18.3	0.893
CL J0152.7−1357	0.83	0.97 ± 0.26	7.8 ± 3.0	NCC	✓	913	36.48	10.20	9.3	1.098
CL J1226.9+3332	0.89	1.00 ± 0.05	7.8 ± 1.1	NCC		5014	32.71	13.00	11.8	0.947

Note. The BOXSZ cluster sample. The columns give the cluster name, redshift, radius, mass, morphological classification (see Section 2), *Chandra* X-ray and Bolocam SZ observation details, and the maximum radius (see Section 4.1) included in this analysis.

25-cluster CLASH sample (Postman et al. 2012), the 12 MACS clusters at $z > 0.5$ (Ebeling et al. 2007), and the last 8 clusters chosen *ad hoc*, so there is no strict selection function. The images from both instruments are approximately 14 arcmin in size. Given the relatively high median redshift of the sample, $z = 0.42$ (see Fig. 1), these images in general contain information beyond r_{500} and therefore allow for studies of the clusters' outskirts. The clusters' masses were taken from S13. They were computed from X-rays assuming a constant gas fraction according to the method detailed in Mantz et al. (2010b) based on the measured gas fraction from Allen et al. (2008).

As in S13, CC and NCC clusters are differentiated using an X-ray luminosity ratio cut. If the luminosity within $0.05r_{500}$ is greater than 0.17 times the total luminosity within r_{500}, then the cluster is classified as CC. Within the BOXSZ sample, the CC clusters have a lower median redshift compared to the NCC clusters. In addition, 15 of the 16 highest redshift clusters are NCC. Although this trend matches what is expected based on cluster formation

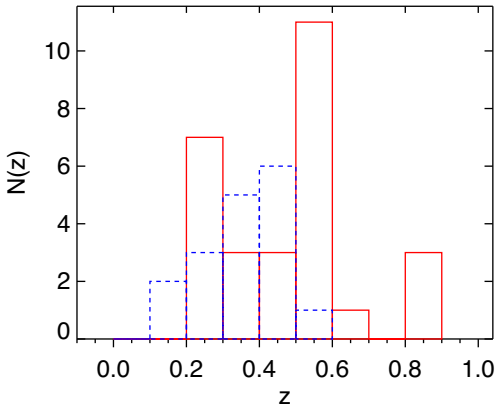

Figure 1. Redshift distribution of the sample. The red solid line indicates NCC clusters while the blue dotted line indicates CC clusters.

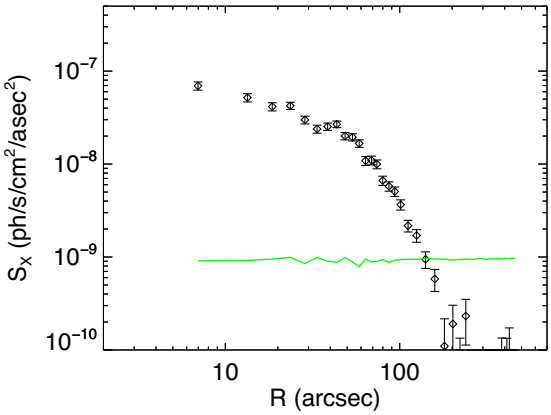

Figure 2. Example X-ray surface brightness profile (MACS J0416.1−2403). The green line represents the background level, and the black points are the the estimated surface brightness after subtracting the background.

models, the trend within the BOXSZ sample is most likely due to selection effects. Again following the convention of S13, clusters are classified as disturbed using the X-ray centroid shift parameter This quantity is the root mean square of the centroid-peak offset of centroids computed within circular apertures increasing from $0.05r_{500}$ up to r_{500} in steps of $0.05r_{500}$ (Poole et al. 2006; Maughan et al. 2012; Sayers et al. 2013b). All clusters with a centroid shift larger than 0.01 are considered disturbed. The sample contains a variety of clusters based on these classifications: 17 out of 45 are CC and 16 out of 45 are disturbed, with all but one of the disturbed systems being NCC (see Table 1).

3 DATA REDUCTION

3.1 X-ray

The X-ray data for this analysis were taken from the *Chandra* X-ray Observatory public archive, and all were obtained using the Advanced CCD Imaging Spectrometer (ACIS) focal plane arrays ACIS-I and ACIS-S. The data were reduced according to standard processing using CIAO version 4.7. Observation information is summarized in Table 1.

Raw event files were processed in several steps to make cluster, exposure, and background maps to ensure all sources of non-cluster signal were accounted for. First, event files were processed to create raw images, which were then filtered to remove cosmic rays and other point sources. Many of the observations were in VFAINT mode, where a larger pixel kernel was used to identify bad events. Standard bad pixels and chip boundaries were removed, as well as filtering for good time intervals. Light-curve filtering in the total 0.3–10 keV band of the background was performed to find any background flares. Light-curve filtering is ideally performed in the same manner as the blank-sky backgrounds. However, the energy band chosen in this work does not match that of the blank-sky backgrounds. A sample of 10 clusters was refiltered to test whether the different energy bands would affect the resulting surface brightness profiles, and no significant differences were found. We then restricted our analysis to only the 0.7–2 keV band in order to minimize the effect of the background on the data and the temperature dependence of the signal. The background was calculated by renormalizing *Chandra* blank-sky observations of the appropriate epoch to the flux measured in the outskirts of the chips that did not include cluster signal. These regions were always chosen to be sufficiently far from the cluster centre ($R > 1.5r_{500}$). The background data in counts was subtracted from the total counts to calculate the counts from the cluster ('source' counts).

The cluster centre was chosen as the X-ray surface brightness peak, and the same centre is used for the SZ maps. The images were then radially binned so that each annulus contained at least 100 total counts and 10 source (i.e. total minus background) counts, and was at least 5 arcsec in radial width. Due to the large binning, point-spread-function (PSF) effects could be ignored. Fig. 2 shows an example surface brightness profile resulting from the data reduction.

To extract the surface brightness, we need to compute the cooling function $\Lambda(T)$, which was done using the Mekal plasma modelling code in XSPEC (Arnaud 1996). A constant metallicity of 0.3 $Z_\odot$ was assumed. The n_H column density number was estimated using the program nH in the FTOOLS software from HEASARC[2] (Blackburn 1995), and is in general different for each cluster based on its location.

3.2 SZ

Bolocam was a 144-element bolometric imager stationed on the CSO with an 8 arcmin circular field of view (FOV). For the BOXSZ observations, Bolocam was configured with an SZ-emission-weighted band centre of 140 GHz, a PSF with a full width at half-maximum of 58 arcsec, and a scan pattern resulting in a final image size of 14 × 14 arcmin. The observations were conducted between 2006 November and 2012 March (see Table 1 for an observation summary). The SZ data reduction technique is described in detail in Sayers et al. (2011), and the relevant details are listed here. The pointing reconstruction is accurate to 5 arcsec, and the flux calibration is accurate to 5 per cent . Bright radio sources were removed from the images, including a total of 11 sources in the central cluster region thought to be member galaxies and 6 non-central sources thought to be unrelated to the clusters (Sayers et al. 2013a).

An instrument noise model is constructed for each cluster image based on jack-knifed realizations of the data. In addition to instrument noise, the images also contain brightness fluctuations associated with background signals from the primordial cosmic microwave background (CMB) anisotropies and dusty star-forming galaxies. These fluctuations are subdominant to the instrument

[2] http://heasarc.gsfc.nasa.gov/ftools/

noise, and have been included in the noise model based on power-spectrum measurements from *Planck* and the South Pole Telescope (George et al. 2015; Planck Collaboration XI 2016a). Brightness fluctuations associated with foreground emission, such as Galactic dust and synchrotron, are negligible given the observing frequency, image size, and high Galactic latitude of all the clusters, and therefore have not been included in the noise model. In the fits described below, the noise is assumed to be uncorrelated between pixels, which has been demonstrated to be a good approximation (Siegel et al. 2018), and the validity of this assumption is discussed in more detail in Section 6.2.

The data processing, which is primarily to remove atmospheric brightness fluctuations, results in a spatial distortion of the cluster signal. This distortion appears as a high-pass filter in the 2D images, and has been calculated separately for each cluster to account for the minor differences in filtering based on the observing conditions and the cluster shape. In all of the fits described below, this has been accounted for by applying the cluster-specific high-pass filter to the candidate model prior to comparison with the data.

4 METHOD

There are two main components of this work: the individual cluster fits and the sample mean fits. For the individual cluster fitting, two types of models are adopted to fit the density and temperature profiles: smooth parametric functions and concentric shell models. Two approaches are explored to fit the sample mean profiles, both using a version of the concentric shell modelling at common radii to constrain average profiles and their intrinsic scatters.

4.1 Individual cluster analysis

Both the smooth parametric models and the concentric shell models are separately fitted to the data. The former assumes a smooth profile that one can easily compare with other studies and gives a general idea of the cluster as a whole. The latter assumes constant temperature and density in a set of five radial shells. While this step-wise modelling is somewhat simplistic, it allows for possible substructures and irregularities in the profiles. For the individual cluster fitting, the maximum radius, $r_{\rm max}$, is chosen to be the location where the X-ray data reaches a signal to noise (i.e. source counts over the square root of total counts; see Section 3.1) of one. Table 1 reports $r_{\rm max}$ for all clusters. For most clusters, $r_{\rm max}$ is near r_{500}. Note that for the more distant clusters, although the central bin is chosen to have a radius of 30 arcsec, the width of the other bins can be less than this value. However, both the PSF and correlations between bins are accounted for in the fitting procedure, so impacts from the PSF are included in the analysis. For both types of fits, we use MCMC to maximize a joint SZ and X–ray likelihood function by varying either the shell deprojection values or the parameters of the smooth parametric profiles.

4.1.1 *Smooth parametric profiles*

For the smooth parametric fits, we assume fitting functions similar to those given in Vikhlinin et al. (2006), which are based on X-ray observations of 13 clusters. Specifically, the density is assumed to follow a double-beta profile

$$n_e(r) = \left(n_{0,1}^2(1+(r/r_{c,1})^2)^{-3\beta} + n_{0,2}^2(1+(r/r_{c,2})^2)^{-3\beta}\right)^{1/2}, \quad (1)$$

where $n_{0,i}$ and $r_{c,i}$ are the central density and the scale radius for the i'th component, respectively, and β is the slope parameter for the components. The temperature is assumed to follow a profile given by

$$T_e(r) = T_0 \frac{T_{\rm min}/T_0 + (r/r_{\rm cool})^{1.9}}{1+(r/r_{\rm cool})^{1.9}} \left(1+(r/r_t)^2\right)^{-\alpha}, \quad (2)$$

where T_0 is the normalization temperature, $T_{\rm min}$ is the temperature at the centre, $r_{\rm cool}$ is the cool-core radius, r_t is the outer scale radius, and α is the outer slope. The inner slope is fixed to 1.9 (Vikhlinin et al. 2006). These profiles are then used to determine a 1D projected X-ray surface brightness profile and a 2D SZ image that can be compared to the observational data. Specifically,

$$S_{\rm X\text{-}ray}(R) = \frac{1}{4\pi(1+z)^4} \int n_e^2(\ell)\Lambda(T_e(\ell))\mathrm{d}\ell \quad (3)$$

gives the X-ray surface brightness at the projected radius R, where the integral is over the full line of sight at R. For these spherical models, we make the substitutions $\ell = \sqrt{r^2-R^2}$ and $\mathrm{d}\ell = r\mathrm{d}r/\sqrt{r^2-R^2}$. $\Lambda(T_e(\ell))$ is the cooling function (which is computed numerically as outlined in Section 3.1, and scales approximately as $T^{1/2}$).

The change in CMB brightness due to the SZ effect is given by

$$S_{\rm SZ}(R) = g(x) S_{\rm CMB} \frac{k_{\rm B}\sigma_T}{m_e c^2} \int n_e(\ell) T_e(\ell)\mathrm{d}\ell, \quad (4)$$

where $S_{\rm CMB}$ is the average CMB brightness, $k_{\rm B}$ is the Boltzmann constant, $\sigma_{\rm T}$ is the Thomson cross-section, $m_{\rm e}$ is the electron mass, c is the speed of light, and the integral is again over the full line of sight at R. The prefactor $g(x)$ contains the frequency dependence of the SZ effect (see, e.g., Carlstrom, Holder & Reese 2002). $S_{\rm SZ}(R)$ is used to obtain a 2D image of the SZ signal, which is directly compared to the observational data after accounting for the effects of the image filtering and PSF described in Section 3.2.

The fit for each cluster proceeds as follows. First, a basic single-beta isothermal model is assumed, with the parameters $n_{0,1}$, $r_{c,1}$, β, and T_0 allowed to vary. Next, a second fit is performed with additional free parameters that describe a second density component, generally due to the steep inner profile often found in cool-core clusters ($n_{0,2}$, $r_{c,2}$). The χ^2 value from each of these fits is used to compute a probability to exceed (PTE), and the fit with the higher PTE is then selected as the better description of the data for that cluster. The PTE values are again used to compare fits with additional parameters to allow for a temperature change at large radii (r_t, α) and with additional parameters associated with a temperature drop towards to core ($T_{\rm min}$, $r_{\rm cool}$). Out of all the possible permutations given above, the fit with the highest PTE is selected for each cluster.

4.1.2 *Concentric shell deprojections*

For the deprojections, a concentric shell model is assumed, which assigns constant densities and temperatures within concentric 3D shells (McLaughlin 1999) – see Fig. 3 for the geometry. For the individual cluster analysis, we use five shells: The first shell corresponds to the approximate resolution of Bolocam, and spans the radial range 0–30 arcsec. At increasing radii, the shells are logarithmically spaced up to the cut-off radius, $r_{\rm max}$. This logarithmic spacing results in more uniform signal to noise within each shell compared to a linear spacing. Note that the azimuthally averaged 1D projected X-ray surface brightness bins do not need to have the same radii as the 3D model shells. In fact, the spacing between the 1D projected data bins is much smaller than the spacing between

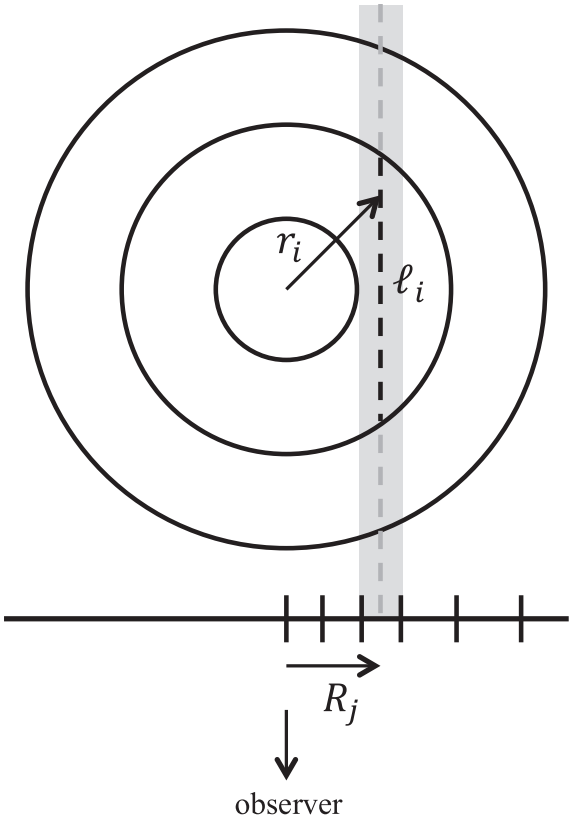

Figure 3. The concentric shell model, adapted from McLaughlin (1999). The observer sees a 2D map with radial bins denoted by R_j, while the 3D shells have radii r_i. The radial coordinates for the 2D bins do not necessarily match those for the 3D shells. ℓ_i is the distance along the line of sight that radial shell i contributes to the 1D bin at radius R_j.

the 3D shells, especially in the centre of the cluster where there are many counts.

The X-ray surface brightness in the projected bin j centred at radius R_j is modelled as

$$S_{\text{X-ray}}(R_j) = \frac{1}{4\pi(1+z)^4} \sum_{i=1} n_{\text{e},i}^2 \Lambda(T_{\text{e},i}) \cdot l_i(R_j) \tag{5}$$

where i is the index of the 3D shell , $n_{\text{e},i}$ is the electron density within the shell, $n_{\text{H},i}$ is the hydrogen density within the shell, $T_{\text{e},i}$ is the electron temperature within the shell, and $l_i(R_j)$ is the line-of-sight length of the shell. The cooling function $\Lambda(T_{e,i})$ is the same as in the smooth parametric fits. The SZ signal in the projected bin centred at radius R_j is modelled as

$$S_{\text{SZ}}(R_j) = g(x) S_{\text{CMB}} \frac{k_{\text{B}}\sigma}{m_{\text{e}}c^2} \sum_{i=1} n_{\text{e},i} T_{\text{e},i} \cdot l_i(R_j). \tag{6}$$

Without modification, the concentric shell model only accounts for signal from within r_{max}. Particularly for the SZ signal, this can lead to a bias in the results because a significant amount of the projected signal originates from line-of-sight distances beyond r_{max}.[3]

[3]For example, near the cluster centre approximately 3 per cent of the SZ signal originates beyond r_{max}, while at a projected radius of $r = 0.5r_{500}$ approximately 25 per cent of the SZ signal originates beyond r_{max}. In practice, not accounting for the projected signal beyond r_{max} can bias the recovered temperature in the final deprojection shell by up to 25 per cent .

We have therefore adopted the following iterative procedure to estimate this emission. First, we perform deprojections assuming there is no emission beyond the last shell. We then use the resulting shell values in temperature and density to compute the corresponding squared density and pressure shell values. These are then fitted by the smooth parametric curves given in Piffaretti et al. (2011) (for density) and S13 (for pressure), where the overall amplitude is allowed to vary. Once the normalization is constrained, these profiles are then integrated between r_{max} and $10r_{500}$ to estimate the signal contributed by the line of sight beyond the last concentric shell, and new deprojections are computed after accounting for this additional signal. This process is repeated until the deprojections converge, typically after 3–4 iterations. The results are not sensitive to the exact model used to describe the smooth density and pressure profiles, and, for example, assuming either the S13, Arnaud et al. (2010), or Planck Collaboration V (2013) parametrization for the pressure results in negligible changes to the deprojected values.

Most results in this work are obtained with the general approach presented in Ameglio et al. (2007). However, this work contains several modifications to that approach: No temperature regularization is applied, the assumption of the emission beyond the last radial shell is modified (see above), and the radial bins used to azimuthally average the X-ray surface brightness images no longer need to be at the same radii as the 3D concentric shells.

4.1.3 *Individual cluster likelihood*

Both the smooth parametric profiles and the concentric shell deprojections are fitted to the data using an MCMC to maximize a single joint likelihood:

$$\mathcal{L} = \mathcal{L}_{\text{X-ray}} \times \mathcal{L}_{\text{SZ}}. \tag{7}$$

For the SZ data, the log-likelihood is computed according to

$$ln(\mathcal{L}_{\text{SZ}}) = \sum_j -\frac{1}{2}\frac{(O_j - M_j)^2}{\sigma_j^2} \tag{8}$$

where O_j is the observed projected SZ brightness in 2D map pixel j, M_j is the projected brightness based on either the smooth parametric profile or the concentric shell model (after accounting for the effects of the PSF and the image filtering), and σ_j is the rms noise in each pixel j. The noise in the SZ images is assumed to be uncorrelated between individual map pixels and to follow a Gaussian distribution, which was shown to be a good approximation in Siegel et al. (2018). For the X-ray data, the log-likelihood is computed according to

$$ln(\mathcal{L}_{\text{X-ray}}) = \sum_j -\frac{1}{2}\frac{(O_j - M_j)^2}{M_j} - \frac{1}{2} ln(2\pi M_j). \tag{9}$$

M_j is the model of the total counts in a bin:

$$M_j = M_{\text{src},j} + \text{Bkg}_j. \tag{10}$$

$M_{\text{src},j}$ and Bkg_j are the source and background counts, respectively, for bin j. The naming conventions are identical to the SZ log-likelihood, except that the index j corresponds to a projected 1D radial bin rather than a 2D map pixel. The extra term is needed since the variance (the model) is fitted for as well, and so the normalization cannot be ignored. Although the X-ray noise follows a Poisson distribution, we approximate the likelihood with a Gaussian distribution with variance equal to the mean value of the model. By requiring each radial bin to have a sufficiently large number of counts, at least 100, this Gaussian approximation provides a good description of the noise statistics. Since the model M_j is in units

of counts, equations (3) and (5) must be converted to counts. For the smooth parametric profiles, equation (3) is integrated over the bin width, while for the deprojected profiles, equation (5) is assumed constant within the bin and multiplied by the area of the bin.

4.2 Ensemble cluster analysis

Under the assumption of purely gravitational collapse, clusters' physical properties obey simple scaling relations. However, the other physical effects that impact cluster formation can produce some bias and scatter relative to these relations. So, considering the entire population of clusters in the Universe, we expect that any given physical property can be described by an average value along with a scatter relative to this average value. Any representative sample of observed clusters can then be used to constrain such universal mean values and their intrinsic scatters. Therefore, in addition to characterizing the individual profiles of the observed clusters, we utilized our data to constrain the universal mean temperature and density profiles and their scatters.

There are two possible approaches to this aim. The first approach consists in fitting for the mean profile and its scatter by modelling them in a likelihood that fits directly the X-ray and SZ data for all clusters at once. We will call this approach 'global likelihood'. This method properly accounts for sample variance and for all non–linearities in the modelling. (We discuss this method and its results on the density profile in Appendix A). In what follows, we will present the results of the meta-analysis of density and temperature. The meta-analysis consists in deriving ensemble properties for a given physical quantity from the results obtained for that quantity in an individual-object data analysis. It is important to realize that the scatters obtained with the two methods are not, and don't need to be, the same. The relations between the two cannot be easily evaluated.

To obtain ensemble-average constraints on the density and temperature profiles with the meta-analysis method, we first compute concentric shell deprojections for all of the clusters in a set of five logarithmically spaced radial shells, scaled according to r_{500} and extending to $r_{\rm max} = 1.25r_{500}$. Note that these bins are not the same as those used in the individual concentric shell deprojections. For this ensemble analysis, identical bins (in units of r_{500}) were used for all 45 clusters in the sample. The innermost shell extends to $0.15r_{500}$, which is larger than the Bolocam PSF for 34 out of 45 of the BOXSZ clusters.

Due to the differing signal to noise of the X-ray maps, not all of the clusters were deprojected in all five shells. Out of the BOXSZ sample of 45 clusters, 17 were deprojected in all 5 shells, 27 were deprojected in the four innermost shells, and 1 cluster (RX J2129.6+005) was deprojected in the three innermost shells.

The deprojected density and temperature profiles were first rescaled according to the self-similar relations from Nagai et al. (2007), which account for the gravity-only differences in the clusters' physical properties given their masses and redshifts. The density was scaled according to

$$n_{\rm e,500} = 500\frac{\Omega_{\rm b}}{\Omega_{\rm m}}\frac{\rho_{\rm crit}(z)}{\mu_{\rm e}m_{\rm p}}, \tag{11}$$

where $\Omega_{\rm m}$ is the total matter density, $\Omega_{\rm b}$ is the baryonic density, $\rho_{\rm crit}$ is the critical density of the Universe, $\mu_{\rm e} = 1.16$ is the mean molecular weight for electrons, and $m_{\rm p}$ is the mass of the proton. The temperature was scaled according to

$$T_{500} = 8.71\ {\rm keV}\left(\frac{M_{500}}{10^{15}\,{\rm M}_{\odot}}\right)^{2/3}E(z)^{2/3}, \tag{12}$$

where $E(z) = \sqrt{\Omega_{\rm m}(1+z)^3+\Omega_{\Lambda}}$ represents the evolution of the Hubble parameter. The values of r_{500}, M_{500}, and z are listed in Table 1, and were taken from S13 based on the analysis methods of Mantz et al. (2010b).

Once the scaled individual deprojections for the clusters were obtained at the set of common scaled radii, they were combined to obtain ensemble mean profiles, along with the intrinsic scatters about these mean profiles, using the Gaussian process formalism described in S13. In this approach, the binned density and temperature profiles of the clusters were assumed to be Gaussian distributed around a mean value, with a width that includes the individual clusters' covariances (as computed from the deprojections) and an intrinsic scatter for the ensemble. The log-likelihood used to constrain the model is

$$ln\mathcal{L} = \sum_{k} -\frac{1}{2}\left[\tilde{\boldsymbol{x}}_{\boldsymbol{k}}^{T}(\mathbf{S}+\mathbf{U_k})^{-1}\tilde{\boldsymbol{x}}_{\boldsymbol{k}} + ln|\mathbf{S}+\mathbf{U_k}|\right] \tag{13}$$

where $\tilde{\boldsymbol{x}}_{\boldsymbol{k}}$ is a vector containing ten elements (i.e. one element for each of the five radial shells for both the density and the temperature), with $\tilde{\boldsymbol{x}}_{\boldsymbol{k}} = \overline{\boldsymbol{x}} - \boldsymbol{x}_{\boldsymbol{k}}$ for the ensemble mean profile $\overline{\boldsymbol{x}}$ and individual cluster concentric shell deprojected density and temperature profile $\boldsymbol{x}_{\boldsymbol{k}}$, k is the cluster index (e.g. ranging from 1 to 45 for the full BOXSZ sample), $\mathbf{U_k}$ is the covariance matrix for the individual cluster deprojection (which can be treated as a 'measurement' covariance matrix), and $\mathbf{S}$ is the intrinsic scatter matrix. The parameters returned from the fit are the mean profile $\overline{\boldsymbol{x}}$ and the intrinsic scatter about this profile $\mathbf{S}$. Note that, as with $\tilde{\boldsymbol{x}}_{\boldsymbol{k}}$, both $\mathbf{U_k}$ and $\mathbf{S}$ include terms associated with both the density and the temperature. Finally, we have assumed the intrinsic scatters to be Gaussian, rather than log-Gaussian. This choice was motivated by the shape of the measured distributions for $\mathbf{U_k}$ along with the fact that noise fluctuations in the SZ data can sometimes produce negative values of $\tilde{\boldsymbol{x}}_{\boldsymbol{k}}$ which are incompatible with the assumption of a log-Gaussian distribution.

Fig. 4 shows a typical example of correlations among the elements in the covariance matrix $\mathbf{U_k}$. There are significant anticorrelations between adjacent temperatures. In particular, the two inner shells have a correlation close to -1. As expected, there are also anti-correlations between densities and temperatures of the same shell. Furthermore, there are positive correlations between temperature values separated by one shell.

Given the quality/quantity of the observational data, it was not possible to constrain all values of the $\mathbf{S}$ matrix. To minimize the number of free parameters, we assume a diagonal-only $\mathbf{S}$ matrix, so there are no covariances between the intrinsic scatter values. This results in fitting for 5 mean densities, 5 mean temperatures, 5 density intrinsic scatter elements, and 5 temperature intrinsic scatter elements, for a total of 20 parameters.

The procedure was repeated to fit for the ensemble-average pressure profiles. First, the individual cluster MCMC chains containing the scaled densities and temperatures were converted to scaled pressures at each step in the chain according to $P(P_{500}) \propto n(n_{\rm e,500})T(T_{500})$. Explicitly, the pressure scaling is

$$P_{500} = 3.68\times10^{-3}\ \frac{\rm keV}{\rm cm^{-3}}\left(\frac{M_{500}}{10^{15}\,{\rm M}_{\odot}}\right)^{2/3}E(z)^{8/3}. \tag{14}$$

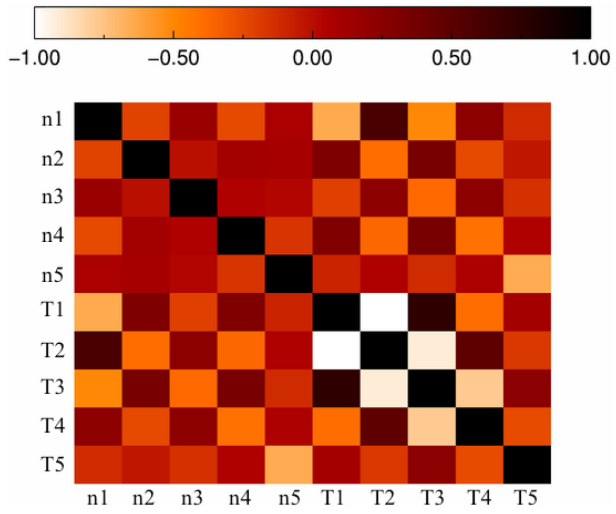

Figure 4. A typical correlation matrix $\mathbf{U_k}$ of a concentric shell deprojection (the cluster is MACS J1423.8+2404). n_i denotes the i'th density shell while T_i denotes the i'th temperature shell.

Individual cluster pressure deprojections and their covariance matrices were then calculated from these chains. The meta-analysis procedure described above was then used to determine the ensemble-average pressure profile and its intrinsic scatter based on these individual deprojections.

5 ANALYSIS OF MOCK CLUSTER OBSERVATIONS

In order to search for potential biases in our fitting procedures, we performed the complete analysis on a set of mock observations of smooth cluster models generated from a set of known parameters. Although the smooth models used to generate the clusters in the mock observations do not capture the full complexity of real clusters, they were chosen because they allow for simpler comparisons between the input cluster parameters and those generated by our fitting procedures.

5.1 Individual cluster analysis

A set of four clusters was constructed to test our individual cluster-fitting routines. These clusters were generated using either a single- or a double-beta density profile and a constant temperature profile. The parameters used to produce the test clusters were chosen based on the characteristics of a representative set of real clusters from the BOXSZ sample: Abell 1835, MACS J0417.5−1154, MS 2053.7−0449, and MACS J0744.8+3927, denoted as clusters A, B, C, and D, respectively, and given in Table 2. Based on the fits to the real clusters, clusters A, B, and D were generated using double-beta density profiles while cluster C was generated using a single-beta density profile.

Given the input density and temperature profiles, along with the exposure times (∼50 ks) and effective areas of the real images, mock X-ray observations were produced to match the *Chandra* ACIS-I FOV and angular resolution (Gardini et al. 2004; Rasia et al. 2008). The mock maps did not include any background signal. An analogous procedure was used to generate the mock SZ observations, such that they match the noise properties, image size, and angular resolution of the real Bolocam observations. In addition, the image filtering of the Bolocam data processing was also applied to the cluster in the mock observation. For each of the four test clusters, 100 mock X-ray and SZ observations were produced, each with a different random realization of the noise.

We then applied our MCMC fitting code to the X-ray/SZ pair of mock observations for each given cluster type in order to obtain single-cluster parametric fits. The smooth parametric profiles assumed for the fits matched those used to generate the clusters (i.e. isothermal with a single- or double-beta profile for the density). Due to degeneracies between the fitted parameters, the noise fluctuations in the different mock observations often produce results with different fit parameters yet similar profile shapes. Therefore, rather than comparing the fitted parameter values with the inputs used to generate the test clusters, we compared the actual shapes of the fitted profiles. Using the output of the MCMC, we thus plotted the best-fitting density for each of the 100 mock observation pairs at a set of closely spaced radii spanning the approximate range constrained by the data. Then, at each radius the overall median fitted density values, along with the inner 68 per cent of the fitted density values, were computed. This output was then compared with the input profile used to generate the cluster.

Fig. 5 shows the fractional difference between the fitted and input density profiles computed using the above procedure. The span encompassing 68 per cent of the recovered density values is different for each of the four test clusters, due to the clusters' varying distances, masses, noise properties, and the number of parameters that were fit for. The only statistically significant bias appears in cluster A, where the profile is on average 2σ lower than the input profile. However, the absolute magnitude of this bias is quite small (<1 per cent), and it appears to be random between the four test clusters (i.e. the direction of the bias is not constant). In addition, other sources of error, such as calibration and measurement noise, are ≃5–10 per cent, significantly larger than this potential bias in our reconstructions. There are further indications of a possible bias near the extreme centres of clusters A, B, and D, although this

Table 2. Cluster models used for the mock observations.

Cluster	z	Real counterpart	M_{2500} ($10^{14}\,M_\odot$)	T (keV)	$n_{e0,1}$ ($10^{-2}\,cm^{-3}$)	$r_{c,1}$ (kpc)	$n_{e0,2}$ ($10^{-2}\,cm^{-3}$)	$r_{c,2}$ (kpc)	β
A	0.25	Abell 1835	5.11	7.0	23.48	43.0	2.13	190.0	0.70
B	0.44	MACS J0417.5−1154	9.50	9.5	6.80	55.7	0.52	454.8	0.86
C	0.58	MS 2053.7−0449	0.59	5.0	0.90	105.3	–	–	0.61
D	0.69	MACS J0744.8+3927	3.50	8.0	6.20	42.6	1.05	184.7	0.68

Note. The input parameters used to generate the smooth cluster models for the mock observations. Each of these four test clusters was based on the fit to a real cluster in the BOXSZ sample. In all cases, the cluster was assumed to be isothermal. The density profiles for clusters A, B, and D were based on the double-beta model, while the density profile for cluster C was based on the single-beta model.

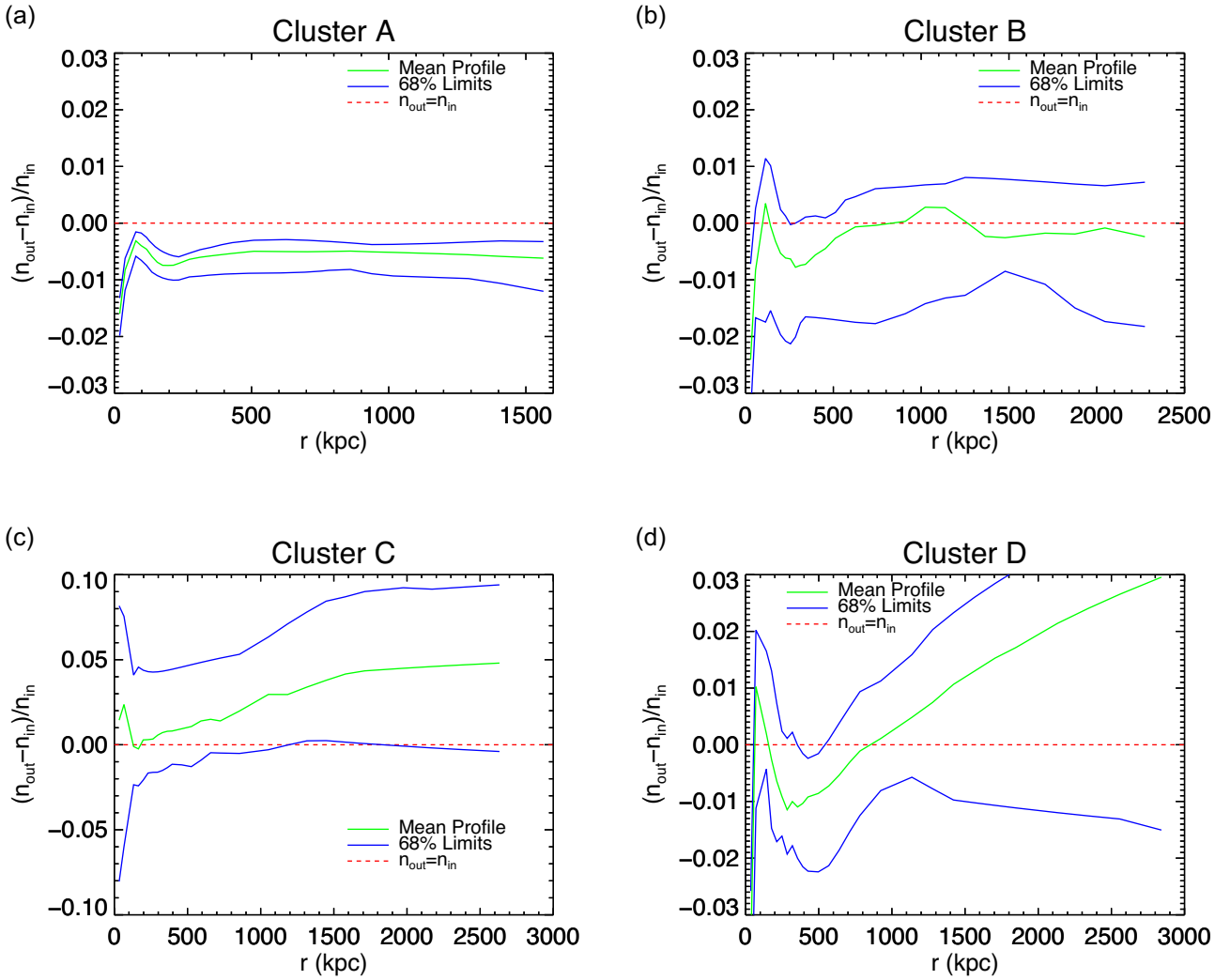

Figure 5. Normalized difference between the input deprojected density profile used to generate the test clusters and the fitted deprojected density profile recovered from the mock observations. Note the *y*-axis scale is larger for cluster C than for the others. The green central curve represents the mean fitted profile, while the blue limits represent the upper and lower 68 per cent limits for the fitted density at that particular radius.

is likely an artefact of the minimum radial width allowed when creating the binned projected profiles (5 arcsec). In other words, this bias is outside of the region nominally constrained by our fitting procedure. This test therefore demonstrates that our fitting method recovers individual cluster density profiles with a bias that is negligible compared to our measurement noise and calibration uncertainties.

For each X-ray/SZ pair of mock observations, a single isothermal value for the temperature was also fitted for. For each test cluster, the 100 resulting temperature values were used to determine the mean and standard deviation of the fitted values, and the results are presented in Table 3. Overall, the fitted temperatures agree reasonably well with the input values, and the only statistically significant difference is found in cluster A at $\simeq 3\sigma$. However, as with the slight bias in the recovered density profile for this cluster, the absolute magnitude of the bias is small compared to other sources of error in our analysis.

Based on the above results, we also infer that the profiles obtained from the concentric shell deprojections do not contain a significant bias. The statistical uncertainties on the deprojections are larger than those for the smooth parametric fits, and so the bias would need to be significantly larger to noticeably impact those fits. Further supporting this conclusion, as described in the following section,

Table 3. Cluster temperatures for the mock observations.

Cluster	Input T (keV)	Output T (keV)	Input scatter
A	7.0	6.43 ± 0.16	0.25
B	9.5	9.35 ± 0.13	0.25
C	5.0	4.69 ± 0.21	0.30
D	8.0	7.93 ± 0.12	0.25

Note. The input temperatures used to generate the test clusters, along with the fitted temperatures recovered from the mock observations of those clusters (individual cluster fitting; see Section 5.1). The error bars denote the uncertainty on the mean recovered temperature from 100 mock observations. The last column reports the fractional input scatter for the ensemble cluster temperature profiles in Section 5.2.

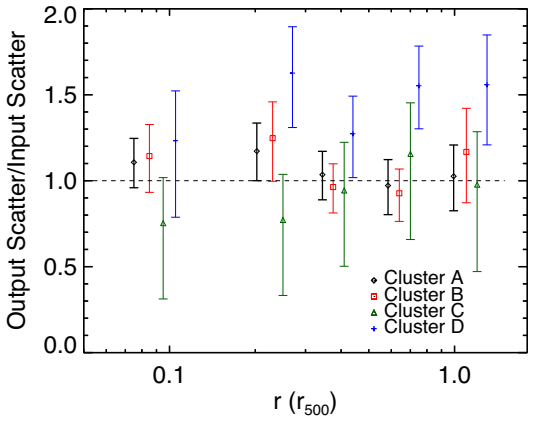

Figure 6. Output intrinsic temperature scatters with errors for the four mock cluster samples. Since the input scatter used for cluster C was different from that of the other three test clusters, the recovered scatters are plotted relative to the input values.

the ensemble deprojection analysis of the mock cluster observations results in profile shapes that are unbiased with respect to the input values.

5.2 Ensemble cluster analysis

In addition to analysing mock observations of individual clusters, we also fitted for mean profiles, and the intrinsic scatters about these mean profiles, using mock observations of larger cluster samples. This procedure allowed us to search for potential biases in the ensemble fits presented in Section 4.2. For this test, we produced 4 sets of 40 mock cluster observations, with each set thus containing a similar number of clusters to the full BOXSZ sample. Within each of these 4 sets, all 40 of the test clusters were generated using the parameters for a single cluster from Table 2 (e.g. set one was based on cluster A, set two on cluster B, etc.) Within a given set, all 40 of the test clusters were generated based on the same density profile, but the isothermal temperature of each cluster was scattered about its nominal value with an rms equal to the value given in Table 3.

Individual deprojections were then computed from each mock observation in each sample. Next, the joint fitting code presented in Section 4.2 was applied to those 40 deprojections to obtain the fitted values of the mean profiles and the intrinsic scatters about those profiles, with the results shown in Fig. 6. Although the test clusters are isothermal, and therefore the scatter is completely correlated between all of the deprojection shells, we performed the fits using our baseline procedure which sets all of the off-diagonal scatter values to 0.

For three of the clusters (A, B, and C), the recovered intrinsic scatter values are fully consistent with the input values. However, in the case of cluster D, the recovered scatter value is higher in all five radial bins. Averaging all five bins together for cluster D, including the covariance between the bins, results in a radially averaged scatter that is higher than the input value at a significance of 3σ. The cause of this bias is unknown, but, given that it only occurs in one of the four test clusters, it must be due to something specific to that cluster (e.g. it is an extremely compact cluster near the high-z limit of our sample). While it is computationally intractable to perform these test fits on all 45 clusters in our sample to determine if such a bias exists in any of the other objects, this result hints at a possible upward bias in the recovered temperature scatters, which we discuss in more detail in Section 6.2.

6 RESULTS

6.1 Individual cluster results

The reader should refer to Appendix B for goodness of fit details (Table B1) , the parameters obtained from the smooth parametric fits (Table B2) and the concentric shell models (Table B3). The individual cluster profiles are plotted in the appendix along with descriptions and previously published results that exist for each cluster. The ACCEPT study (Cavagnolo et al. 2009) is plotted for overlapping clusters but given the differences in calibration, we do not analyse results beyond qualitative visual comparison. The individual cluster results may be summarized as follows:

(i) We are able to fit for density and temperature profiles to or beyond r_{500} in 34 out of 45 clusters. For the clusters in common with the ACCEPT spectroscopic X-ray analysis, our results extend to larger radii in all cases, typically by a factor of $\simeq$2 (see the plots in the appendix).

(ii) The PTEs of the concentric shell deprojections are generally very low, $<$0.001, indicating a poor fit quality. The assumption of flat densities within the radial shell bounds (which are at least 30 arcsec wide in radius) is not a good representation of the projected X-ray data which has been binned to a much finer resolution ($\sim$5 arcsec in width). The PTEs of the smooth parametric fits are also very low on average. This is again driven mainly by the X-ray data, which are of sufficient quality to detect substructures and other features that are not well modelled by a smooth profile.

(iii) Based on the parametric fits, the data show $>3\sigma$ evidence of a cool core in five clusters (29 per cent of the cool-core subset of 17 clusters defined based on the X-ray luminosity ratio described in Section 2): Abell 2204, MS 2137, MACS J0417.5−1154, MACS J1347.5−1144, and MACS J1423.8+2404. The significance of the cool core was determined based on the difference of T_0 and $T_{\rm min}$, with the uncertainty on this difference determined using the full covariance matrix between the two parameters. The relatively low detection rate was driven by a combination of measurement noise and coarse angular resolution in the SZ data, the latter of which is insufficient to resolve a potential cool core for many of the BOXSZ clusters.

(iv) Several X-ray spectroscopic analyses indicate that cluster temperature profiles generally peak near $0.3r_{500}$ and then decrease at larger radii (e.g. Vikhlinin et al. 2006; Leccardi & Molendi 2008; Arnaud et al. 2010). The combined X-ray/SZ analysis of Eckert et al. (2013a) shows a similar trend. Based on our smooth parametric fits, 10 clusters show $>3\sigma$ evidence for a temperature decrease at large radii: Abell 2204, Abell 209, Abell 1423, Abell 963, Abell 2261, Abell 2219, Abell 697, MS 2137, MACS J1720.3+3536, and MACS J0717.5+3745. The significance of the temperature drop was determined based on the the difference between the temperature at $0.3r_{500}$ and r_{500}. At every step of the MCMC, this difference was calculated from the smooth parametric temperature equation. The significance of the temperature change was then computed by dividing the mean difference by the standard deviation of the difference. One cluster, Abell S1063, shows $>3\sigma$ evidence for an increase in the temperature profile at large radii. However, the statistical significance of the temperature rise is $<3\sigma$. This implies that most of the clusters are consistent with an isothermal profile, which is expected based on the signal-to-noise ratio

obtained in our smooth parametric fits at large radii. Specifically, previous results indicate a typical temperature drop of $\simeq$3–5 keV between the peak and r_{500}. The noise uncertainties on our smooth parametric profile fits over that radial range are $\simeq$1–2 keV, thus implying that only a small fraction of our sample is likely to show a temperature drop with a statistical significance of $>3\sigma$.

6.2 Ensemble results

The density profiles for the full sample, CC and NCC clusters, are reported in Fig. 7 (top panels), together with their uncertainties. We find a higher density in the innermost shell for the CC clusters compared to the NCC clusters. The fractional intrinsic scatter values recovered for the density profiles fall from approximately 0.4 in the innermost shell to 0.1 at intermediate radius, before showing an increase near r_{500}, which is largely consistent with previous works using a similar ensemble fitting approach (see Fig. 8; e.g. Mantz et al. 2016).

The mean temperature and pressure profiles, along with their associated intrinsic scatters, are also shown in Fig. 7. Overall, at larger radii, the mean temperatures are relatively flat, and we do not detect the clear decrease found in other studies (see Fig. 8; e.g. Vikhlinin et al. 2006; Leccardi & Molendi 2008; Arnaud et al. 2010; Eckert et al. 2013b; McDonald et al. 2014). Specifically, we do not see a temperature increase at small radii $\sim 0.2 r_{500}$ before a subsequent decrease at large radii. However, our temperature profile is compatible with the results of Leccardi & Molendi (2008) in that region, and only 1–2σ lower than the profiles obtained by Vikhlinin et al. (2006) and McDonald et al. (2014). While this difference is not statistically significant, it may be due to the selection effects given that the Leccardi & Molendi (2008) sample is most similar to ours in mass and redshift. Given the modest statistical significance of this difference, it may simply be due to noise fluctuations. However, inaccurate subtraction of the X-ray background may also play a role. For example, oversubtraction of the hard background would tend to bias spectroscopic X-ray temperatures low while biasing our derived temperatures high (via the reduction in X-ray-derived density). The difference could also be related to cluster physics. For instance, clumping within the ICM, which is expected to increase with radius, will tend to bias spectroscopically derived temperatures low compared to the X-ray/SZ values derived in our analysis (e.g. Mazzotta et al. 2004; Rasia et al. 2005; Vazza et al. 2013). Elongation of the cluster along the line of sight, which will increase the SZ brightness compared to the X-ray brightness, could also artificially boost the temperatures recovered in our analysis (e.g. Cooray 2000). Another possibility for the slightly higher than expected temperatures at large radii may be biases in the SZ data. Indirect evidence for such an effect can be found by comparing the pressure profiles obtained by Sayers et al. (2013b), based solely on Bolocam data, to those obtained by Sayers et al. (2016) based on a joint analysis of Bolocam and Planck for a nearly identical set of clusters. Beyond $\simeq 0.5 r_{500}$, the latter work found a lower value for the pressure profile, with the difference increasing to a factor of $\simeq$1.5 at r_{500}. This implies that the Bolocam data alone may be overestimating the pressure at large radii, which would bias our temperature profiles high in that region. This can be seen in the mean pressure profile plot. However there is good agreement in the radial range of interest in this study when compared with Arnaud et al. (2010) and Planck Collaboration V (2013). In addition, the mean temperature profiles recovered for the CC and NCC subsets in the innermost shell are not different at a statistically significant level (i.e. the CC subset does not show a significant drop towards the cluster centre). This is likely a result of the coarse binning required by the SZ data. Specifically, the innermost shell extends to $0.15 r_{500}$, which is generally not small enough to resolve the cool core. All of the potential biases and physical effects noted in this paragraph apply to the individual cluster temperature profiles as well, and therefore may explain differences compared to other studies (e.g. ACCEPT) that appear for some clusters.

The fractional temperature intrinsic scatters are approximately constant with radius, with a value of 0.4–0.5. Spectroscopic X-ray studies, such as Vikhlinin et al. (2006) and Mantz et al. (2016), have found similarly constant profiles, although they have found significantly lower fractional scatters of approximately 0.1. The reason for this discrepancy is not fully understood, although it appears to be largely due to the combination of line-of-sight differences in the SZ/X-ray signals, cluster selection, and non-idealities in the SZ measurement noise. First, Ameglio et al. (2007), using an SZ/X-ray deprojection method nearly identical to ours, found that, for a given cluster, the recovered temperature profiles differ with a fractional rms of $\simeq$0.15 when different observational lines of sight are considered. This variation is due to deviations from spherical symmetry in the ICM combined with the differing density/temperature dependance of the X-ray and SZ signals, and would therefore not appear in a single-probe X-ray analysis but would appear in our combined SZ/X-ray analysis. Secondly, the simulations of Barnes et al. (2017) indicate that the temperature profiles of massive clusters of diverse morphologies, such as that of our sample, show strong redshift evolution ($\sim$20 per cent between $z = 0$ and $z = 1$), which would appear as a fractional intrinsic scatter with an rms of $\simeq$0.1 in our analysis.[4] Finally, our assumption that the noise in the SZ map pixels is uncorrelated is not strictly correct. This results in a slight underestimate of the SZ measurement noise in the derived temperature profiles, which directly translates to an overestimate of the intrinsic scatter. By comparing to the results of S13, see Fig. 8, which are based on identical Bolocam SZ data and do account for the noise non-idealities, we estimate that the unaccounted for noise is equivalent to a fractional intrinsic scatter of 0.3 in our derived temperature profiles.[5] In sum, given that Mantz et al. (2016) measure a fractional intrinsic scatter of 0.1 in their X-ray analysis, we expect to measure a value of $\sqrt{0.1^2 + 0.15^2 + 0.1^2 + 0.3^2} \simeq 0.35$ after accounting for the three effects described above, in reasonable agreement with our actual measurements. Furthermore, as noted in Section 5.2, our analysis of mock cluster observations hints at a possible overestimate of the fractional intrinsic scatter in temperature (by a factor of $\simeq$0.1 for one of the four test clusters). Therefore, some of the remaining discrepancy between the expected measure value of 0.35 and our actual measured values of 0.4–0.5 may be due to a fitting bias.

[4]Temperature profiles of high-mass relaxed clusters, such as those in the Mantz et al. (2016) sample, are not expected to noticeably evolve with redshift, and therefore would not include this additional scatter.

[5]Fully accounting for the SZ noise correlations requires a bootstrap-like sampling of noise realizations, which is not computationally tractable for our MCMC fits. Therefore, to obtain a rough estimate of the impact of the unaccounted-for noise on our scatter results, we artificially increased the per-cluster SZ noise until the pressure-intrinsic scatter values were approximately equal to those obtained by S13. We then recomputed the temperature-intrinsic scatters using the artificially increased SZ noise estimates, and the quadrature difference compared to the intrinsic scatter values obtained from our nominal analysis corresponds to a fractional scatter of 0.3.

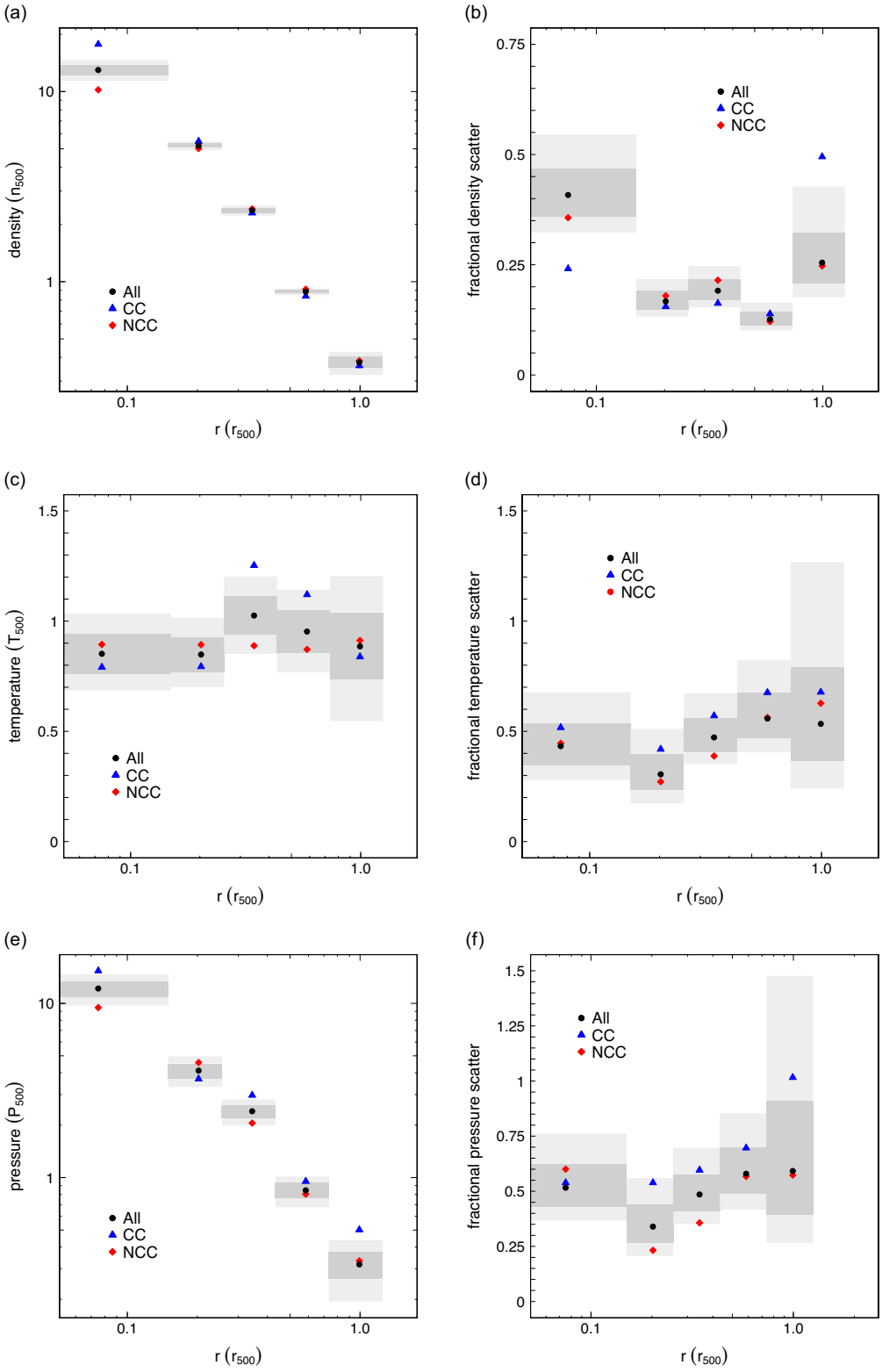

Figure 7. The left-hand column shows the mean density (a), temperature (c), and pressure (e) profiles for the full sample, CC and NCC subsets (scaled according to the self-similar values given in Section 4.2). The grey shaded regions are the 68 per cent and 95 per cent confidence regions for the meta-analysis of the full sample. The confidence regions for the CC and NCC subsets are slightly larger in size, and have been omitted for clarity. The right-hand column shows the fractional intrinsic scatter about the mean profiles.

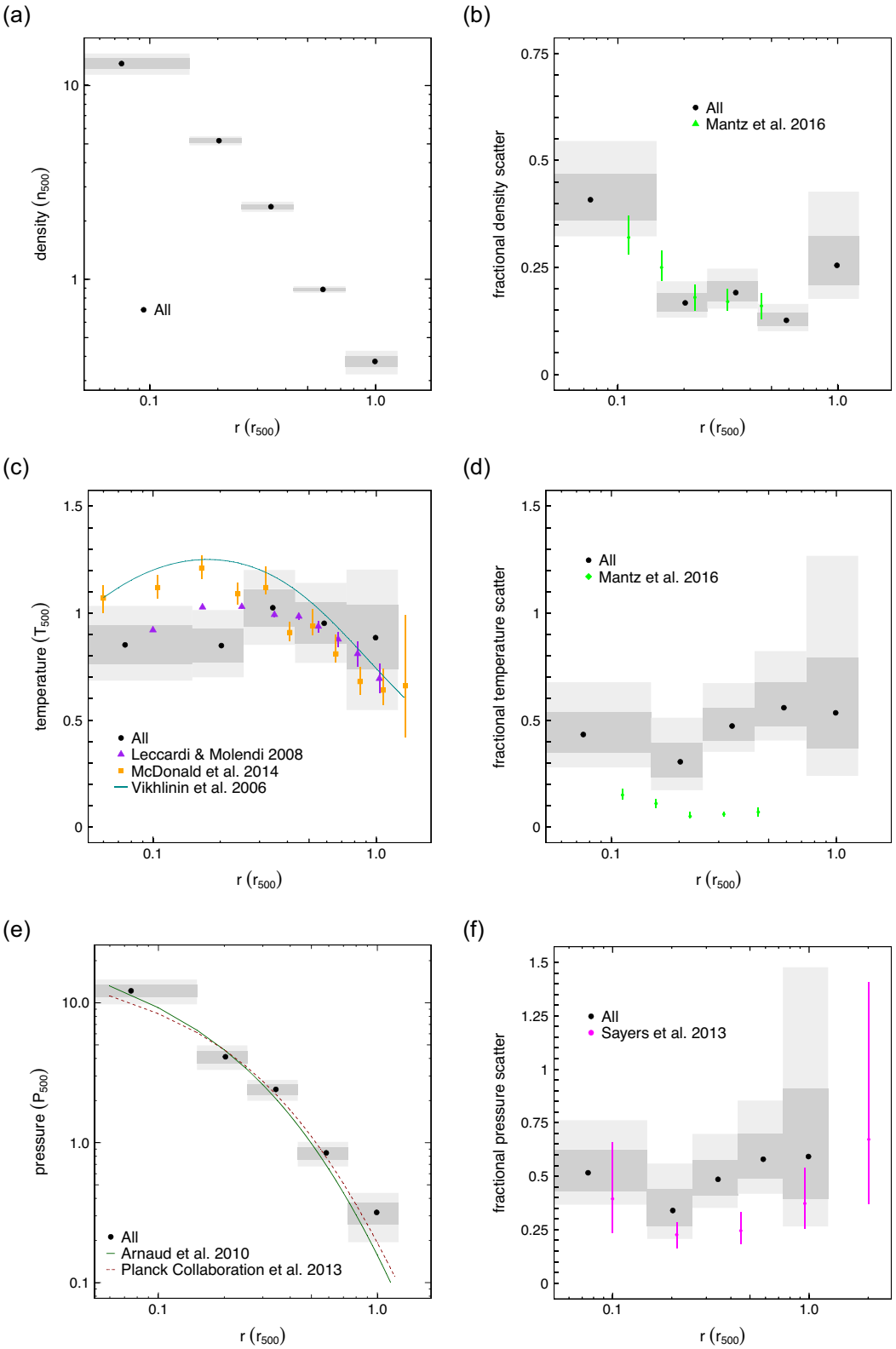

Figure 8. The same plot as Fig. 7, but compared to other studies. The left-hand column shows the mean density (a), temperature (c), and pressure (e) profiles for the full sample (scaled according to the self-similar values given in Section 4.2). The grey shaded regions are the 68 per cent and 95 per cent confidence regions for the full sample. The right-hand column shows the fractional intrinsic scatter about the mean profiles. The green points in the density and temperature scatter profiles are from Mantz et al. (2016), the dark cyan line in the temperature profile is from Vikhlinin et al. (2006), the purple triangles in the temperature profile are from Leccardi & Molendi (2008), the orange squares in the temperature profile are from the low-z sample from McDonald et al. (2014), the dark green solid line in the pressure profile is from Arnaud et al. (2010), the dark red dashed line in the pressure profile is from Planck Collaboration V (2013), while the magenta points are from S13.

7 CONCLUSIONS

We have obtained individual cluster density and temperature profiles extending to $\simeq r_{500}$ for the BOXSZ sample of 45 clusters using a combination of X-ray surface brightness and SZ measurements. The profiles extend to larger radii than can typically be probed using X-ray spectroscopy (e.g. a factor of $\simeq$2 compared to the ACCEPT analysis), although with modest signal to noise limited mainly by the SZ data. The recovered profiles show some differences with previous X-ray spectroscopic studies, most notably the general lack of a temperature drop at large radii. While this may be due to noise fluctuations, it could also be related to systematic errors in X-ray background subtraction, clumping in the ICM, cluster elongation, and/or a slight bias in the Bolocam SZ data at large radii.

We applied a meta-analysis method based on individual cluster deprojections to obtain ensemble-average-scaled deprojections for the density and temperature and their intrinsic scatters. These were computed at a set of common radii extending to $1.25r_{500}$. In general, our results for the ensemble-average density profiles agree with previous works. For example, we find that the fractional intrinsic scatter in the density profiles is highest near the centre of the cluster, where a range of non-gravitational processes occur, lowest in the intermediate regions where the cluster is more regular, and then increasing at larger radii (r_{500}) where active accretion of new material onto the cluster is occurring.

The ensemble-average temperature profile we recover is also in good agreement with previous results. We did not detect a significant drop in temperature near the cluster centre, even for the CC subset, due mainly to the coarse angular resolution of the SZ data which limit the innermost shell to a radius of $0.15r_{500}$. In fact, our temperature profile is relatively flat, but we do not have the constraining power to differentiate between a flat profile and the large radius decrease seen in other studies. Differences between the temperature profile and previous studies may be due to selection effects, noise fluctuations, X-ray background subtraction, ICM clumping, cluster elongation, and/or a slight bias in the SZ data at large radii.

The 0.4–0.5 fractional intrinsic scatter we obtained for the temperature profile is significantly larger than previous results (e.g. $\lesssim$ 0.1 by Mantz et al. 2016). As detailed in Section 6, this difference is not fully understood but is thought to be caused by a combination of several effects. In particular, line-of-sight differences in the SZ and X-ray signals, combined with departures from spherical symmetry, are estimated to increase the fractional intrinsic scatter by $\simeq$0.15 in our analysis compared to X-ray spectroscopic analyses. Furthermore, redshift evolution in the average temperature profile of diverse cluster populations, such as the BOXSZ sample, is estimated to contribute an additional fractional intrinsic scatter of $\simeq$0.1 in our analysis. In addition, our assumption that the noise in the SZ maps is uncorrelated between pixels is not strictly valid, and results in a slight underestimate of the SZ measurement noise, which in turn produces an overestimate of the fractional intrinsic scatter. Finally, there are indications of a slight bias in our fitting method that results in overestimated temperature intrinsic scatters. In sum, these effects largely explain the difference between our temperature intrinsic scatter measurements and those based on X-ray spectroscopy.

This work further supports the universality of cluster pressure profiles. The joint X-ray/SZ method described here can be applied to higher resolution SZ observations to strengthen the constraints of thermodynamic quantities at larger radii, especially temperature, without the dependence on X-ray spectroscopy. As SZ observations improve, the large uncertainties of the individual and mean temperature profiles as seen in this work will decrease.

ACKNOWLEDGEMENTS

Computation for the work described in this paper was supported by the University of Southern California's Center for High-Performance Computing (http://hpcc.usc.edu). JAS would like to thank the Women in Science and Engineering (WiSE) Program at USC for financial support. Silvia Ameglio was supported by the USC WiSE postdoctoral fellowship and the NSF ADVANCE AST-0649899. EP wishes to thank the Aspen Center for Physics for hospitality during part of the preparation of this work. JS was partially supported by NSF/AST-1617022.

REFERENCES

Adam R. et al., 2016, A&A, 586, A122
Allen S. W., Rapetti D. A., Schmidt R. W., Ebeling H., Morris R. G., Fabian A. C., 2008, MNRAS, 383, 879
Ameglio S., Borgani S., Pierpaoli E., Dolag K., 2007, MNRAS, 382, 397
AMI Consortium, 2012, MNRAS, 425, 162
Amodeo S., Ettori S., Capasso R., Sereno M., 2016, A&A, 590, A126
Arnaud K. A., 1996, in Jacoby G. H., Barnes J. eds, ASP Conf. Ser. Vol. 101, Astronomical Data Analysis Software and Systems V. Astron. Soc. Pac., San Francisco, p. 17
Arnaud M., Pratt G. W., Piffaretti R., Böhringer H., Croston J. H., Pointecouteau E., 2010, A&A, 517, A92
Baldi A., Ettori S., Mazzotta P., Tozzi P., Borgani S., 2007, ApJ, 666, 835
Barnes D. J., Kay S. T., Henson M. A., McCarthy I. G., Schaye J., Jenkins A., 2017, MNRAS, 465, 213
Basu K. et al., 2010, A&A, 519, A29
Battaglia N., Bond J. R., Pfrommer C., Sievers J. L., 2012, ApJ, 758, 75
Biffi V. et al., 2017, MNRAS, 468, 531
Blackburn J. K., 1995, in Shaw R. A., Payne H. E., Hayes J. J. E. eds, ASP Conf. Ser. Vol. 77, Astronomical Data Analysis Software and Systems IV. Astron. Soc. Pac., San Francisco, p. 367
Böhringer H., Soucail G., Mellier Y., Ikebe Y., Schuecker P., 2000, A&A, 353, 124
Bonamente M., Joy M. K., LaRoque S. J., Carlstrom J. E., Reese E. D., Dawson K. S., 2006, ApJ, 647, 25
Bonamente M., Landry D., Maughan B., Giles P., Joy M., Nevalainen J., 2013, MNRAS, 428, 2812
Boschin W., Girardi M., Barrena R., Biviano A., Feretti L., Ramella M., 2004, A&A, 416, 839
Bourdin H., Mazzotta P., Kozmanyan A., Jones C., Vikhlinin A., 2017, ApJ, 843, 72
Bradač M., Allen S. W., Treu T., Ebeling H., Massey R., Morris R. G., von der Linden A., Applegate D., 2008, ApJ, 687, 959
Canning R. E. A. et al., 2017, MNRAS, 464, 2896
Carlstrom J. E., Holder G. P., Reese E. D., 2002, ARA&A, 40, 643
Cavagnolo K. W., Donahue M., Voit G. M., Sun M., 2009, ApJS, 182, 12
Coe D. et al., 2012, ApJ, 757, 22
Cooray A. R., 2000, MNRAS, 313, 783
Czakon N. G. et al., 2015, ApJ, 806, 18
De Filippis E., Sereno M., Bautz M. W., Longo G., 2005, ApJ, 625, 108
de Haan T. et al., 2016, ApJ, 832, 95
Diego J. M., Broadhurst T., Zitrin A., Lam D., Lim J., Ford H. C., Zheng W., 2015, MNRAS, 451, 3920
Donahue M., Gaskin J. A., Patel S. K., Joy M., Clowe D., Hughes J. P., 2003, ApJ, 598, 190
Donahue M. et al., 2014, ApJ, 794, 136
Donnarumma A., Ettori S., Meneghetti M., Moscardini L., 2009, MNRAS, 398, 438

Donnarumma A. et al., 2011, A&A, 528, A73
Ebeling H., Barrett E., Donovan D., Ma C.-J., Edge A. C., van Speybroeck L., 2007, ApJ, 661, L33
Eckert D. et al., 2012, A&A, 541, A57
Eckert D., Molendi S., Vazza F., Ettori S., Paltani S., 2013a, A&A, 551, A22
Eckert D., Ettori S., Molendi S., Vazza F., Paltani S., 2013b, A&A, 551, A23
Ehlert S. et al., 2011, MNRAS, 411, 1641
Ferrari C. et al., 2011, A&A, 534, L12
Gardini A., Rasia E., Mazzotta P., Tormen G., De Grandi S., Moscardini L., 2004, MNRAS, 351, 505
George E. M. et al., 2015, ApJ, 799, 177
Ghirardini V., Ettori S., Eckert D., Molendi S., Gastaldello F., Pointecouteau E., Hurier G., Bourdin H., 2018, A&A, 614, A7
Giacintucci S., Markevitch M., Venturi T., Clarke T. E., Cassano R., Mazzotta P., 2014, ApJ, 781, 9
Gilmour R., Best P., Almaini O., 2009, MNRAS, 392, 1509
Gioia I. M., Braito V., Branchesi M., Della Ceca R., Maccacaro T., Tran K.-V., 2004, A&A, 419, 517
Girardi M., Demarco R., Rosati P., Borgani S., 2005, A&A, 442, 29
Girardi M., Boschin W., Barrena R., 2006, A&A, 455, 45
Gómez P. L. et al., 2012, AJ, 144, 79
Grego L., Carlstrom J. E., Joy M. K., Reese E. D., Holder G. P., Patel S., Cooray A. R., Holzapfel W. L., 2000, ApJ, 539, 39
Gu L. et al., 2009, ApJ, 700, 1161
Hlavacek-Larrondo J. et al., 2013, ApJ, 777, 163
Huo Z.-Y., Xue S.-J., Xu H., Squires G., Rosati P., 2004, AJ, 127, 1263
Ichikawa K. et al., 2013, ApJ, 766, 90
Jauzac M. et al., 2015, MNRAS, 446, 4132
Jee M. J., Tyson J. A., 2009, ApJ, 691, 1337
Jee M. J. et al., 2007, ApJ, 661, 728
Jiménez-Bailón E., Lozada-Muñoz M., Aguerri J. A. L., 2013, Astronomische Nachrichten, 334, 377
Kaiser N., 1986, MNRAS, 222, 323
Kartaltepe J. S., Ebeling H., Ma C. J., Donovan D., 2008, MNRAS, 389, 1240
Komatsu E. et al., 2001, PASJ, 53, 57
Korngut P. M. et al., 2011, ApJ, 734, 10
Kotov O., Vikhlinin A., 2005, ApJ, 633, 781
Kotov O., Vikhlinin A., 2006, ApJ, 641, 752
Landry D., Bonamente M., Giles P., Maughan B., Joy M., Murray S., 2013, MNRAS, 433, 2790
LaRoque S. J. et al., 2003, ApJ, 583, 559
LaRoque S. J., Bonamente M., Carlstrom J. E., Joy M. K., Nagai D., Reese E. D., Dawson K. S., 2006, ApJ, 652, 917
Lau E. T., Kravtsov A. V., Nagai D., 2009, ApJ, 705, 1129
Lau E. T., Nagai D., Avestruz C., Nelson K., Vikhlinin A., 2015, ApJ, 806, 68
Leccardi A., Molendi S., 2008, A&A, 486, 359
Limousin M. et al., 2010, MNRAS, 405, 777
Limousin M. et al., 2016, A&A, 588, A99
Lu T. et al., 2010, MNRAS, 403, 1787
Mahdavi A., Hoekstra H., Babul A., Bildfell C., Jeltema T., Henry J. P., 2013, ApJ, 767, 116
Ma C.-J., Ebeling H., Barrett E., 2009, ApJ, 693, L56
Mann A. W., Ebeling H., 2012, MNRAS, 420, 2120
Mantz A., Allen S. W., Rapetti D., Ebeling H., 2010a, MNRAS, 406, 1759
Mantz A., Allen S. W., Ebeling H., Rapetti D., Drlica-Wagner A., 2010b, MNRAS, 406, 1773
Mantz A. B., Allen S. W., Morris R. G., Schmidt R. W., 2016, MNRAS, 456, 4020
Massardi M., Ekers R. D., Ellis S. C., Maughan B., 2010, ApJ, 718, L23
Maughan B. J., Ellis S. C., Jones L. R., Mason K. O., Córdova F. A., Priedhorsky W., 2006, ApJ, 640, 219
Maughan B. J., Jones C., Jones L. R., Van Speybroeck L., 2007, ApJ, 659, 1125
Maughan B. J., Jones C., Forman W., Van Speybroeck L., 2008, ApJS, 174, 117
Maughan B. J., Giles P. A., Randall S. W., Jones C., Forman W. R., 2012, MNRAS, 421, 1583
Mazzotta P., Rasia E., Moscardini L., Tormen G., 2004, MNRAS, 354, 10
McDonald M. et al., 2014, ApJ, 794, 67
McLaughlin D. E., 1999, AJ, 117, 2398
Medezinski E., Broadhurst T., Umetsu K., Oguri M., Rephaeli Y., Benítez N., 2010, MNRAS, 405, 257
Medezinski E. et al., 2013, ApJ, 777, 43
Mercurio A., Girardi M., Boschin W., Merluzzi P., Busarello G., 2003, A&A, 397, 431
Metzger M. R., Ma C.-P., 2000, AJ, 120, 2879
Mohammed I., Saha P., Williams L. L. R., Liesenborgs J., Sebesta K., 2016, MNRAS, 459, 1698
Morandi A., Limousin M., 2012, MNRAS, 421, 3147
Morandi A., Pedersen K., Limousin M., 2010, ApJ, 713, 491
Morandi A. et al., 2012, MNRAS, 425, 2069
Morandi A., Sun M., Forman W., Jones C., 2015, MNRAS, 450, 2261
Mroczkowski T. et al., 2009, ApJ, 694, 1034
Mroczkowski T. et al., 2012, ApJ, 761, 47
Nagai D., Kravtsov A. V., Vikhlinin A., 2007, ApJ, 668, 1
Neumann D. M., Arnaud M., 2000, ApJ, 542, 35
Newman A. B., Treu T., Ellis R. S., Sand D. J., Nipoti C., Richard J., Jullo E., 2013, ApJ, 765, 24
Nord M. et al., 2009, A&A, 506, 623
Ogrean G. A. et al., 2015, ApJ, 812, 153
Ota N., Pointecouteau E., Hattori M., Mitsuda K., 2004, ApJ, 601, 120
Paulin-Henriksson S., Antonuccio-Delogu V., Haines C. P., Radovich M., Mercurio A., Becciani U., 2007, A&A, 467, 427
Piffaretti R., Arnaud M., Pratt G. W., Pointecouteau E., Melin J.-B., 2011, A&A, 534, A109
Plagge T. et al., 2010, ApJ, 716, 1118
Planck Collaboration V, 2013, A&A, 550, A131
Planck Collaboration XI, 2016a, A&A, 594, A11
Planck Collaboration XXIV, 2016b, A&A, 594, A24
Planelles S. et al., 2017, MNRAS, 467, 3827
Pointecouteau E., Giard M., Benoit A., Désert F. X., Bernard J. P., Coron N., Lamarre J. M., 2001, ApJ, 552, 42
Poole G. B., Fardal M. A., Babul A., McCarthy I. G., Quinn T., Wadsley J., 2006, MNRAS, 373, 881
Postman M. et al., 2012, ApJS, 199, 25
Rasia E., Mazzotta P., Borgani S., Moscardini L., Dolag K., Tormen G., Diaferio A., Murante G., 2005, ApJ, 618, L1
Rasia E., Mazzotta P., Bourdin H., Borgani S., Tornatore L., Ettori S., Dolag K., Moscardini L., 2008, ApJ, 674, 728
Rasia E. et al., 2015, ApJ, 813, L17
Reiprich T. H. et al., 2009, A&A, 501, 899
Richard J., Kneib J.-P., Limousin M., Edge A., Jullo E., 2010, MNRAS, 402, L44
Roncarelli M., Ettori S., Dolag K., Moscardini L., Borgani S., Murante G., 2006, MNRAS, 373, 1339
Ruppin F. et al., 2017, A&A, 597, A110
Sanders J. S., Fabian A. C., Taylor G. B., 2005, MNRAS, 356, 1022
Sanders J. S., Fabian A. C., Taylor G. B., 2009, MNRAS, 393, 71
Sarazin C. L., 1988, X-Ray Emission from Clusters of Galaxies. Cambridge Univ. Press, Cambridge
Sayers J., Golwala S. R., Ameglio S., Pierpaoli E., 2011, ApJ, 728, 39
Sayers J. et al., 2013a, ApJ, 764, 152
Sayers J. et al., 2013b, ApJ, 768, 177 (S13)
Sayers J. et al., 2013c, ApJ, 778, 52
Sayers J. et al., 2016, ApJ, 832, 26
Schellenberger G., Reiprich T. H., Lovisari L., Nevalainen J., David L., 2015, A&A, 575, A30
Siegel S. R. et al., 2018, ApJ, 861, 71
Solovyeva L., Anokhin S., Sauvageot J. L., Teyssier R., Neumann D., 2007, A&A, 476, 63
Tyson J. A., Kochanski G. P., Dell'Antonio I. P., 1998, ApJ, 498, L107
Umetsu K., Medezinski E., Broadhurst T., Zitrin A., Okabe N., Hsieh B.-C., Molnar S. M., 2010, ApJ, 714, 1470

Umetsu K. et al., 2012, ApJ, 755, 56
Umetsu K., Zitrin A., Gruen D., Merten J., Donahue M., Postman M., 2016, ApJ, 821, 116
Vazza F., Eckert D., Simionescu A., Brüggen M., Ettori S., 2013, MNRAS, 429, 799
Verdugo T., de Diego J. A., Limousin M., 2007, ApJ, 664, 702
Vikhlinin A., Kravtsov A., Forman W., Jones C., Markevitch M., Murray S. S., Van Speybroeck L., 2006, ApJ, 640, 691
Vikhlinin A. et al., 2009, ApJ, 692, 1060
Worrall D. M., Birkinshaw M., 2003, MNRAS, 340, 1261
Zhang Y.-Y., Böhringer H., Mellier Y., Soucail G., Forman W., 2005, A&A, 429, 85
Zitrin A., Broadhurst T., Barkana R., Rephaeli Y., Benítez N., 2011, MNRAS, 410, 1939

APPENDIX A: JOINT CLUSTER LIKELIHOOD

A full global-likelihood method was also implemented on the data. Instead of fitting to individual cluster deprojected profiles, this method fits directly to both X-ray and SZ data for clusters simultaneously. This approach models more directly what happens in reality, and therefore accounts more clearly for the various sources of errors (including sample variance) as well as non-linearities in the dependences between physical quantities and observables.

Given the common rescaling of r_{500}, $n_{\mathrm{e},500}$, and T_{500} described in Section 4.2, we modelled the density and temperature as constant values within each radial shell. As with the ensemble analysis of Section 4.2, identical radial shells (in units of r_{500}) were used for all 45 clusters. Specifically, we assumed that within each radial shell of each cluster, the actual density and temperature values are a random realization based on a single universal mean value for that bin (identical for all clusters), and its intrinsic scatter for that shell. The clusters were modelled assuming five radial shells, so 20 parameters were included in the fit: 5 universal mean densities, 5 universal mean temperatures, 5 density-intrinsic scatters, and 5 temperature-intrinsic scatters. The global likelihood aims to determine these 20 parameters by simultaneously fitting to the SZ and X-ray data from all of the clusters within a given sample. In the likelihood, the stochastic nature of the cluster modelling is implemented within the MCMC approach for the likelihood determination. Specifically, whenever the MCMC code determines the likelihood for a given set of these 20 parameters, the model-predicted value within each radial shell for each individual cluster is randomly drawn based on a Gaussian distribution centred on the universal mean value with a standard deviation equal to the intrinsic scatter value. More explicitly, the modelling of the physical properties for cluster k at each iteration of the MCMC code practically reads:

$$\mathbb{T}_{i,k} = \bar{\mathbb{T}}_i + \mathrm{ran}_k(\sigma_{\mathbb{T}i}) \tag{A1}$$

and

$$\mathbb{N}_{i,k} = \bar{\mathbb{N}}_i + \mathrm{ran}_k(\sigma_{\mathbb{N}i}) \tag{A2}$$

where $\boldsymbol{i}$ is the radial shell, $\boldsymbol{k}$ represents the cluster, $\bar{\mathbb{T}}_i$ and $\bar{\mathbb{N}}_i$ are the universal mean values of the temperature and density in radial shell $\boldsymbol{i}$ (in units of T_{500} and $n_{\mathrm{e},500}$), and $\mathrm{ran}_k(\sigma_{\mathbb{T}i})$ and $\mathrm{ran}_k(\sigma_{\mathbb{N}i})$ indicate random draws for each cluster k from Gaussian distributions with the given standard deviation for that MCMC draw (e.g. $\sigma_{\mathbb{T}i}$).

The joint likelihood of all clusters using both the SZ and X-ray observations reads

$$ln(\mathcal{L}) = \sum_k \left(\sum_j -\frac{1}{2}\frac{(O_{\mathrm{SZ},j,k} - M_{\mathrm{SZ},j,k})^2}{\sigma^2_{\mathrm{SZ},j,k}} - \sum_i \frac{1}{2}\frac{(O_{\text{X-ray},i,k} - M_{\text{X-ray},i,k})^2}{M_{\text{X-ray},i,k}} - \frac{1}{2} ln(2\pi M_{\text{X-ray},i,k}) \right) \tag{A3}$$

where k again indicates a given cluster, j indicates a single SZ map pixel, and i indicates a single projected radial shell for the X-ray data. O denotes the observed SZ or X-ray brightness, and M gives the model-predicted SZ or X-ray brightness based on the temperature and density from equations (A1) and (A2) and the relations provided in equations (5), (6), (11), and (12). Given equations (A1) and (A2), M naturally contain information about the universal intrinsic scatters in temperature and density. The fitting procedure is thus fitting directly to the SZ map pixels and X-ray-projected bins for all clusters simultaneously. Note that, although the likelihood is assumed to be Gaussian in the observables, it is not Gaussian in the parameters (the X-ray emission has a quadratic dependence on density and a non-linear dependence on temperature while the SZ brightness is proportional to the product of density and temperature). The weight of each individual cluster in the global likelihood reflects the quality of the observational data, and clusters with higher SZ noise σ_{SZ} and/or fewer X-ray source photons may have very little influence on the overall constraints. Indeed, for our sample, the total weighting factors vary from cluster to cluster by approximately two orders of magnitude. Furthermore, in determining the uncertainties on the intrinsic scatter values, this expression correctly accounts for the finite cluster sample size. Finally, uncertainties in the X-ray measured values of M_{500} and r_{500} could easily be accounted for in the likelihood expression, although they were not included in the present analysis.

We implemented this global likelihood in an MCMC, and analysed CC clusters separately from NCC ones due to the expected difference in behaviour of the density and temperature profiles in the clusters' centres. This split also reduced the number of clusters in a given MCMC from 45 to ∼20, and allowed the fits to converge in a reasonable amount of time, several weeks, with our available computing resources. For these fits, the only quantities that are meaningfully constrained are the ensemble mean density profiles and their intrinsic scatter, which are reported in Section 6.2. The ensemble mean temperature profiles and their intrinsic scatter have large uncertainties and are therefore poorly constrained. The cause of these poor constraints is not fully understood, but we suspect it may be related to the relatively small samples sizes used in our MCMC fits combined with the large differences in cluster weighting factors, which effectively reduce the sample sizes even further.

This approach, while it has a clean interpretation and full retention of information in the data, did not produce satisfactory results for the temperature analysis. Furthermore, it was not computationally tractable to apply this approach to the full cluster sample. Therefore, an alternative method was adopted in the main section of the paper, based on a meta-analysis of the individual clusters' deprojections.

The density profiles for CC and NCC clusters obtained with this method are reported in Fig. A1, together with their uncertainties. The mean density profiles show good agreement with the results obtained with the meta-analysis of Section 4.2, which are also plotted

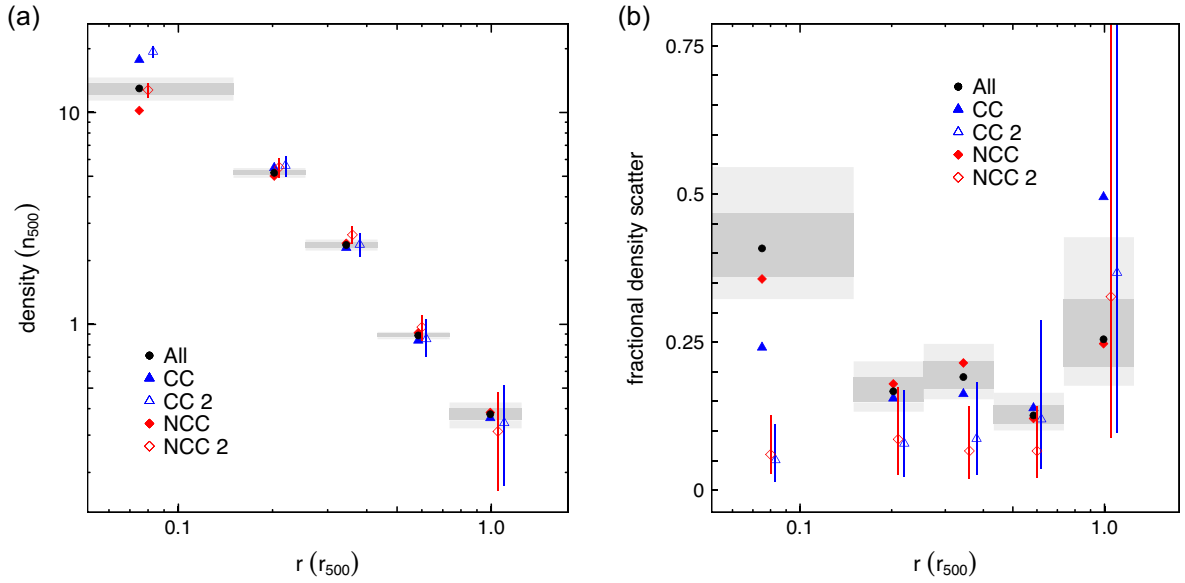

Figure A1. The left-hand column shows the mean density (a) profiles for the full sample, CC, and NCC subsets (scaled according to the self-similar values given in this appendix). The solid points correspond to the results obtained from the meta-analysis of Section 4.2, which include the full sample, CC, and NCC subsets, denoted by All, CC, and NCC. The hollow points correspond to the results obtained from the full-likelihood method of this appendix, and only includes the CC and NCC subsets, denoted by CC 2 and NCC 2. The full sample was not fitted for with this method due to computational constraints. The grey shaded regions are the 68 per cent and 95 per cent confidence regions for the meta-analysis of the full sample. The confidence regions for the CC and NCC subsets are slightly larger in size, and have been omitted for clarity. The right column (b) shows the fractional intrinsic scatter about the mean profile.

in the same panels.The joint likelihood method also finds a higher density in the innermost shell for the CC clusters compared to the NCC clusters. The intrinsic scatters about the mean density obtained from the joint likelihood are generally smaller than those obtained from the meta-analysis, although the difference is only significant in the innermost shell. The reason for this is not clear. Furthermore, the density scatter values are consistent for both the CC and the NCC samples (and for the full sample in the meta-analysis).

APPENDIX B: INDIVIDUAL CLUSTER RESULTS

Table B1. Goodness of fit details.

			Concentric shell deprojections						Smooth parametric profiles					
	X-ray proj. bins	SZ map pixels	χ^2_{XR}	χ^2_{SZ}	χ^2_{tot}	dof	χ^2_{red}	PTE	χ^2_{XR}	χ^2_{SZ}	χ^2_{tot}	dof	χ^2_{red}	PTE
Abell 2204	77	1677	1239.55	1864.14	3103.69	1744	1.782	0.000	82.23	2116.02	2198.25	1745	1.260	0.000
Abell 383	58	1388	742.58	1453.50	2196.08	1437	1.531	0.000	76.86	1481.79	1558.65	1440	1.082	0.015
Abell 1423	44	1577	170.90	1650.79	1821.69	1612	1.132	0.000	84.87	1666.52	1751.39	1616	1.084	0.010
Abell 209	61	905	903.42	1046.86	1950.28	957	2.044	0.000	94.05	1044.52	1138.57	961	1.185	0.000
Abell 963	71	1518	1318.75	1574.04	2892.79	1580	1.834	0.000	145.30	1580.28	1725.58	1582	1.091	0.006
Abell 2261	76	1739	821.29	1809.37	2630.66	1806	1.459	0.000	119.87	1809.71	1929.58	1808	1.067	0.023
Abell 2219	83	1566	3319.62	1473.09	4792.71	1640	2.928	0.000	236.06	1503.62	1739.68	1644	1.058	0.050
Abell 267	45	772	190.82	723.02	913.84	808	1.135	0.004	48.83	731.71	780.54	812	0.961	0.781
RX J2129.6+005	33	484	215.22	536.87	752.09	508	1.489	0.000	205.88	543.01	748.90	513	1.460	0.000
Abell 1835	92	1644	2504.11	2045.04	4549.15	1727	2.639	0.000	137.73	2015.50	2153.23	1728	1.246	0.000
Abell 697	63	1649	493.01	1992.64	2485.65	1703	1.462	0.000	76.08	1980.35	2056.43	1707	1.205	0.000
Abell 611	63	1181	639.14	1176.02	1815.16	1235	1.473	0.000	92.22	1178.70	1270.92	1237	1.027	0.245
MS 2137.3−2353	63	1186	638.81	1186.75	1825.56	1240	1.476	0.000	354.59	1218.05	1572.64	1243	1.265	0.000
MACS J1931.8−2634	52	537	2473.80	546.03	3019.83	580	5.234	0.000	47.35	541.69	589.04	581	1.014	0.400
Abell S1063	77	1724	1135.82	1804.71	2940.53	1792	1.644	0.000	91.97	1818.45	1910.42	1793	1.065	0.027
MACS J1115.8+0129	63	940	734.66	1067.39	1802.05	993	1.820	0.000	55.30	1062.86	1118.16	995	1.124	0.004
Abell 370	14	710	32.71	759.25	791.96	717	1.109	0.022	16.32	776.02	792.34	720	1.100	0.031
ZWCL 0024+17	59	936	156.86	1006.99	1163.85	986	1.184	0.000	121.68	1010.19	1131.87	991	1.142	0.001
MACS J1532.9+3021	33	1352	678.70	1456.80	2135.50	1376	1.555	0.000	28.75	1456.93	1485.68	1379	1.077	0.023
MACS J0429.6−0253	25	424	281.17	523.59	804.76	440	1.842	0.000	27.21	524.98	552.20	441	1.252	0.000
MACS J2211.7−0349	43	1154	459.67	1196.37	1656.04	1188	1.397	0.000	45.78	1209.27	1255.05	1193	1.052	0.103
MACS J1720.3+3536	34	462	240.01	562.42	802.42	487	1.658	0.000	43.06	558.44	601.51	489	1.230	0.000
MACS J0416.1−2403	24	351	61.71	348.03	409.73	367	1.126	0.049	40.28	399.27	439.55	371	1.185	0.008
MACS J0451.9+0006	16	634	36.03	363.97	399.99	329	1.227	0.003	14.61	669.80	684.41	646	1.059	0.143
MACS J0417.5−1154	102	1730	1767.26	1878.09	3645.35	1823	2.003	0.000	377.11	1887.78	2264.89	1823	1.242	0.000
MACS J1206.2−0847	42	733	256.18	757.47	1013.65	766	1.329	0.000	64.60	766.82	831.43	767	1.084	0.053
MACS J0329.6−0211	23	400	138.60	428.76	567.36	414	1.380	0.000	29.77	431.00	460.77	415	1.110	0.060
MACS J1347.5−1144	61	780	1816.78	803.91	2620.69	832	3.161	0.000	139.62	811.80	951.43	832	1.144	0.002
MACS J1311.0−0310	24	185	501.62	165.11	666.73	200	3.384	0.000	28.20	179.26	207.46	203	1.022	0.400
MACS J0257.1−2325	28	500	118.57	476.42	594.99	519	1.153	0.009	27.72	493.29	521.01	524	0.994	0.529
MACS J0911.2+1746	27	516	76.38	561.55	637.93	535	1.199	0.001	37.56	566.92	604.49	538	1.124	0.024
MACS J2214.9−1359	28	560	107.70	704.66	812.35	666	1.225	0.000	41.57	658.15	699.72	582	1.202	0.001
MACS J0018.5+1626	58	703	351.40	738.41	1089.80	752	1.455	0.000	94.48	772.25	866.73	755	1.148	0.003
MACS J1149.5+2223	34	622	123.26	683.70	806.95	648	1.251	0.000	47.09	685.74	732.82	652	1.124	0.015
MACS J0717.5+3745	58	700	427.05	739.81	1166.86	749	1.564	0.000	57.21	783.68	840.90	751	1.120	0.012
MACS J1423.8+2404	61	732	1383.17	704.84	2088.01	784	2.674	0.000	96.05	702.76	798.82	787	1.015	0.377
MACS J0454.1−0300	56	634	424.26	705.99	1130.25	681	1.667	0.000	180.89	762.28	943.17	686	1.375	0.000
MACS J0025.4−1222	31	199	81.72	230.13	311.85	221	1.431	0.000	37.07	302.52	339.59	226	1.503	0.000
MS 2053.7−0449	11	88	17.72	71.80	89.53	90	1.029	0.405	19.31	72.84	92.16	95	0.970	0.564
MACS J0647.7+7015	23	539	81.28	547.38	628.66	553	1.143	0.011	32.72	557.32	590.04	558	1.057	0.168
MACS J2129.4−0741	21	459	58.28	508.27	566.55	471	1.211	0.001	19.26	570.72	589.98	476	1.239	0.000
MACS J0744.8+3927	28	254	246.58	287.72	534.30	273	1.979	0.000	49.03	294.17	343.20	275	1.248	0.003
MS 1054.4−0321	25	127	80.63	143.74	224.37	143	1.603	0.000	238.61	148.60	387.21	148	2.616	0.000
CL J0152.7−1357	15	155	24.51	218.91	243.41	163	1.521	0.000	26.00	245.55	271.55	166	1.636	0.000
CL J1226.9+3332	14	117	84.30	134.16	218.46	122	1.836	0.000	27.29	125.47	152.76	126	1.212	0.053

Note. The goodness of fit details for both the concentric shell deprojections and smooth parametric profile individual cluster analyses are listed. The second and third columns are the number of X-ray and SZ data points, respectively. The chi-squared values for the X-ray (χ^2_{XR}), SZ (χ^2_{SZ}), and total (χ^2_{tot}) data are given. 'dof' is the total degrees of freedom, 'χ^2_{red}' is the total reduced chi-squared value, and 'PTE' is the probability to exceed.

Table B2. Best-fitting parameters for the smooth parametric profiles.

Cluster	n profile	T profile	$n_{e0,1}$ (10^{-2} cm^{-3})	$r_{c,1}$ (arcsec)	$n_{e0,2}$ (10^{-3} cm^{-3})	$r_{c,2}$ (arcsec)	β	T_0 (keV)	T_{min} (keV)	r_{cool} (arcsec)	r_t (arcsec)
Abell 2204	double-B	CC-full	$22.88^{+0.67}_{-0.67}$	$7.27^{+0.23}_{-0.23}$	$15.40^{+0.74}_{-0.74}$	$50.1^{+2.0}_{-2.1}$	$0.641^{+0.008}_{-0.008}$	$16.8^{+3.9}_{-3.4}$	$3.5^{+1.9}_{-2.0}$	63^{+26}_{-24}	250^{+130}_{-110}
Abell 383	double-B	iso	$13.50^{+0.61}_{-0.62}$	$5.58^{+0.31}_{-0.30}$	20^{+2}_{-18}	25^{+2}_{-24}	$0.601^{+0.006}_{-0.006}$	$7.21^{+0.48}_{-0.48}$	–	–	–
Abell 1423	single-B	NCC	$2.61^{+0.20}_{-0.20}$	$14.4^{+1.0}_{-1.0}$	–	–	$0.497^{+0.005}_{-0.005}$	$16.5^{+6.4}_{-5.4}$	–	–	54^{+31}_{-42}
Abell 209	single-B	NCC	$0.84^{+0.03}_{-0.03}$	$51.4^{+2.1}_{-2.1}$	–	–	$0.586^{+0.008}_{-0.008}$	$11.02^{+0.67}_{-0.67}$	–	–	320^{+140}_{-150}
Abell 963	double-B	NCC	$3.07^{+0.17}_{-0.18}$	$15.9^{+1.7}_{-1.6}$	$8.1^{+1.0}_{-1.1}$	$54.5^{+5.4}_{-5.0}$	$0.663^{+0.014}_{-0.014}$	$10.2^{+2.6}_{-2.3}$	–	–	69^{+32}_{-35}
Abell 2261	double-B	NCC	$4.58^{+0.40}_{-0.41}$	$9.2^{+1.3}_{-1.3}$	$16.2^{+1.9}_{-2.0}$	$30.3^{+2.3}_{-2.3}$	$0.581^{+0.006}_{-0.006}$	$5.6^{+0.5}_{-1.9}$	–	–	148^{+93}_{-91}
Abell 2219	single-B	NCC	$1.06^{+0.01}_{-0.01}$	$67.64^{+0.90}_{-0.94}$	–	–	$0.682^{+0.004}_{-0.004}$	$13.8^{+1.1}_{-1.1}$	–	–	115^{+26}_{-27}
Abell 267	single-B	NCC	$1.19^{+0.04}_{-0.04}$	$35.2^{+1.4}_{-1.4}$	–	–	$0.639^{+0.010}_{-0.010}$	$10.04^{+0.69}_{-0.69}$	–	–	244^{+96}_{-92}
RX J2129.6+005	single-B	iso	$7.17^{+0.33}_{-0.33}$	$9.74^{+0.46}_{-0.46}$	–	–	$0.548^{+0.006}_{-0.006}$	$6.96^{+0.58}_{-0.58}$	–	–	–
Abell 1835	double-B	CC-only-core	$14.06^{+0.30}_{-0.30}$	$8.10^{+0.20}_{-0.21}$	$14.25^{+0.61}_{-0.59}$	$41.2^{+1.5}_{-1.5}$	$0.669^{+0.006}_{-0.006}$	47^{+11}_{-10}	$7.63^{+0.43}_{-0.44}$	275^{+45}_{-45}	–
Abell 697	single-B	NCC	$1.03^{+0.03}_{-0.03}$	$47.8^{+1.4}_{-1.4}$	–	–	$0.639^{+0.008}_{-0.008}$	$10.61^{+0.36}_{-0.36}$	–	–	223^{+68}_{-69}
Abell 611	double-B	NCC	$14.6^{+5.7}_{-5.1}$	$2.30^{+0.75}_{-0.76}$	$19.5^{+1.0}_{-1.0}$	$21.96^{+0.96}_{-0.96}$	$0.597^{+0.006}_{-0.006}$	$9.57^{+0.78}_{-0.75}$	–	–	480^{+510}_{-380}
MS 2137.3−2353	single-B	CC-full	$11.57^{+0.53}_{-0.53}$	$3.25^{+0.13}_{-0.13}$	–	–	$0.491^{+0.002}_{-0.002}$	$30.8^{+5.6}_{-5.7}$	$1.6^{+1.1}_{-1.0}$	$32.4^{+5.5}_{-5.6}$	54^{+12}_{-12}
MACS J1931.8−2634	double-B	CC-full	$17.29^{+0.86}_{-0.73}$	$6.17^{+0.16}_{-0.16}$	$14.01^{+0.84}_{-0.84}$	$30.9^{+1.4}_{-1.4}$	$0.689^{+0.010}_{-0.010}$	35^{+16}_{-13}	$3.0^{+2.0}_{-2.0}$	109^{+40}_{-36}	360^{+240}_{-210}
Abell S1063	double-B	CC-only-core	$3.49^{+0.55}_{-0.58}$	$9.9^{+2.6}_{-2.5}$	$22.1^{+1.4}_{-1.5}$	$33.6^{+1.6}_{-1.5}$	$0.676^{+0.007}_{-0.007}$	63^{+19}_{-19}	$12.1^{+1.0}_{-1.0}$	263^{+68}_{-72}	–
MACS J1115.8+0129	double-B	CC-only-core	$9.02^{+0.35}_{-0.36}$	$7.72^{+0.38}_{-0.39}$	$12.5^{+1.4}_{-1.4}$	$30.1^{+2.6}_{-2.5}$	$0.647^{+0.012}_{-0.012}$	32^{+22}_{-16}	$4.9^{+1.3}_{-1.4}$	145^{+61}_{-59}	–
Abell 370	single-B	iso	$0.58^{+0.04}_{-0.04}$	$52.6^{+5.8}_{-5.6}$	–	–	$0.708^{+0.043}_{-0.043}$	$13.17^{+0.82}_{-0.78}$	–	–	–
ZWCL 0024+17	single-B	iso	$1.49^{+0.11}_{-0.12}$	$9.85^{+0.80}_{-0.79}$	–	–	$0.453^{+0.006}_{-0.006}$	$6.5^{+1.6}_{-1.5}$	–	–	–
MACS J1532.9+3021	single-B	CC-full	$12.35^{+0.40}_{-0.39}$	$8.02^{+0.24}_{-0.24}$	–	–	$0.614^{+0.005}_{-0.005}$	$11.2^{+3.6}_{-3.5}$	$3.6^{+1.4}_{-1.7}$	100^{+61}_{-58}	–
MACS J0429.6−0253	double-B	CC-only-core	$13.5^{+1.0}_{-1.0}$	$4.95^{+0.47}_{-0.46}$	$11.9^{+1.9}_{-1.8}$	$26.7^{+3.5}_{-3.4}$	$0.669^{+0.023}_{-0.022}$	52^{+25}_{-24}	$5.9^{+1.5}_{-1.5}$	165^{+48}_{-52}	–
MACS J2211.7−0349	single-B	iso	$3.14^{+0.08}_{-0.08}$	$23.00^{+0.65}_{-0.65}$	–	–	$0.667^{+0.007}_{-0.007}$	$12.99^{+0.56}_{-0.56}$	–	–	–
MACS J1720.3+3536	double-B	NCC	$8.62^{+0.57}_{-0.54}$	$6.77^{+0.50}_{-0.51}$	$10.16^{+0.75}_{-0.78}$	$35.2^{+2.8}_{-2.7}$	$0.747^{+0.026}_{-0.025}$	$9.8^{+1.7}_{-1.9}$	–	–	77^{+33}_{-39}
MACS J0416.1−2403	single-B	iso	$0.58^{+0.02}_{-0.03}$	$79.3^{+8.1}_{-7.4}$	–	–	$1.10^{+0.11}_{-0.10}$	$7.98^{+0.78}_{-0.77}$	–	–	–
MACS J0451.9+0006	single-B	iso	$1.04^{+0.08}_{-0.08}$	$31.1^{+3.0}_{-3.0}$	–	–	$0.683^{+0.032}_{-0.032}$	$7.06^{+0.68}_{-0.68}$	–	–	–
MACS J0417.5−1154	double-B	CC-full	$8.95^{+0.29}_{-0.29}$	$7.84^{+0.27}_{-0.27}$	$6.58^{+0.17}_{-0.17}$	$64.5^{+1.9}_{-1.9}$	$0.709^{+0.011}_{-0.011}$	$24.0^{+7.1}_{-6.7}$	$6.3^{+2.2}_{-2.7}$	95^{+51}_{-47}	440^{+330}_{-230}
MACS J1206.2−0847	double-B	CC-only-core	$3.88^{+0.39}_{-0.39}$	$12.6^{+2.1}_{-2.1}$	$9.8^{+1.7}_{-1.7}$	$45.9^{+6.2}_{-6.1}$	$0.722^{+0.028}_{-0.027}$	61^{+21}_{-19}	$10.61^{+0.73}_{-0.73}$	265^{+56}_{-61}	–
MACS J0329.6−0211	double-B	CC-only-core	$12.90^{+0.67}_{-0.68}$	$5.78^{+0.37}_{-0.36}$	$8.99^{+0.67}_{-0.68}$	$37.4^{+2.9}_{-2.7}$	$0.749^{+0.028}_{-0.028}$	59^{+20}_{-21}	$8.26^{+0.91}_{-0.95}$	273^{+63}_{-57}	–
MACS J1347.5−1144	double-B	CC-full	$31.6^{+2.9}_{-2.7}$	$3.44^{+0.26}_{-0.28}$	$48.0^{+2.9}_{-2.8}$	$17.13^{+0.68}_{-0.67}$	$0.661^{+0.005}_{-0.005}$	$15.93^{+0.92}_{-0.90}$	$4.7^{+3.6}_{-3.5}$	$22.0^{+8.0}_{-7.2}$	–
MACS J1311.0−0310	double-B	iso	$3.94^{+0.16}_{-0.16}$	$13.3^{+1.2}_{-1.1}$	$7.0^{+0.9}_{-6.0}$	40^{+5}_{-35}	$0.925^{+0.085}_{-0.071}$	$7.00^{+0.71}_{-0.72}$	–	–	–
MACS J0257.1−2325	single-B	iso	$2.74^{+0.14}_{-0.14}$	$14.60^{+0.79}_{-0.79}$	–	–	$0.584^{+0.009}_{-0.009}$	$10.85^{+0.94}_{-0.94}$	–	–	–
MACS J0911.2+1746	single-B	NCC	$0.84^{+0.06}_{-0.06}$	$26.1^{+2.1}_{-2.1}$	–	–	$0.557^{+0.015}_{-0.015}$	$6.5^{+1.3}_{-1.3}$	–	–	390^{+290}_{-260}
MACS J2214.9−1359	single-B	CC-only-core	$1.54^{+0.08}_{-0.08}$	$22.8^{+1.3}_{-1.3}$	–	–	$0.600^{+0.012}_{-0.012}$	$28.2^{+8.4}_{-8.3}$	$6.9^{+2.4}_{-2.5}$	90^{+38}_{-36}	–
MACS J0018.5+1626	double-B	iso	$1.61^{+0.58}_{-0.58}$	$9.1^{+3.7}_{-4.0}$	$10.2^{+0.5}_{-9.7}$	40^{+2}_{-38}	$0.703^{+0.011}_{-0.011}$	$8.46^{+0.40}_{-0.40}$	–	–	–
MACS J1149.5+2223	single-B	iso	$0.68^{+0.03}_{-0.03}$	$52.5^{+2.9}_{-2.9}$	–	–	$0.720^{+0.023}_{-0.023}$	$10.42^{+0.50}_{-0.50}$	–	–	–

Table B2 – *continued*

Cluster	n profile	T profile	$n_{e0,1}$ (10^{-2} cm^{-3})	$r_{c,1}$ (arcsec)	$n_{e0,2}$ (10^{-3} cm^{-3})	$r_{c,2}$ (arcsec)	β	T_0 (keV)	T_{min} (keV)	r_{cool} (arcsec)	r_t (arcsec)
MACS J0717.5+3745	double-B	NCC	$1.36^{+0.14}_{-0.14}$	$20.1^{+2.6}_{-2.5}$	$6.39^{+0.21}_{-0.20}$	$88.4^{+4.2}_{-4.3}$	$1.003^{+0.036}_{-0.037}$	$25.4^{+2.4}_{-2.4}$	–	–	$38.1^{+6.1}_{-6.5}$
MACS J1423.8+2404	single-b	CC-full	$20.2^{+1.3}_{-1.3}$	$3.42^{+0.11}_{-0.11}$	–	–	$0.556^{+0.004}_{-0.004}$	$15.8^{+4.2}_{-3.6}$	$1.68^{+0.70}_{-0.95}$	49^{+17}_{-14}	123^{+46}_{-44}
MACS J0454.1−0300	single-b	iso	$1.79^{+0.04}_{-0.04}$	$25.42^{+0.65}_{-0.64}$	–	–	$0.631^{+0.006}_{-0.006}$	$8.92^{+0.31}_{-0.31}$	–	–	–
MACS J0025.4−1222	single-B	iso	$0.72^{+0.02}_{-0.02}$	$47.5^{+2.3}_{-2.3}$	–	–	$0.878^{+0.032}_{-0.033}$	$5.38^{+0.59}_{-0.58}$	–	–	–
MS 2053.7−0449	single-B	iso	$1.14^{+0.12}_{-0.12}$	$15.6^{+2.2}_{-2.2}$	–	–	$0.604^{+0.035}_{-0.036}$	$4.0^{+1.1}_{-1.1}$	–	–	–
MACS J0647.7+7015	single-B	iso	$2.02^{+0.11}_{-0.11}$	$19.7^{+1.2}_{-1.3}$	–	–	$0.636^{+0.015}_{-0.015}$	$11.76^{+0.52}_{-0.53}$	–	–	–
MACS J2129.4−0741	single-B	iso	$1.85^{+0.11}_{-0.11}$	$19.4^{+1.2}_{-1.3}$	–	–	$0.620^{+0.014}_{-0.014}$	$11.05^{+0.53}_{-0.53}$	–	–	–
MACS J0744.8+3927	double-B	NCC	$8.7^{+1.1}_{-1.0}$	$4.69^{+0.78}_{-0.76}$	$16.4^{+3.1}_{-3.2}$	$20.1^{+3.0}_{-3.0}$	$0.622^{+0.020}_{-0.020}$	$10.7^{+1.8}_{-1.8}$	–	–	96^{+58}_{-57}
MS 1054.4−0321	single-B	iso	$0.68^{+0.01}_{-0.01}$	$71.2^{+3.7}_{-3.6}$	–	–	$1.168^{+0.065}_{-0.063}$	$6.38^{+0.28}_{-0.29}$	–	–	–
CL J0152.7−1357	single-B	iso	$0.26^{+0.01}_{-0.01}$	138^{+12}_{-12}	–	–	$1.717^{+0.282}_{-0.200}$	$6.14^{+0.66}_{-0.66}$	–	–	–
CL J1226.9+3332	single-B	NCC	$0.28^{+0.03}_{-0.03}$	$14.2^{+1.2}_{-1.2}$	–	–	$0.659^{+0.022}_{-0.023}$	$9.95^{+0.65}_{-0.70}$	–	–	420^{+280}_{-260}

Note. The best-fitting parameters for the smooth parametric profiles are listed. The n profile describes whether a single or double-beta density profile was used, while the T profile describes the type of temperature profile: iso (isothermal), NCC (fitting parameters T_0 and r_t), CC-only-core (fitting parameters T_0, T_{cool}, and r_{cool}), or CC-full (all temperature parameters).

Table B3. Best-fitting parameters for the concentric shell deprojections.

Cluster	r_1	r_2	r_3	r_4	r_5	$n_{e,1}$	$n_{e,2}$	$n_{e,3}$	$n_{e,4}$	$n_{e,5}$	$T_{e,1}$	$T_{e,2}$	$T_{e,3}$	$T_{e,4}$	$T_{e,5}$
Abell 2204	0.0537	0.109	0.221	0.448	0.908	$65.07^{+1.71}_{-1.66}$	$22.52^{+0.45}_{-0.45}$	$8.36^{+0.09}_{-0.09}$	$2.40^{+0.03}_{-0.03}$	$0.64^{+0.01}_{-0.01}$	$0.75^{+0.18}_{-0.75}$	$1.16^{+0.3}_{-0.3}$	$1.12^{+0.09}_{-0.09}$	$0.72^{+0.13}_{-0.13}$	$0.23^{+0.05}_{-0.23}$
Abell 383	0.0856	0.166	0.320	0.619	1.200	$33.40^{+0.85}_{-0.87}$	$12.12^{+0.19}_{-0.2}$	$4.21^{+0.06}_{-0.06}$	$1.41^{+0.02}_{-0.02}$	$0.44^{+0.02}_{-0.02}$	$1.53^{+0.36}_{-1.53}$	$0.60^{+0.16}_{-0.6}$	$1.63^{+0.25}_{-0.25}$	$1.93^{+0.3}_{-0.3}$	$0.52^{+0.11}_{-0.52}$
Abell 1423	0.0762	0.151	0.300	0.595	1.180	$20.43^{+0.86}_{-0.81}$	$7.79^{+0.31}_{-0.31}$	$3.28^{+0.09}_{-0.09}$	$1.31^{+0.03}_{-0.03}$	$0.42^{+0.01}_{-0.01}$	$1.26^{+0.3}_{-1.26}$	$1.39^{+0.35}_{-1.39}$	$1.04^{+0.32}_{-0.32}$	$0.81^{+0.3}_{-0.3}$	$0.34^{+0.07}_{-0.34}$
Abell 209	0.0672	0.148	0.324	0.711	1.560	$14.98^{+0.87}_{-0.87}$	$8.95^{+0.23}_{-0.23}$	$4.20^{+0.07}_{-0.07}$	$1.37^{+0.03}_{-0.03}$	$0.41^{+0.01}_{-0.01}$	$1.14^{+0.29}_{-1.14}$	$0.68^{+0.27}_{-0.28}$	$1.15^{+0.13}_{-0.13}$	$0.96^{+0.24}_{-0.24}$	$0.48^{+0.1}_{-0.48}$
Abell 963	0.0762	0.150	0.294	0.578	1.140	$25.69^{+0.92}_{-1.1}$	$11.42^{+0.27}_{-0.24}$	$4.57^{+0.06}_{-0.06}$	$1.55^{+0.01}_{-0.01}$	$0.42^{+0.01}_{-0.01}$	$2.00^{+0.57}_{-2}$	$0.88^{+0.26}_{-0.88}$	$1.07^{+0.28}_{-0.28}$	$0.19^{+0.04}_{-0.19}$	$0.63^{+0.15}_{-0.63}$
Abell 2261	0.067	0.138	0.285	0.588	1.210	$28.22^{+0.4}_{-0.41}$	$11.92^{+0.12}_{-0.12}$	$4.04^{+0.04}_{-0.04}$	$1.28^{+0.01}_{-0.01}$	$0.35^{+0.01}_{-0.01}$	$0.41^{+0.1}_{-0.41}$	$0.42^{+0.14}_{-0.14}$	$0.32^{+0.07}_{-0.07}$	$0.12^{+0.03}_{-0.12}$	$0.17^{+0.04}_{-0.17}$
Abell 2219	0.0634	0.125	0.249	0.492	0.975	$18.52^{+0.68}_{-0.7}$	$13.77^{+0.34}_{-0.38}$	$6.98^{+0.07}_{-0.07}$	$2.51^{+0.04}_{-0.04}$	$0.72^{+0.02}_{-0.01}$	$1.13^{+0.28}_{-1.13}$	$0.89^{+0.33}_{-0.35}$	$0.95^{+0.11}_{-0.12}$	$0.71^{+0.17}_{-0.17}$	$0.66^{+0.27}_{-0.27}$
Abell 267	0.0904	0.162	0.292	0.524	0.942	$16.78^{+0.61}_{-0.63}$	$9.55^{+0.23}_{-0.23}$	$4.16^{+0.09}_{-0.09}$	$1.66^{+0.04}_{-0.04}$	$0.53^{+0.02}_{-0.02}$	$2.86^{+0.7}_{-2.86}$	$0.89^{+0.25}_{-0.89}$	$1.56^{+0.34}_{-0.34}$	$1.49^{+0.35}_{-0.34}$	$1.19^{+0.31}_{-1.19}$
RX J2129.6+005	0.0875	0.148	0.251	0.425	0.721	$29.19^{+0.65}_{-0.64}$	$12.45^{+0.37}_{-0.38}$	$5.76^{+0.14}_{-0.13}$	$2.45^{+0.06}_{-0.06}$	$0.78^{+0.04}_{-0.03}$	$0.76^{+0.21}_{-0.76}$	$1.07^{+0.29}_{-1.07}$	$0.78^{+0.17}_{-0.78}$	$1.17^{+0.2}_{-0.2}$	$1.19^{+0.44}_{-0.45}$
Abell 1835	0.0787	0.158	0.318	0.638	1.280	$42.27^{+0.95}_{-0.96}$	$13.72^{+0.21}_{-0.19}$	$4.83^{+0.04}_{-0.04}$	$1.36^{+0.02}_{-0.02}$	$0.33^{+0.01}_{-0.01}$	$1.18^{+0.36}_{-0.36}$	$0.61^{+0.24}_{-0.25}$	$0.92^{+0.09}_{-0.09}$	$1.25^{+0.16}_{-0.16}$	$1.63^{+0.34}_{-0.34}$
Abell 697	0.0776	0.156	0.314	0.631	1.270	$15.86^{+0.56}_{-0.55}$	$9.82^{+0.16}_{-0.16}$	$4.08^{+0.05}_{-0.05}$	$1.36^{+0.02}_{-0.02}$	$0.37^{+0.01}_{-0.01}$	$0.79^{+0.2}_{-0.79}$	$0.52^{+0.18}_{-0.18}$	$0.85^{+0.06}_{-0.06}$	$0.35^{+0.09}_{-0.1}$	$0.26^{+0.06}_{-0.26}$
Abell 611	0.105	0.200	0.379	0.718	1.360	$19.78^{+0.48}_{-0.47}$	$7.91^{+0.16}_{-0.15}$	$3.16^{+0.05}_{-0.05}$	$1.00^{+0.03}_{-0.02}$	$0.35^{+0.01}_{-0.01}$	$1.37^{+0.39}_{-1.37}$	$0.94^{+0.28}_{-0.94}$	$1.34^{+0.25}_{-0.25}$	$0.51^{+0.11}_{-0.51}$	$0.32^{+0.07}_{-0.32}$
MS 2137.3−2353	0.129	0.245	0.465	0.882	1.670	$14.24^{+0.46}_{-0.4}$	$4.01^{+0.13}_{-0.13}$	$1.30^{+0.04}_{-0.04}$	$0.58^{+0.02}_{-0.02}$	$0.36^{+0.01}_{-0.01}$	$1.95^{+0.63}_{-1.95}$	$2.02^{+0.57}_{-2.02}$	$1.31^{+0.32}_{-1.31}$	$1.71^{+0.6}_{-0.61}$	$0.48^{+0.1}_{-0.48}$
MACS J1931.8−2634	0.111	0.190	0.326	0.559	0.959	$27.78^{+0.83}_{-0.65}$	$9.62^{+0.21}_{-0.19}$	$4.08^{+0.07}_{-0.07}$	$1.39^{+0.02}_{-0.02}$	$0.48^{+0.01}_{-0.01}$	$0.54^{+0.15}_{-0.54}$	$0.99^{+0.25}_{-0.99}$	$1.03^{+0.41}_{-0.42}$	$1.93^{+0.25}_{-0.25}$	$1.85^{+0.54}_{-0.54}$
Abell S1063	0.084	0.173	0.355	0.727	1.490	$28.93^{+0.41}_{-0.38}$	$12.32^{+0.19}_{-0.2}$	$4.17^{+0.04}_{-0.04}$	$0.99^{+0.01}_{-0.01}$	$0.26^{+0.01}_{-0.01}$	$1.49^{+0.48}_{-0.48}$	$0.53^{+0.24}_{-0.25}$	$1.12^{+0.12}_{-0.12}$	$1.62^{+0.3}_{-0.3}$	$2.26^{+0.62}_{-0.64}$
MACS J1115.8+0129	0.118	0.217	0.401	0.738	1.360	$23.51^{+0.4}_{-0.37}$	$8.33^{+0.17}_{-0.15}$	$3.11^{+0.05}_{-0.05}$	$1.01^{+0.02}_{-0.02}$	$0.32^{+0.01}_{-0.01}$	$0.85^{+0.23}_{-0.85}$	$0.60^{+0.17}_{-0.6}$	$1.51^{+0.22}_{-0.22}$	$1.80^{+0.33}_{-0.33}$	$2.27^{+0.6}_{-0.6}$
Abell 370	0.112	0.198	0.353	0.628	1.120	$7.55^{+0.67}_{-0.66}$	$5.55^{+0.31}_{-0.32}$	$2.68^{+0.12}_{-0.12}$	$1.25^{+0.05}_{-0.05}$	$0.32^{+0.03}_{-0.03}$	$1.92^{+0.56}_{-1.92}$	$1.58^{+0.4}_{-1.58}$	$1.17^{+0.32}_{-0.32}$	$1.56^{+0.22}_{-0.22}$	$2.45^{+0.64}_{-0.64}$
ZWCL 0024+17	0.159	0.292	0.539	0.993	1.830	$7.38^{+0.24}_{-0.23}$	$3.26^{+0.11}_{-0.1}$	$1.25^{+0.05}_{-0.05}$	$0.57^{+0.03}_{-0.02}$	$0.35^{+0.01}_{-0.01}$	$1.69^{+0.45}_{-1.69}$	$1.57^{+0.41}_{-1.57}$	$1.52^{+0.36}_{-1.52}$	$2.47^{+1.01}_{-1.04}$	$2.03^{+0.44}_{-2.03}$
MACS J1532.9+3021	0.115	0.222	0.428	0.825	1.590	$31.84^{+0.35}_{-0.35}$	$8.51^{+0.15}_{-0.15}$	$2.60^{+0.06}_{-0.06}$	$0.77^{+0.03}_{-0.03}$	$0.21^{+0.02}_{-0.02}$	$0.33^{+0.08}_{-0.33}$	$0.65^{+0.24}_{-0.26}$	$0.71^{+0.17}_{-0.17}$	$0.46^{+0.2}_{-0.2}$	$0.41^{+0.09}_{-0.41}$
MACS J0429.6−0253	0.147	0.244	0.407	0.677	1.130	$16.67^{+0.37}_{-0.37}$	$6.24^{+0.22}_{-0.22}$	$2.58^{+0.1}_{-0.12}$	$1.14^{+0.04}_{-0.04}$	$0.34^{+0.01}_{-0.01}$	$1.10^{+0.23}_{-1.1}$	$1.4\text{-}^{+0.45}_{-1.4}$	$1.46^{+0.39}_{-1.46}$	$2.08^{+0.35}_{-0.37}$	$3.82^{+0.67}_{-0.72}$
MACS J2211.7−0349	0.100	0.189	0.358	0.678	1.280	$26.99^{+0.57}_{-0.64}$	$10.08^{+0.23}_{-0.21}$	$3.55^{+0.07}_{-0.07}$	$1.16^{+0.03}_{-0.03}$	$0.25^{+0.01}_{-0.01}$	$1.23^{+0.44}_{-0.46}$	$0.52^{+0.13}_{-0.52}$	$1.11^{+0.17}_{-0.17}$	$1.01^{+0.24}_{-0.23}$	$1.03^{+0.24}_{-1.03}$
MACS J1720.3+3536	0.139	0.235	0.396	0.667	1.130	$15.73^{+0.42}_{-0.42}$	$6.30^{+0.18}_{-0.17}$	$2.87^{+0.06}_{-0.06}$	$1.08^{+0.03}_{-0.03}$	$0.30^{+0.02}_{-0.02}$	$1.79^{+0.45}_{-1.79}$	$1.19^{+0.35}_{-1.19}$	$0.67^{+0.18}_{-0.67}$	$1.08^{+0.29}_{-0.29}$	$1.17^{+0.29}_{-1.17}$
MACS J0416.1−2403	0.131	0.213	0.347	0.565	0.921	$8.38^{+0.46}_{-0.47}$	$5.35^{+0.27}_{-0.28}$	$3.89^{+0.13}_{-0.13}$	$1.70^{+0.05}_{-0.04}$	$0.38^{+0.04}_{-0.03}$	$1.36^{+0.39}_{-1.36}$	$1.09^{+0.29}_{-1.09}$	$1.08^{+0.46}_{-0.47}$	$0.96^{+0.26}_{-0.26}$	$2.53^{+0.61}_{-0.62}$
MACS J0451.9+0006	0.150	0.242	0.390	0.629	1.010	$10.74^{+0.51}_{-0.53}$	$5.40^{+0.36}_{-0.34}$	$2.73^{+0.17}_{-0.15}$	$1.39^{+0.07}_{-0.08}$	$0.51^{+0.03}_{-0.03}$	$1.14^{+0.32}_{-1.14}$	$0.96^{+0.27}_{-0.96}$	$1.06^{+0.27}_{-1.06}$	$1.04^{+0.33}_{-0.34}$	$1.23^{+0.41}_{-0.41}$
MACS J0417.5−1154	0.101	0.208	0.427	0.878	1.810	$18.41^{+0.39}_{-0.39}$	$6.63^{+0.09}_{-0.09}$	$2.98^{+0.02}_{-0.02}$	$0.85^{+0.01}_{-0.01}$	$0.22^{+0.01}_{-0.01}$	$0.75^{+0.27}_{-0.28}$	$0.38^{+0.17}_{-0.17}$	$0.78^{+0.05}_{-0.05}$	$0.64^{+0.08}_{-0.08}$	$0.23^{+0.05}_{-0.23}$
MACS J1206.2−0847	0.106	0.189	0.339	0.606	1.080	$18.81^{+0.46}_{-0.48}$	$7.98^{+0.20}_{-0.20}$	$3.61^{+0.06}_{-0.06}$	$1.30^{+0.03}_{-0.03}$	$0.35^{+0.01}_{-0.01}$	$0.96^{+0.22}_{-0.96}$	$0.53^{+0.15}_{-0.53}$	$0.92^{+0.12}_{-0.12}$	$1.17^{+0.12}_{-0.12}$	$1.45^{+0.29}_{-0.29}$
MACS J0329.6−0211	0.145	0.241	0.400	0.664	1.100	$14.15^{+0.41}_{-0.39}$	$5.98^{+0.21}_{-0.21}$	$2.62^{+0.08}_{-0.08}$	$1.07^{+0.05}_{-0.04}$	$0.35^{+0.02}_{-0.02}$	$0.93^{+0.27}_{-0.93}$	$1.00^{+0.28}_{-1}$	$1.52^{+0.43}_{-0.44}$	$1.41^{+0.26}_{-0.26}$	$2.18^{+0.45}_{-0.45}$
MACS J1347.5−1144	0.104	0.186	0.335	0.603	1.080	$32.63^{+0.39}_{-0.43}$	$9.67^{+0.17}_{-0.15}$	$3.71^{+0.04}_{-0.04}$	$1.25^{+0.02}_{-0.02}$	$0.29^{+0.01}_{-0.01}$	$1.08^{+0.22}_{-0.22}$	$0.47^{+0.11}_{-0.47}$	$0.94^{+0.1}_{-0.1}$	$0.76^{+0.09}_{-0.09}$	$0.75^{+0.23}_{-0.23}$
MACS J1311.0−0310	0.195	0.293	0.440	0.662	0.995	$12.65^{+0.21}_{-0.21}$	$4.42^{+0.14}_{-0.14}$	$2.38^{+0.08}_{-0.08}$	$0.97^{+0.04}_{-0.04}$	$0.31^{+0.04}_{-0.04}$	$1.03^{+0.28}_{-1.03}$	$1.30^{+0.33}_{-1.3}$	$1.35^{+0.37}_{-1.35}$	$1.56^{+0.44}_{-1.56}$	$4.03^{+0.57}_{-0.45}$
MACS J0257.1−2325	0.153	0.26	0.444	0.758	1.290	$13.82^{+0.34}_{-0.34}$	$5.52^{+0.20}_{-0.19}$	$2.44^{+0.07}_{-0.07}$	$0.95^{+0.04}_{-0.04}$	$0.40^{+0.03}_{-0.03}$	$2.41^{+0.88}_{-0.89}$	$0.75^{+0.18}_{-0.75}$	$0.56^{+0.13}_{-0.56}$	$2.36^{+0.31}_{-0.31}$	$1.35^{+0.52}_{-0.53}$
MACS J0911.2+1746	0.150	0.256	0.438	0.749	1.280	$7.71^{+0.34}_{-0.34}$	$4.19^{+0.19}_{-0.19}$	$1.90^{+0.09}_{-0.09}$	$0.84^{+0.04}_{-0.04}$	$0.44^{+0.03}_{-0.03}$	$1.03^{+0.27}_{-1.03}$	$0.66^{+0.18}_{-0.66}$	$0.55^{+0.14}_{-0.55}$	$0.87^{+0.28}_{-0.28}$	$0.49^{+0.12}_{-0.49}$
MACS J2214.9−1359	0.132	0.232	0.407	0.716	1.260	$12.19^{+0.4}_{-0.39}$	$5.22^{+0.20}_{-0.18}$	$2.47^{+0.06}_{-0.07}$	$1.01^{+0.03}_{-0.03}$	$0.3^{+0.02}_{-0.02}$	$0.80^{+0.24}_{-0.8}$	$0.92^{+0.25}_{-0.92}$	$1.34^{+0.24}_{-0.25}$	$1.52^{+0.16}_{-0.16}$	$2.18^{+0.39}_{-0.39}$
MACS J0018.5+1626	0.130	0.230	0.410	0.728	1.290	$10.46^{+0.29}_{-0.28}$	$6.50^{+0.27}_{-0.18}$	$2.76^{+0.04}_{-0.04}$	$0.99^{+0.02}_{-0.02}$	$0.31^{+0.01}_{-0.01}$	$0.59^{+0.18}_{-0.59}$	$0.41^{+0.14}_{-0.41}$	$0.81^{+0.11}_{-0.12}$	$0.83^{+0.11}_{-0.11}$	$0.92^{+0.22}_{-0.22}$
MACS J1149.5+2223	0.125	0.218	0.382	0.668	1.170	$7.97^{+0.39}_{-0.39}$	$4.91^{+0.20}_{-0.20}$	$2.92^{+0.06}_{-0.06}$	$1.10^{+0.03}_{-0.03}$	$0.39^{+0.02}_{-0.02}$	$0.86^{+0.24}_{-0.86}$	$0.58^{+0.17}_{-0.58}$	$0.67^{+0.12}_{-0.12}$	$1.08^{+0.1}_{-0.1}$	$1.07^{+0.2}_{-0.2}$
MACS J0717.5+3745	0.114	0.202	0.359	0.637	1.130	$9.37^{+0.27}_{-0.28}$	$6.09^{+0.16}_{-0.17}$	$3.78^{+0.04}_{-0.04}$	$1.47^{+0.03}_{-0.03}$	$0.36^{+0.01}_{-0.01}$	$1.07^{+0.29}_{-1.07}$	$0.66^{+0.18}_{-0.66}$	$0.91^{+0.09}_{-0.09}$	$0.20^{+0.05}_{-0.05}$	$0.06^{+0.01}_{-0.06}$

Table B3 – *continued*

Cluster	r_1	r_2	r_3	r_4	r_5	$n_{e,1}$	$n_{e,2}$	$n_{e,3}$	$n_{e,4}$	$n_{e,5}$	$T_{e,1}$	$T_{e,2}$	$T_{e,3}$	$T_{e,4}$	$T_{e,5}$
MACS J1423.8+2404	0.176	0.315	0.563	1.010	1.80	$13.19^{+0.6}_{-0.34}$	$3.93^{+0.06}_{-0.07}$	$1.54^{+0.03}_{-0.03}$	$0.55^{+0.01}_{-0.02}$	$0.25^{+0.01}_{-0.01}$	$0.7^{+0.19}_{-0.7}$	$1.21^{+0.52}_{-0.55}$	$0.97^{+0.35}_{-0.36}$	$1.14^{+0.32}_{-0.32}$	$0.73^{+0.19}_{-0.73}$
MACS J0454.1−0300	0.147	0.258	0.452	0.794	1.390	$14.42^{+0.25}_{-0.26}$	$7.15^{+0.31}_{-0.32}$	$2.94^{+0.04}_{-0.04}$	$0.93^{+0.02}_{-0.02}$	$0.45^{+0.01}_{-0.01}$	$1.27^{+0.32}_{-0.34}$	$0.34^{+0.08}_{-0.34}$	$0.9^{+0.12}_{-0.12}$	$1.21^{+0.11}_{-0.11}$	$0.86^{+0.17}_{-0.17}$
MACS J0025.4−1222	0.176	0.267	0.405	0.614	0.931	$6.96^{+0.23}_{-0.23}$	$4.61^{+0.17}_{-0.17}$	$2.81^{+0.12}_{-0.1}$	$1.31^{+0.03}_{-0.03}$	$0.46^{+0.03}_{-0.03}$	$1.22^{+0.35}_{-1.22}$	$0.97^{+0.28}_{-0.97}$	$0.61^{+0.16}_{-0.61}$	$0.9^{+0.31}_{-0.32}$	$0.77^{+0.17}_{-0.77}$
MS 2053.7−0449	0.241	0.332	0.457	0.63	0.867	$4.82^{+0.29}_{-0.27}$	$2.55^{+0.25}_{-0.25}$	$1.58^{+0.13}_{-0.12}$	$1.14^{+0.05}_{-0.06}$	$0.42^{+0.06}_{-0.07}$	$1.22^{+0.31}_{-1.22}$	$1.38^{+0.33}_{-1.38}$	$1.30^{+0.27}_{-1.3}$	$0.74^{+0.17}_{-0.74}$	$0.96^{+0.18}_{-0.96}$
MACS J0647.7+7015	0.158	0.271	0.466	0.801	1.380	$11.49^{+0.56}_{-0.49}$	$5.20^{+0.16}_{-0.17}$	$2.02^{+0.07}_{-0.07}$	$0.73^{+0.03}_{-0.03}$	$0.29^{+0.02}_{-0.02}$	$0.57^{+0.14}_{-0.57}$	$1.24^{+0.47}_{-0.5}$	$1.09^{+0.3}_{-0.3}$	$1.71^{+0.18}_{-0.18}$	$1.49^{+0.32}_{-0.32}$
MACS J2129.4−0741	0.159	0.268	0.452	0.761	1.280	$11.13^{+0.39}_{-0.39}$	$4.71^{+0.18}_{-0.19}$	$1.97^{+0.07}_{-0.07}$	$0.9^{+0.03}_{-0.03}$	$0.26^{+0.02}_{-0.02}$	$1.1^{+0.33}_{-1.1}$	$1.22^{+0.37}_{-1.22}$	$0.82^{+0.32}_{-0.32}$	$1.28^{+0.15}_{-0.15}$	$1.59^{+0.34}_{-0.34}$
MACS J0744.8+3927	0.169	0.264	0.413	0.645	1.010	$10.85^{+0.64}_{-0.49}$	$4.20^{+0.14}_{-0.15}$	$2.37^{+0.15}_{-0.12}$	$1.03^{+0.04}_{-0.04}$	$0.46^{+0.02}_{-0.02}$	$0.37^{+0.08}_{-0.37}$	$1.12^{+0.31}_{-1.12}$	$0.59^{+0.21}_{-0.59}$	$0.56^{+0.22}_{-0.23}$	$0.11^{+0.03}_{-0.11}$
MS 1054.4−0321	0.213	0.305	0.436	0.624	0.893	$4.63^{+0.17}_{-0.21}$	$4.60^{+0.37}_{-0.33}$	$3.50^{+0.14}_{-0.13}$	$1.43^{+0.07}_{-0.06}$	$0.73^{+0.02}_{-0.02}$	$0.99^{+0.25}_{-0.99}$	$0.41^{+0.08}_{-0.41}$	$0.46^{+0.2}_{-0.17}$	$0.57^{+0.13}_{-0.57}$	$0.96^{+0.16}_{-0.16}$
CL J0152.7−1357	0.235	0.346	0.508	0.747	1.100	$2.33^{+0.33}_{-0.33}$	$2.65^{+0.25}_{-0.2}$	$1.20^{+0.07}_{-0.07}$	$1.26^{+0.14}_{-0.09}$	$0.52^{+0.03}_{-0.02}$	$0.84^{+0.21}_{-0.84}$	$0.39^{+0.06}_{-0.39}$	$0.79^{+0.14}_{-0.79}$	$0.66^{+0.19}_{-0.66}$	$1.03^{+0.31}_{-0.31}$
CL J1226.9+3332	0.233	0.331	0.470	0.667	0.947	$7.79^{+0.73}_{-0.55}$	$3.15^{+0.18}_{-0.18}$	$2.13^{+0.16}_{-0.16}$	$0.91^{+0.11}_{-0.09}$	$0.38^{+0.08}_{-0.07}$	$0.48^{+0.12}_{-0.48}$	$1.14^{+0.3}_{-1.14}$	$1.04^{+0.28}_{-1.04}$	$1.33^{+0.36}_{-1.33}$	$0.66^{+0.15}_{-0.66}$

Note. All of the parameter values in this table have been scaled relative to the self-similar values r_{500}, $n_{e,500}$, and T_{500} (see equations (11) and (12)). The value of r_i corresponds to the centre of the shell (see Fig. 3).

Individual cluster profiles (Figs B1–B45), shown in order of increasing redshift. From top to bottom, the three plots for each cluster show the density, temperature, and pressure profiles. The results from this work are shown as black crosshairs for the concentric shell deprojections and as blue lines for the smooth parametric profiles +/- 1σ. Also included as green points are deprojected profiles from the ACCEPT X-ray-only study (Cavagnolo et al. 2009). In each plot, a vertical line denotes r_{500}. Where available, the joint X-ray/SZ fits from LaRoque et al. (2006) are plotted in magenta.

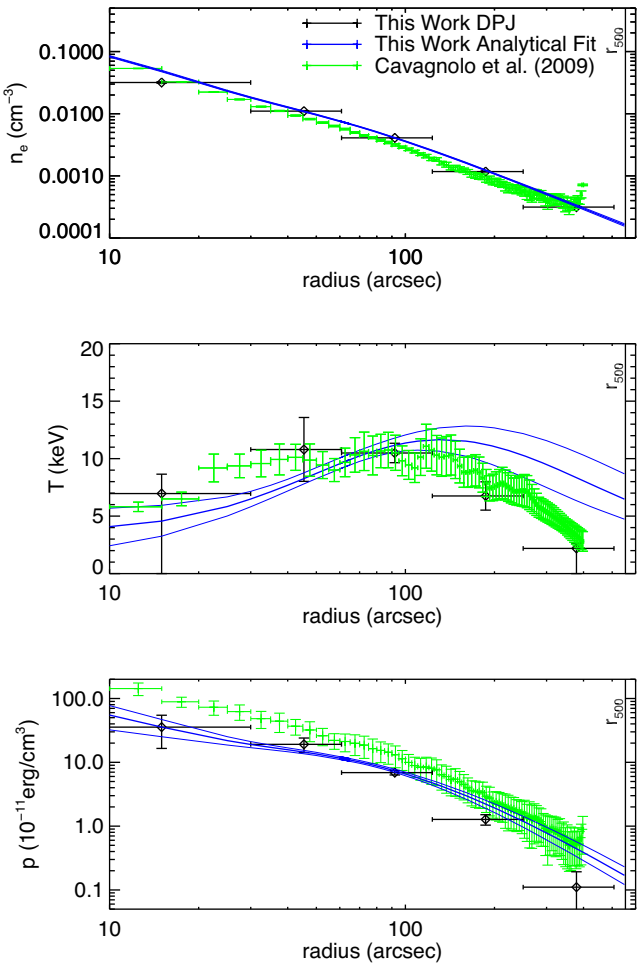

Figure B1. *Abell 2204.* Our smooth parametric profile fit detects a cool core at a significance of 3.8σ, and the temperature drop in the outskirts is detected at a significance 5σ. Although we classify this cluster as relaxed, Sanders, Fabian & Taylor (2005), using X-ray data, found a complicated core consisting of several cold fronts that may be attributed to the cluster recovering from a merger. Gu et al. (2009) also found such temperature substructures, and speculate that they may be caused by an AGN. Sanders, Fabian & Taylor (2009), again using X-ray data, found dips in the surface brightness that may be caused by radio bubble formation in the core of the cluster. Reiprich et al. (2009) used *Suzaku* X-ray measurements to probe the cluster out to large radii, approximately 12 arcmin, where the temperature was found to be 4 keV. This is in good agreement with both the extrapolation of our smooth parametric profile and the predictions from the hydrodynamical simulations of Roncarelli et al. (2006).

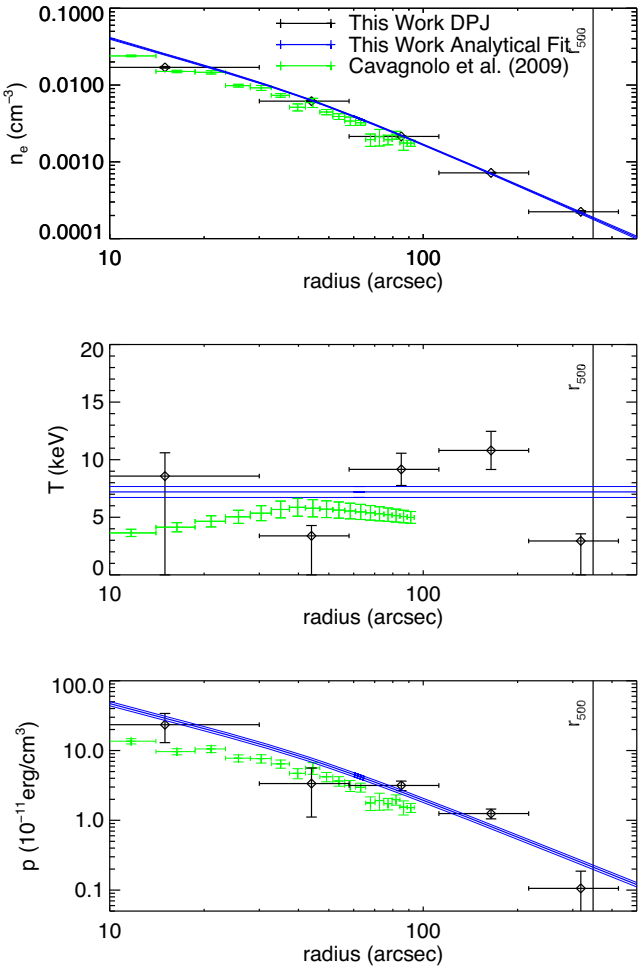

Figure B2. *Abell 383.* Our isothermal smooth parametric fit to the temperature is somewhat higher than that of the ACCEPT study. This cluster is thought to be prolate and elongated along the line of sight (Newman et al. 2013), and a triaxial geometry is required to reconcile masses determined from X-rays and lensing (Morandi & Limousin 2012).

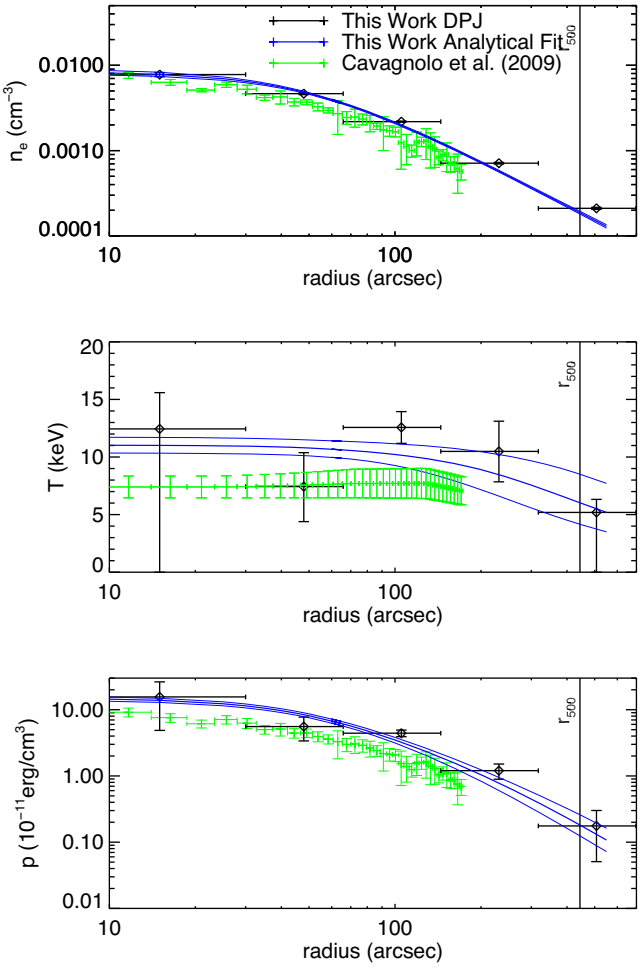

Figure B3. *Abell 209.* In our smooth parametric fit, we detect a temperature drop in the outskirts at a significance of 3.5σ. Although our temperature is somewhat higher than the ACCEPT results, we note that Mercurio et al. (2003) found a temperature of $10.2^{+1.4}_{-1.2}$ keV using X-ray spectroscopy within 180 arcsec, in good agreement with our results. We classify this cluster as non-disturbed, but Mercurio et al. (2003) found a slightly elongated structure in the X-ray map arising from two X-ray peaks. Adding to the evidence that this cluster is at least somewhat disturbed, Paulin-Henriksson et al. (2007) also found elongation in the mass distribution through weak lensing.

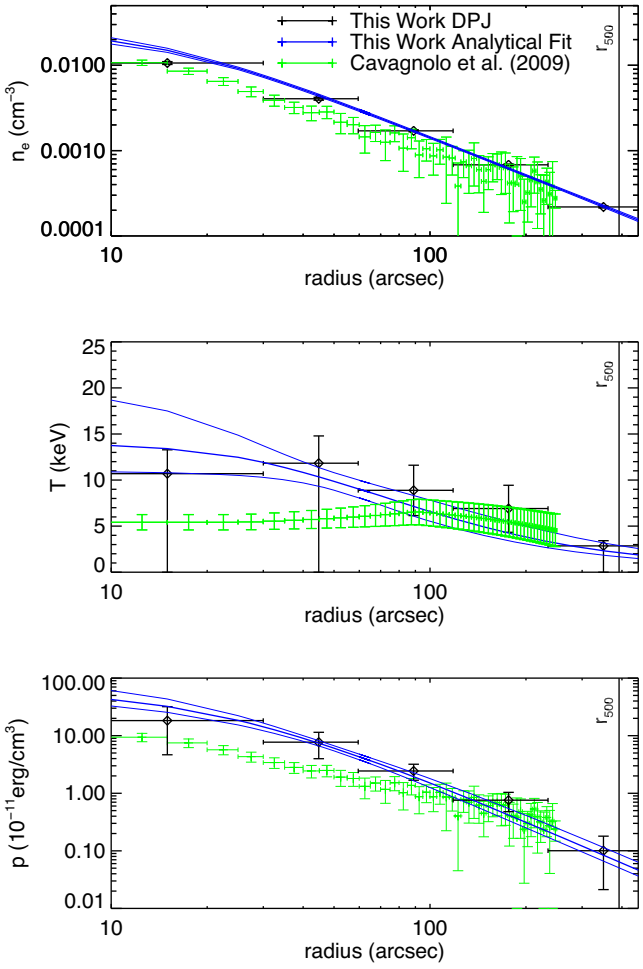

Figure B4. *Abell 1423.* We detect a decrease in the temperature profile at large radii at a significance of 6.9σ. AMI Consortium (2012), using SZ data rather than X-ray spectroscopic measurements, fitted an isothermal model with a temperature of 3.0 $\pm$ 0.8 keV, somewhat low compared to our measurements. However, the X-ray spectroscopic measurements from ACCEPT indicate a higher temperature (5.2 keV).

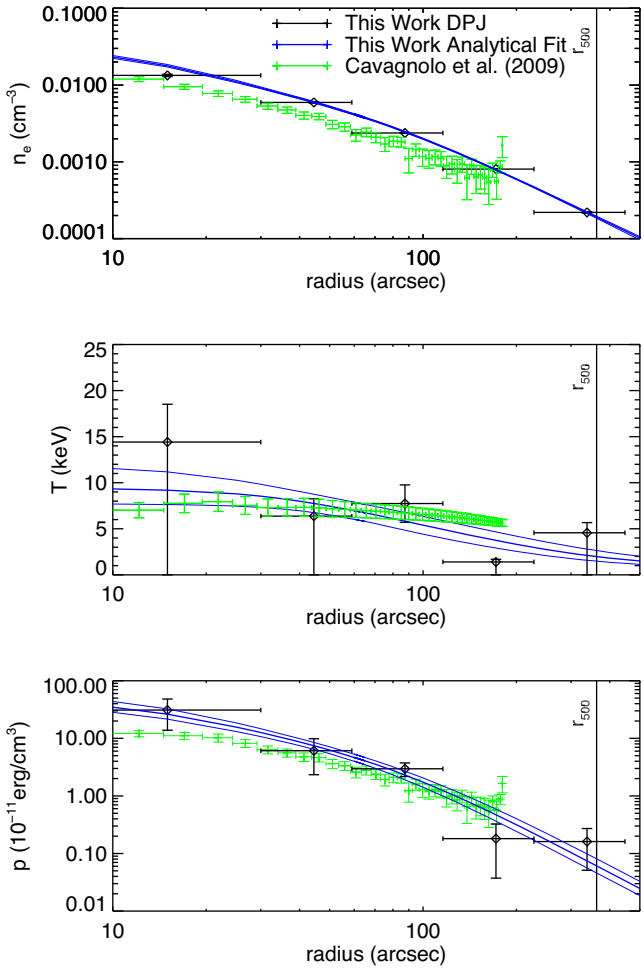

Figure B5. *Abell 963.* We detect a decrease in the temperature profile at large radii at a significance of 6σ. Our density profile is somewhat higher than that of the ACCEPT study. We do not detect the presence of a cool core, but others have found a slight temperature decrease in the centre (Baldi et al. 2007; Cavagnolo et al. 2009). Leccardi & Molendi (2008), using *XMM–Newton*, specifically made note of this and identified it as an 'intermediate' cluster since the temperature decrease in the centre is modest.

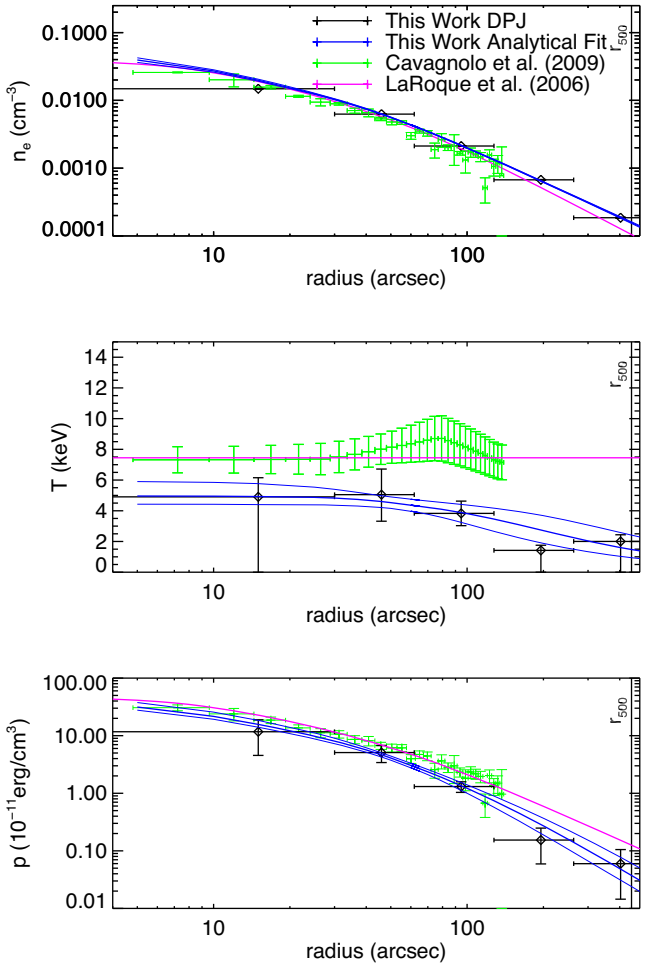

Figure B6. *Abell 2261.* Based on our smooth parametric fit, we detect a temperature drop in the outskirts at a significance of 5.5σ. Compared to X-ray spectroscopy, ACCEPT (Cavagnolo et al. 2009) shows a slight temperature drop in the centre, which is not detected in our analysis, along with an overall temperature somewhat higher than our results. Baldi et al. (2007) found a slight cool core, with a central temperature of 7.7 ± 0.4 keV and peak of 9.0 ± 0.4 keV. Bonamente et al. (2006), also using X-ray spectroscopy, similarly found a temperature profile in good agreement with the ACCEPT results. Coe et al. (2012) found a density profile slope that is shallower than the usual slope at small radii for cool-core clusters; thus they defined it as a 'borderline' relaxed and cool-core cluster (our analysis classifies it as a CC non-disturbed cluster). Finally, Abell 2261 is a CLASH cluster (Postman et al. 2012), and Coe et al. (2012) used the CLASH data to obtain a detailed mass measurement, deducing that the dark matter halo is elongated along the line of sight.

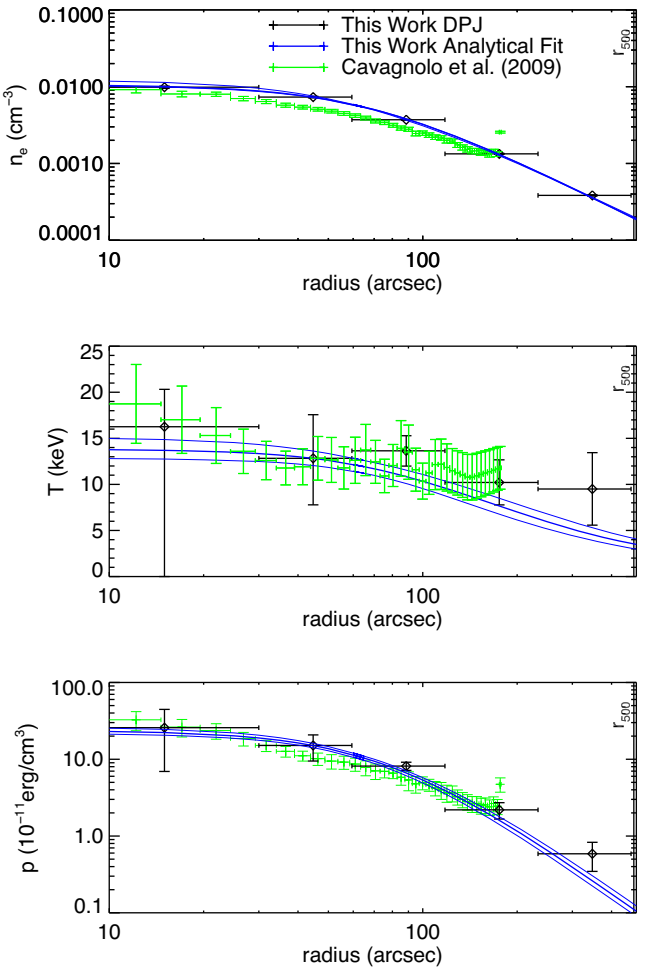

Figure B7. *Abell 2219.* Our smooth parametric fit shows a decrease in temperature in the outskirts at a significance of 11.8σ. Jiménez-Bailón, Lozada-Muñoz & Aguerri (2013) found a shock front with >16keV gas 2 arcmin NW of the cluster, and this elongated cluster is possibly undergoing a large merger event (Boschin et al. 2004). Further evidence for a major merger was detailed in Canning et al. (2017), who used *Chandra* data to identify numerous cold and shock fronts, along with a large temperature spike ∼25 arcsec from the core of the cluster.

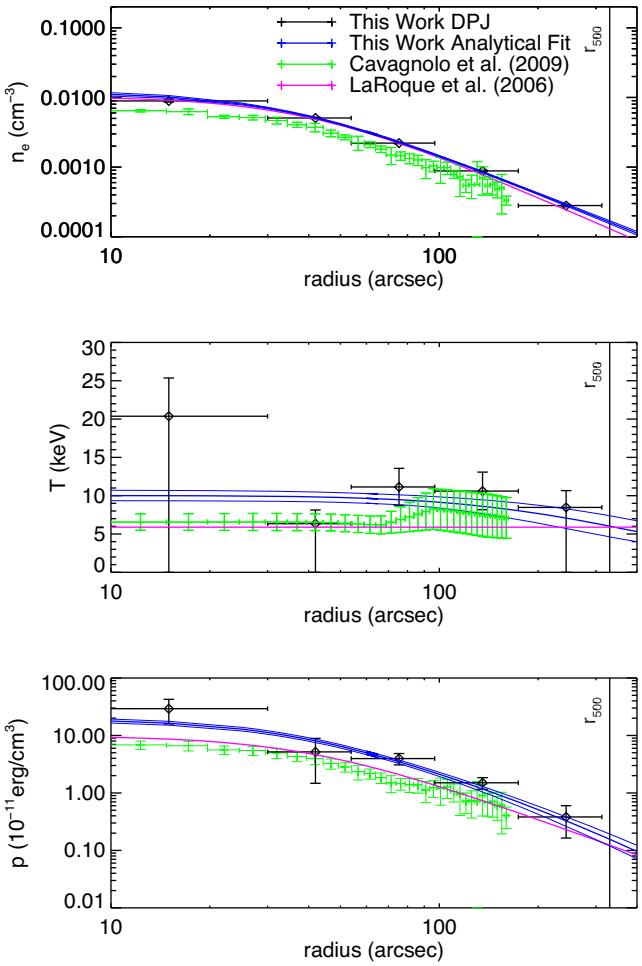

Figure B8. *Abell 267.* Our deprojections and smooth parametric fits show a mostly flat temperature profile. Our data indicate a somewhat higher temperature in the core region compared to ACCEPT. Our smooth parametric fit shows some evidence of a drop in temperature at large radii (2.8σ). Jiménez-Bailón et al. (2013) used *XMM–Newton* spectroscopy to deproject a temperature profile, and they also found an approximately flat profile with a temperature of ∼6 keV. They consider A267 a 'fossil' system, which is dominated by a massive elliptical galaxy. Fossil systems in general have not merged recently, and usually host a cool core. The lack of a cool core in this cluster is perhaps related to heating from an AGN.

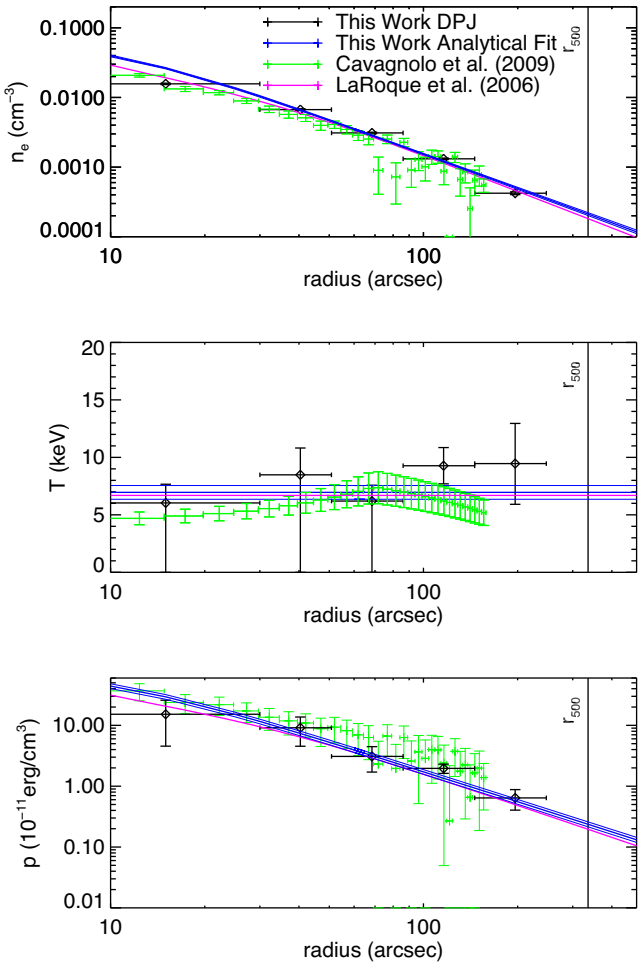

Figure B9. *RX J2129.6+005.* There is some deviation between our density deprojection and the smooth parametric fit near the centre, which may suggest that the single-beta profile is not fully sufficient in describing the data. This is one of the few clusters in the sample where the fits do not reach r_{500}, due to the poor quality of the X-ray data. Landry et al. (2013) used *Chandra* observations to identify this as a relaxed cluster based on the centroid shift. Furthermore, unlike the relatively isothermal temperature profile found in both our analysis and the ACCEPT analysis, they found a central temperature of 4 keV, a peak temperature of 8 keV near 90 arcsec and a decrease in temperature back to 4 keV at the outskirts (near 240 arcsec).

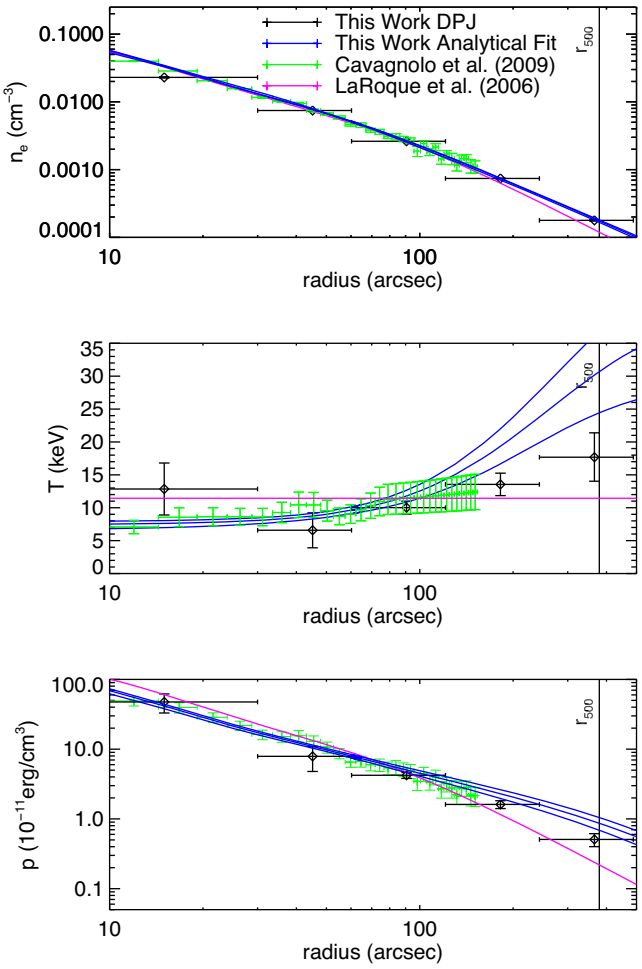

Figure B10. *Abell 1835.* Our smooth parametric fits show modest evidence for a temperature drop in the core (2.8σ). In the outer regions of the cluster, our temperature and pressure profiles are somewhat higher compared to those of the joint X-ray/SZ study presented in LaRoque et al. (2006), although this may be related to the isothermal assumption used in that analysis. In contrast to the rising temperature at large radii seen in our fits, Ichikawa et al. (2013) found that the temperature slowly decreases from 8 keV in the inner region to around 2 keV near the virial radius using *Suzaku* X-ray spectroscopy. Based on *Chandra* observations, Bonamente et al. (2013) also found a similarly large drop in temperature towards the cluster outskirts. We note that many studies have found this cluster to be spherically symmetric without any significant substructure (Korngut et al. 2011; Ichikawa et al. 2013), although Morandi et al. (2012) find that the cluster is elongated in the line of sight, which may be the cause of the apparent temperature increase at large radii in our fits. In addition, Baldi et al. (2007) found that the temperature drops by a factor of 2 in the core region relative to the peak, in contrast to both our results and the ACCEPT results.

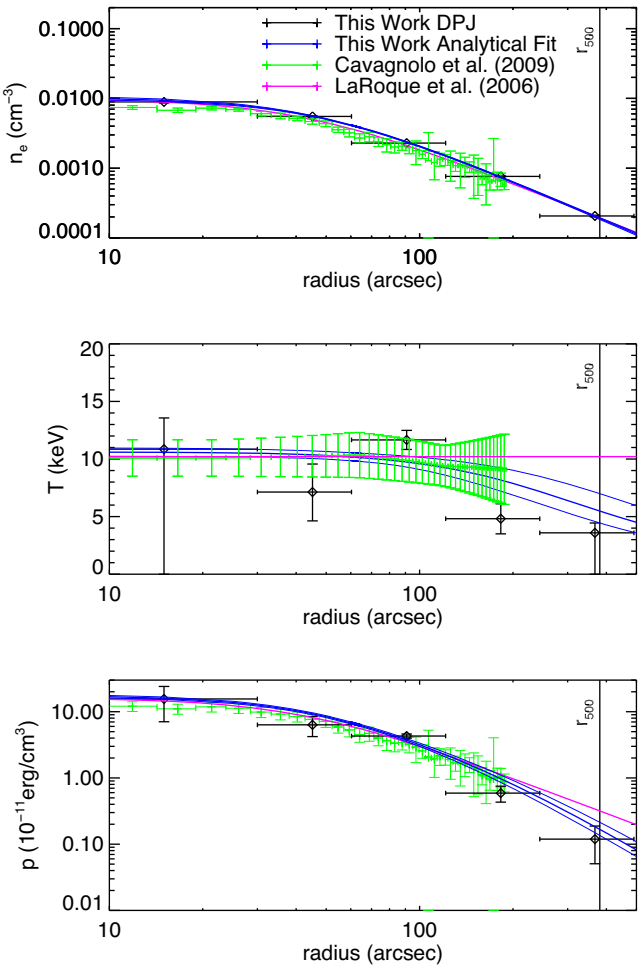

Figure B11. *Abell 697.* We find a relatively flat inner temperature profile, and we detect a drop in temperature near r_{500} at a significance of 4.5σ. Our pressure profiles are consistent with those of the joint X-ray/SZ study of LaRoque et al. (2006). Although we characterized the cluster as non-disturbed, several other studies have shown that the cluster has undergone recent merging. Girardi, Boschin & Barrena (2006) conducted a multiwavelength study using optical and X-ray data, where they calculated line-of-sight galaxy velocity dispersions and spectroscopic temperatures, respectively, and found that A697 is not relaxed. With elongated X-ray emission and substructures near the centre, Abell 697 likely went through many mergers. Through lensing, Metzger & Ma (2000) also concluded that the cluster has undergone a recent merger.

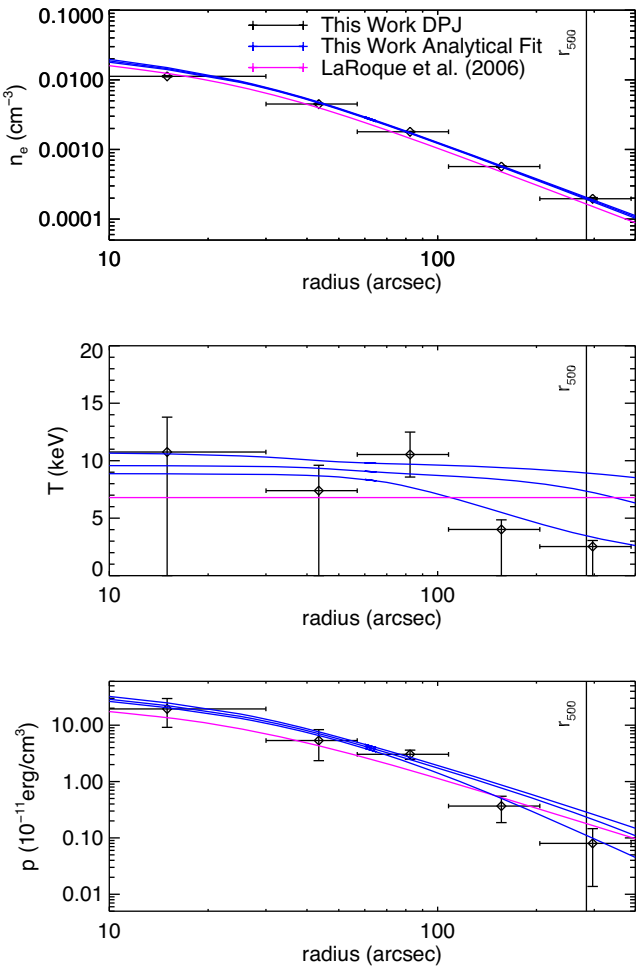

Figure B12. *Abell 611.* We find a relatively flat temperature profile, in good agreement with the spectroscopic X-ray measurements from Bonamente et al. (2006). In addition, Donnarumma et al. (2011) performed an analysis of this cluster using X-ray data from *Chandra* and lensing results from *Hubble*. Unlike our analysis, they identify it as a cool-core cluster. However, their overall temperature profile is in good agreement with our results. They found a central temperature of 6 keV, a peak of 8 keV at 100 kpc (20 arcsec), and a slow drop in temperature to 5keV at 600 kpc (150 arcsec). There is a known error in the ACCEPT results for this cluster, and so they are not included in the plot.

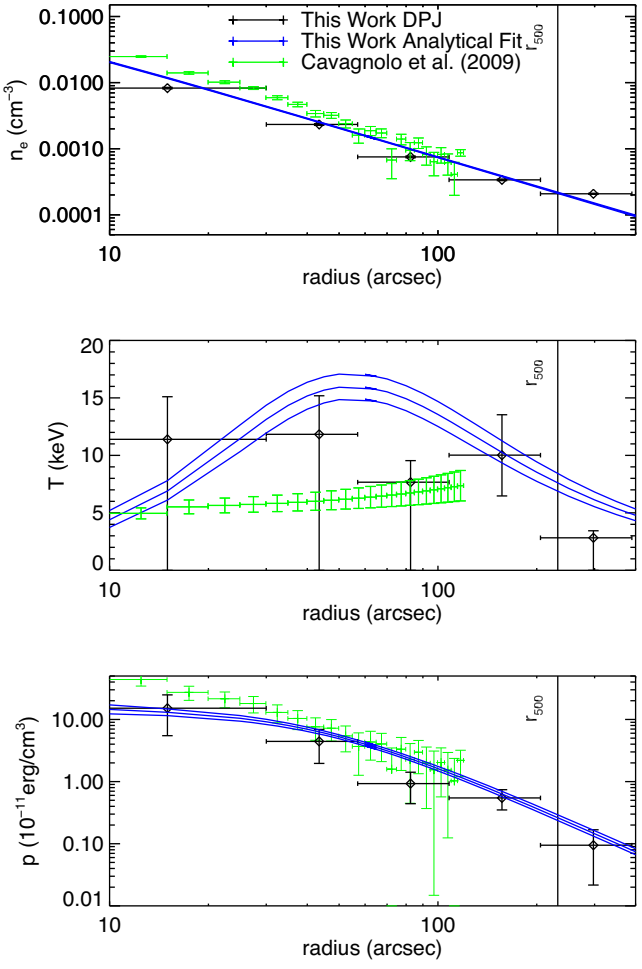

Figure B13. *MS 2137.3−2353.* In our smooth parametric fits, we detect a temperature drop in the centre at a significance of 5.3σ and a temperature drop in the outskirts at a significance of 11.3σ. Our smooth parametric fit indicates a significantly higher temperature at intermediate radii compared to ACCEPT. In reasonable agreement with the ACCEPT results, Donnarumma et al. (2009) obtained a spectroscopic temperature profile using *Chandra* with a 4 keV central temperature, a peak of 5.5 keV at 100 kpc (around 20 arcsec), and decreasing to 3.5 keV in the outskirts at 500 kpc (around 110 arcsec).

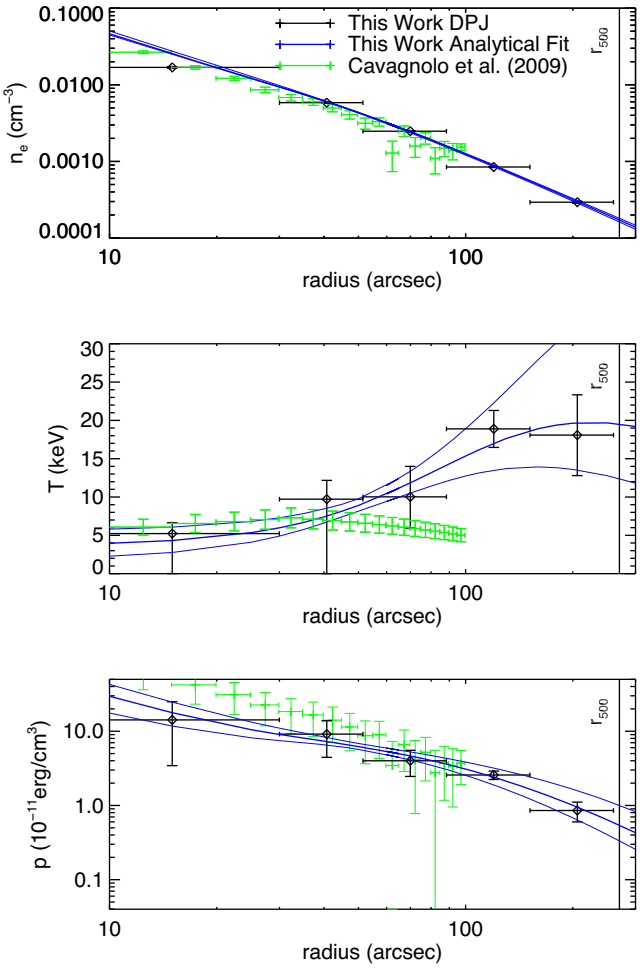

Figure B14. *MACS J1931.8−2634.* There is a slight increase in our derived temperatures towards large radii. Based on our smooth parametric fits, there is some evidence of a drop in temperature at the cluster centre ($\sim 2\sigma$). A detailed multiwavelength study of this cluster was performed by Ehlert et al. (2011) using X-ray (*Chandra*), optical (Subaru), and radio (Very Large Array) data. They found a cool core with AGN feedback (seen in the X-ray and in the radio), along with evidence of merging, suggesting a cool core that is currently being destroyed. They created a temperature map of the cluster from X-ray spectroscopy out to radii of 500 kpc (100 arcsec), and found an asymmetric temperature distribution. Their azimuthally averaged temperature profile has a central temperature of 5 keV and peak of 10 keV, roughly consistent with our results.

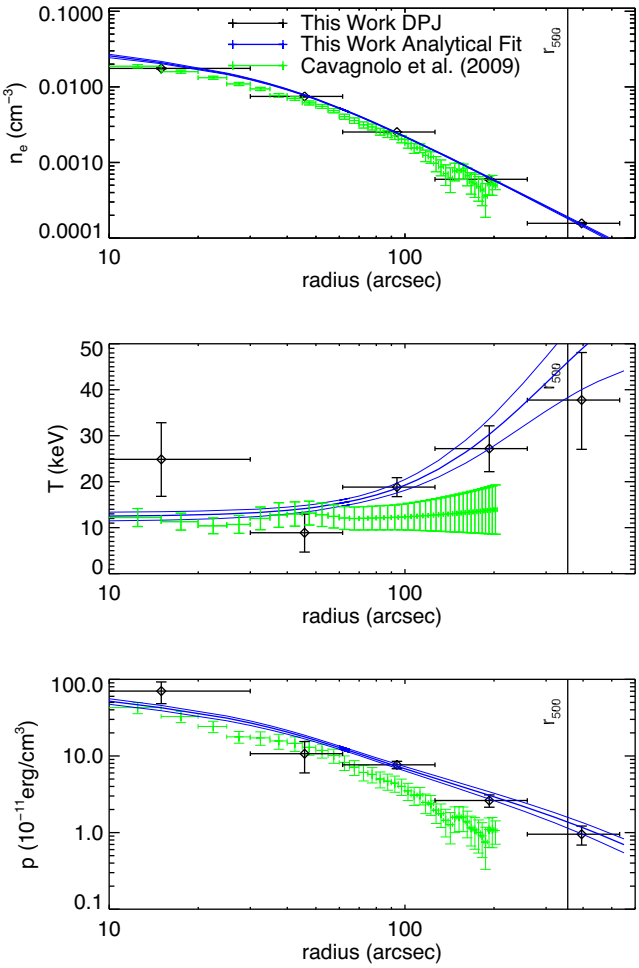

Figure B15. *Abell S1063.* There is a slight increase in temperature at large radii. Gómez et al. (2012) found evidence of merging through both X-ray and optical observations, with an elongated X-ray emission feature in the same direction as two regions of high galaxy density. They found high cluster temperatures of 12–17keV from the centre to ∼800 kpc (160 arcsec), in reasonable agreement with our results over the same range.

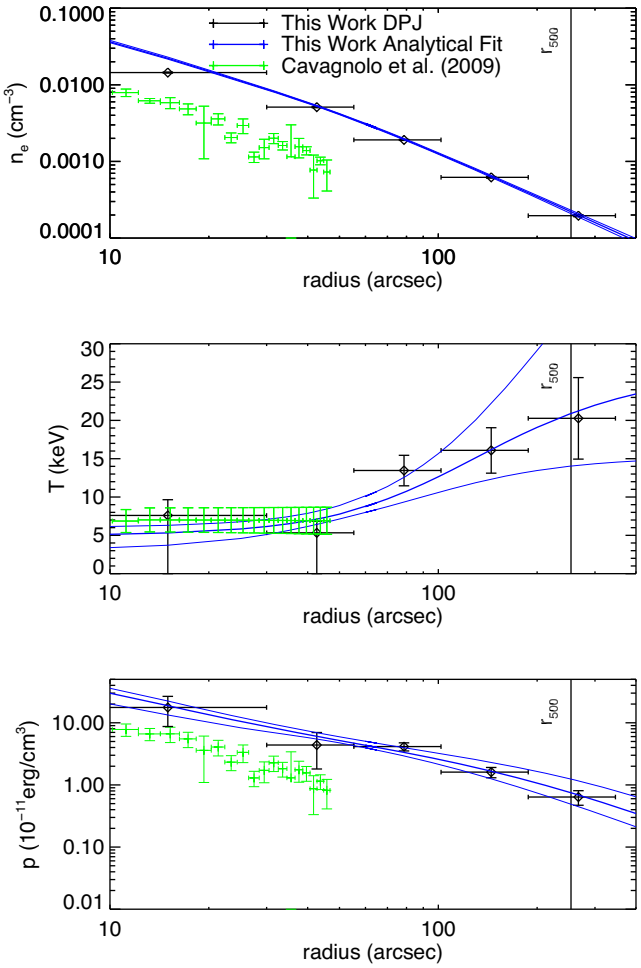

Figure B16. *MACS J1115.8+0129.* The ACCEPT analysis finds densities systematically lower than ours, but our results are consistent with other studies (e.g. Mantz et al. 2016). Donahue et al. (2014) found temperature profiles from X-ray spectroscopy (*XMM–Newton* and *Chandra*), showing a central temperature of around 3 keV rising to 8–9keV, roughly matching our results over the same region. However, the *XMM–Newton* data then show a decrease in the temperature profile near 800 kpc (160 arcsec), which is not seen in our results.

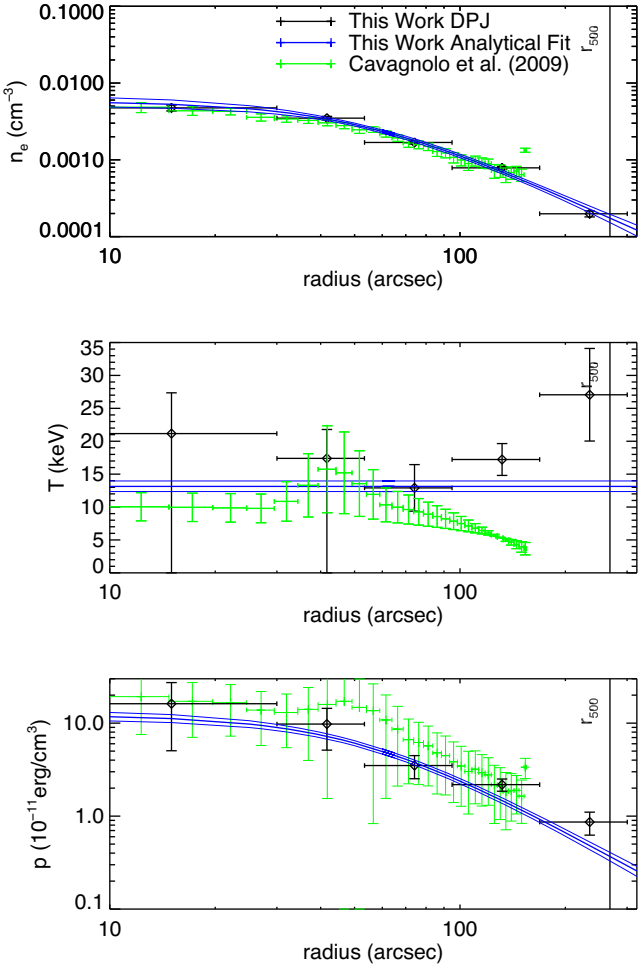

Figure B17. *Abell 370.* There is a temperature drop at large radii not present in the ACCEPT results. Several studies at different wavelengths have found that this cluster is not spherical. This is a very popular lensing cluster, and many such studies have been performed (Medezinski et al. 2010). De Filippis et al. (2005) combined X-ray and SZ data to find the 3D shapes of galaxy clusters, including Abell 370, and found a triaxial morphology, elongated along the line of sight. Richard et al. (2010) conducted a strong lensing analysis based on *Hubble*/ACS observations and reconstructed the mass distribution, which indicates an elongated, bimodal mass distribution aligned with the *Chandra* X-ray luminosity maps. The galaxy distribution also shows bimodality, suggesting a merging cluster. Grego et al. (2000), using OVRO SZ observations of this cluster, also found a smooth but non-spherical distribution.

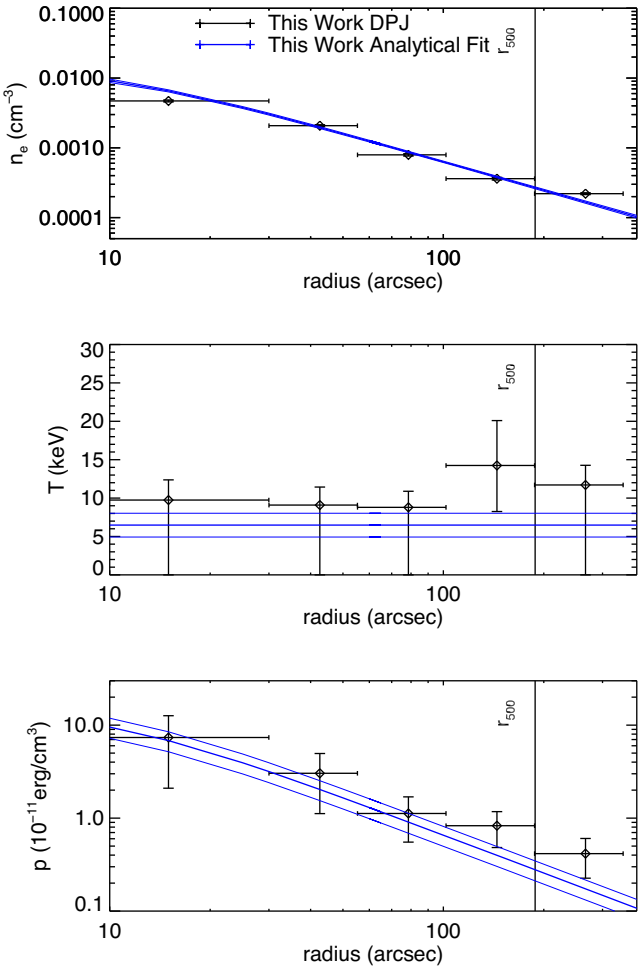

Figure B18. *ZWCL 0024+17*. Zhang et al. (2005) performed an *XMM–Newton* study using imaging and spectroscopy, and found a temperature decrease at large radii (80–180 arcsec) from the isothermal ∼4keV central region, which is fairly consistent with our results. They also found an elongation in the X-ray hard ratio map on large scales, and substructure at large radii. Ota et al. (2004) used *Chandra* spectroscopy and found a nearly isothermal profile of ∼4.5 keV out to 600 kpc (110 arcsec), again quite similar to our results. Böhringer et al. (2000) used *ROSAT* to look at the cluster's X-ray morphology, and found a very small core radius in the surface brightness. They also found an elongation in the X-ray emission; however, it is consistent with a spherical model. Tyson, Kochanski & Dell'Antonio (1998) obtained a mass map using strong lensing measurements, and found a relaxed distribution. Umetsu et al. (2010) performed a full-lensing analysis, including Subaru and *Hubble*/ACS/NIC3 observations, and looked at X-ray data along with simulations. They suggest that the cluster is in a post-collisional state, with two clusters at the same line of sight, as well as finding the mass profile of the cluster. Jee et al. (2007) noted that the X-ray surface brightness from *Chandra* is better fitted by two isothermal beta models, suggesting that possibly one could be seeing two systems that are along the same line of sight.

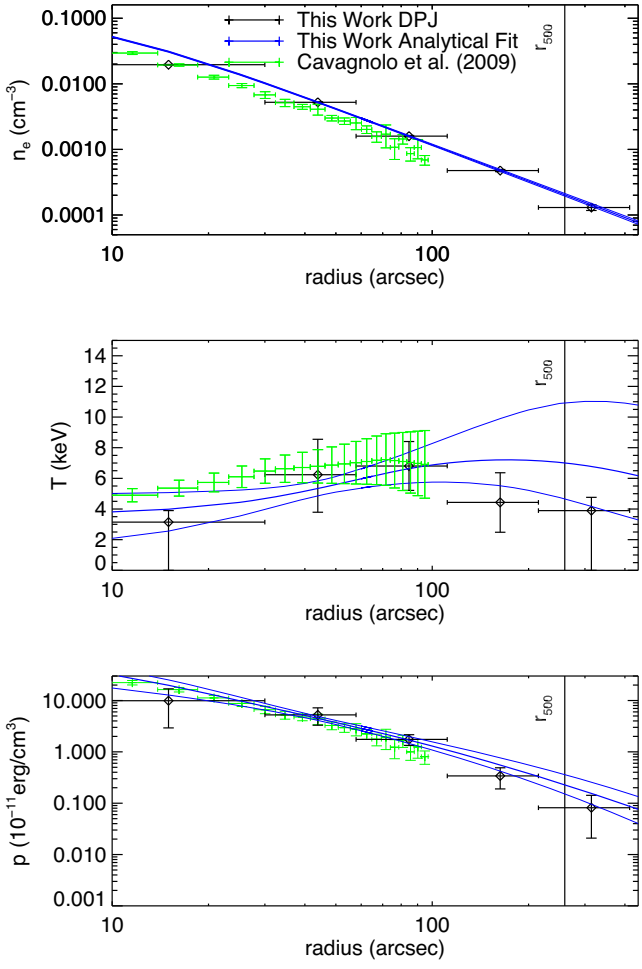

Figure B19. *MACS J1532.9+3021*. Donahue et al. (2014) obtained temperature profiles from X-ray spectroscopy (*XMM–Newton* and *Chandra*) with the temperature profile showing a central value of 3–4keV before rising to 8 keV at larger radii, consistent with our analysis. The *XMM–Newton* profile decreased down to ∼4keV at 900 kpc (∼180 arcsec), while the *Chandra* profile does not show the temperature decrease, instead plateauing at ∼9 keV. Hlavacek-Larrondo et al. (2013) performed a *Chandra*, *XMM–Newton*, VLA, and *Hubble* analysis. They observed evidence of AGN feedback, a cold front, and X-ray cavities. They note a difference in the temperature map from the east and the west side of the cluster, and find a central temperature of 4 keV rising to 9 keV at 250 kpc (∼50 arcsec). They also detect slight differences in the temperature profile at small radii (<25 arcsec) in different directions, with higher temperatures in the S and W directions.

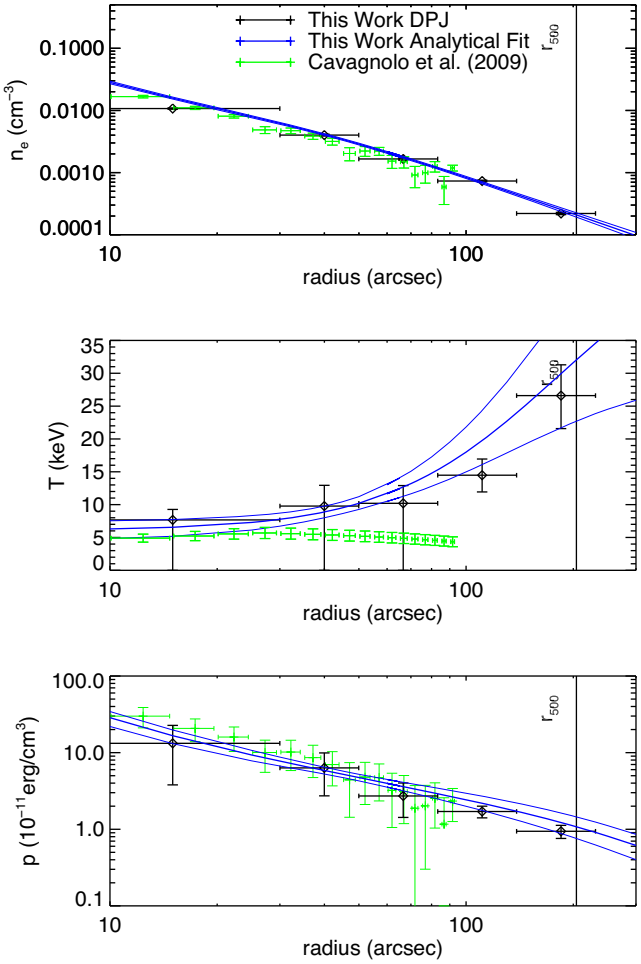

Figure B20. *MACS J0429.6−0253.* Our analysis indicates a temperature increase at large radii that is not seen in the ACCEPT results, and our smooth parametric fits indicate a drop in temperature towards the core at a significance of $\sim 2\sigma$. Donahue et al. (2014) found temperature profiles using X-ray spectroscopy from *XMM–Newton* and *Chandra*, with the temperature profile showing a central temperature of 4 keV and a peak of 9 keV at 200 kpc (40 arcsec), roughly consistent with our results over the same range.

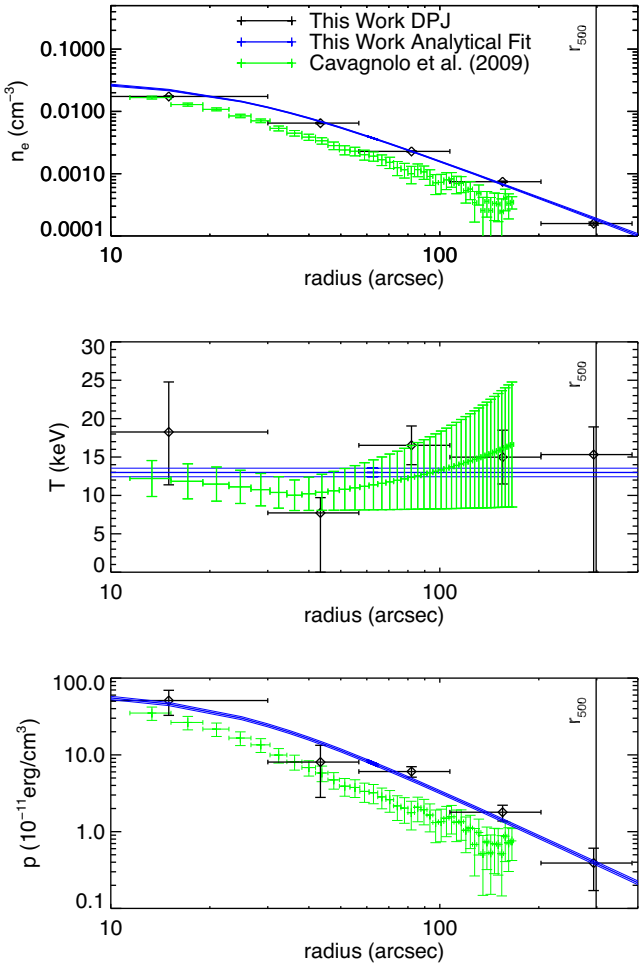

Figure B21. *MACS J2211.7−0349.* Our densities and pressures are systematically and significantly higher than those found in the ACCEPT study. Due to the lack of independent results for this cluster, it is not possible to determine which analysis may be in error.

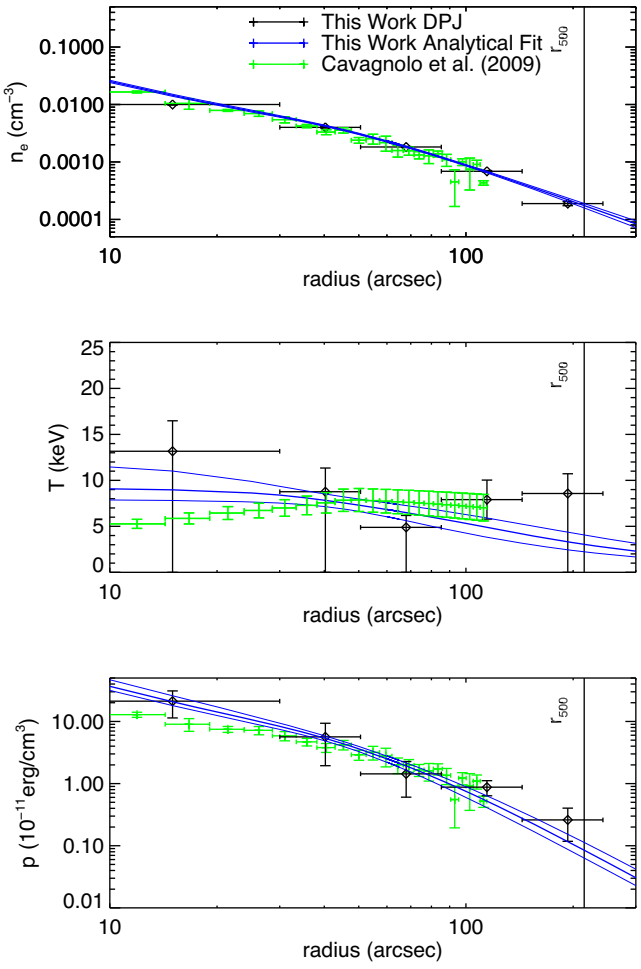

Figure B22. *MACS J1720.3+3536.* Our data indicate a decrease in the temperature in the outskirts at a significance of 6.5σ. Donahue et al. (2014) obtained temperature profiles using X-ray spectroscopy from *XMM–Newton* and *Chandra*, and found that the temperature profiles from the two instrument have different shapes. Both have a central temperature of ∼3.5 keV. *XMM–Newton* jumps to 10 keV, then slowly decreases down to ∼2 keV at 900 kpc (170 arcsec), consistent with our results outside of the core region. In contrast, *Chandra* slowly reaches 10 keV but then drops down to temperatures close to zero around 400 kpc (70 arcsec). Essentially, the outer temperature slope is steeper for *Chandra*, but the inner temperature slope is steeper for *XMM–Newton*. Maughan et al. (2008) used *Chandra* spectroscopy to obtain an isothermal temperature of ∼6.1 keV for radii $<r_{500}$ (7.8 keV if the core region is excised), broadly consistent with our results.

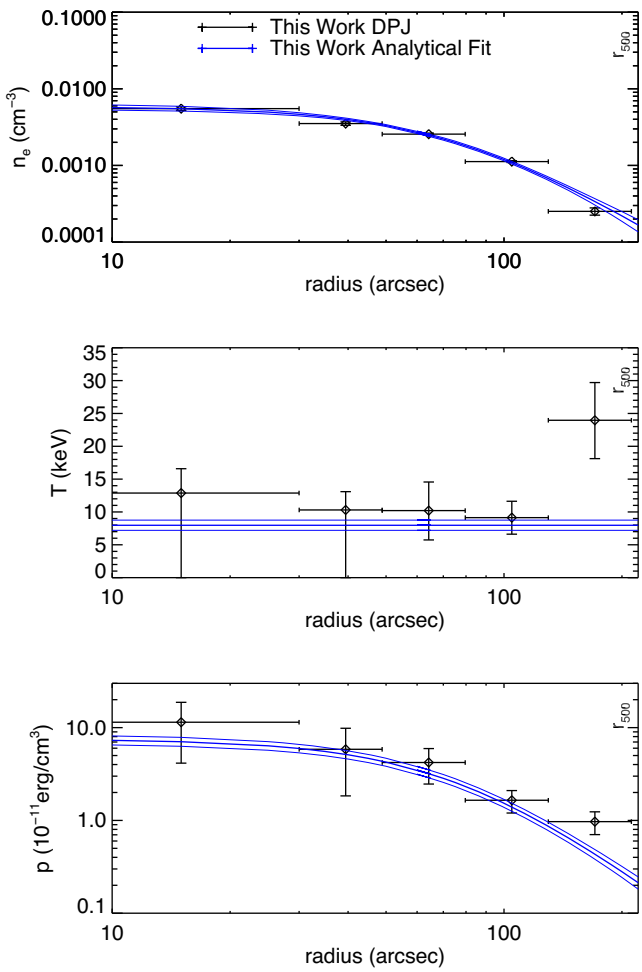

Figure B23. *MACS J0416.1−2403.* Several studies have identified this cluster as a binary merger system. Mann & Ebeling (2012), using optical and X-ray data, found this system to contain a possible binary head-on collision, just after the first collision. Jauzac et al. (2015) conducted a joint X-ray and optical study, and unveiled a large structure associated with a line-of-sight filament that could not be seen in the X-ray. A large offset in the radial velocity between two subclusters was found, and their temperatures were determined to be 10 and 13.6 keV, slightly higher than our isothermal smooth parametric fit. Ogrean et al. (2015) created temperature, pressure, and entropy maps using a multiwavelength analysis of *Chandra*, the VLA, the GMRT, and *Hubble*. The temperature map is elongated, and has a relatively high mean temperature of 10 keV. The radio halo is also elongated along the same direction.

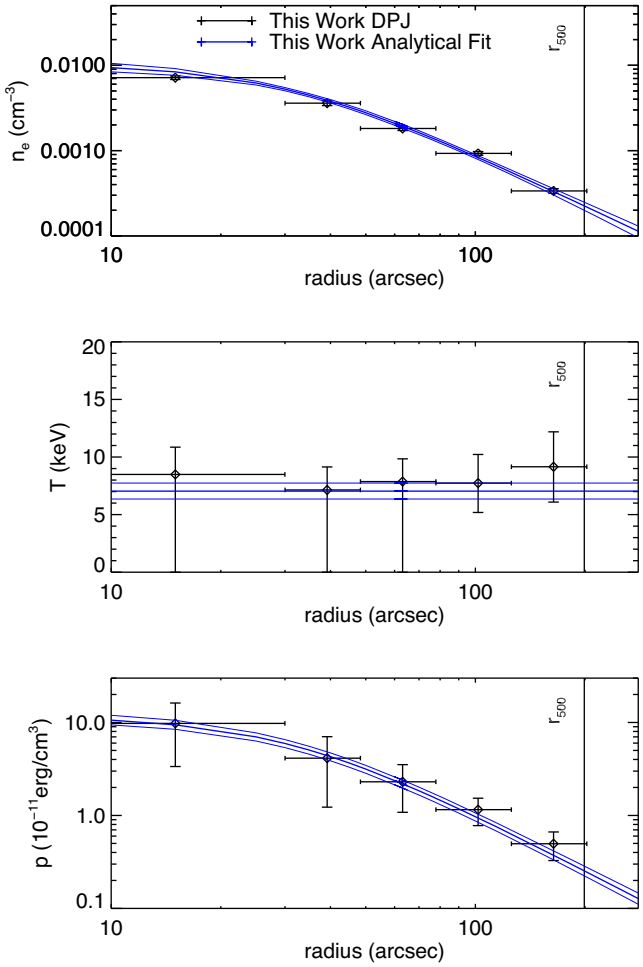

Figure B24. *MACS J0451.9+0006.* Maughan et al. (2008) used *Chandra* spectroscopy to obtain an isothermal temperature of ∼5.6 keV at radii $<r_{500}$ (4.8 keV if the central region is excised). This is somewhat lower, but reasonably consistent with, the approximately isothermal profile found in our analysis. Mann & Ebeling (2012) found this cluster to have highly irregular morphology, but it was not classified as an extreme or active merger due to its small brightest cluster galaxy (BCG)-X-ray peak and BCG-X-ray centre separations.

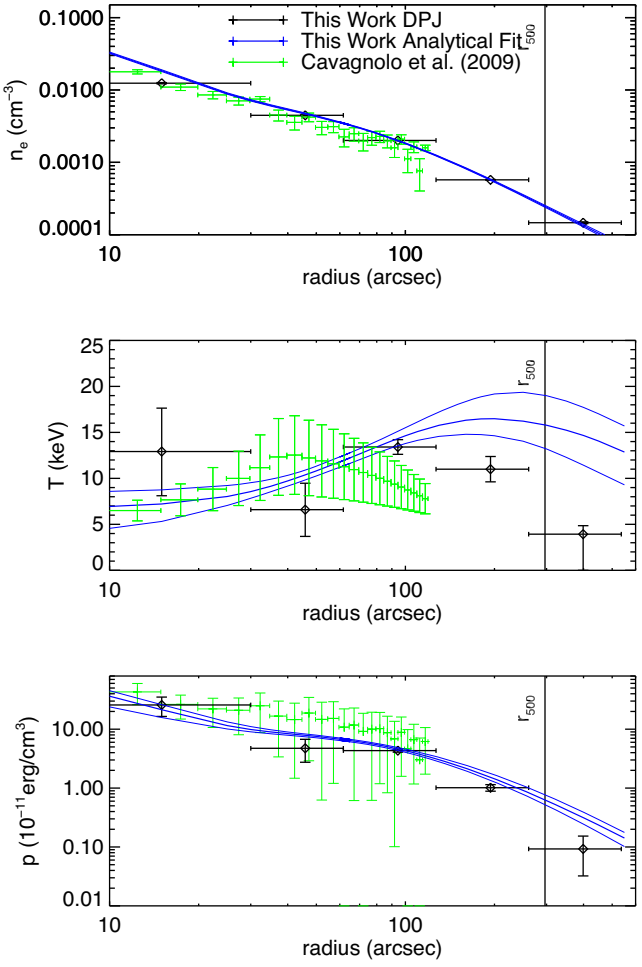

Figure B25. *MACS J0417.5−1154.* From our smooth parametric fits, we detect a cool core at a significance of 3.3σ. Mann & Ebeling (2012) identified this cluster as a primary candidate for a binary, head-on-collision type merger: The X-ray core aligns with one of two optical cores, but the X-ray emission bleeds into the outskirts and meets with the second of the optical cores.

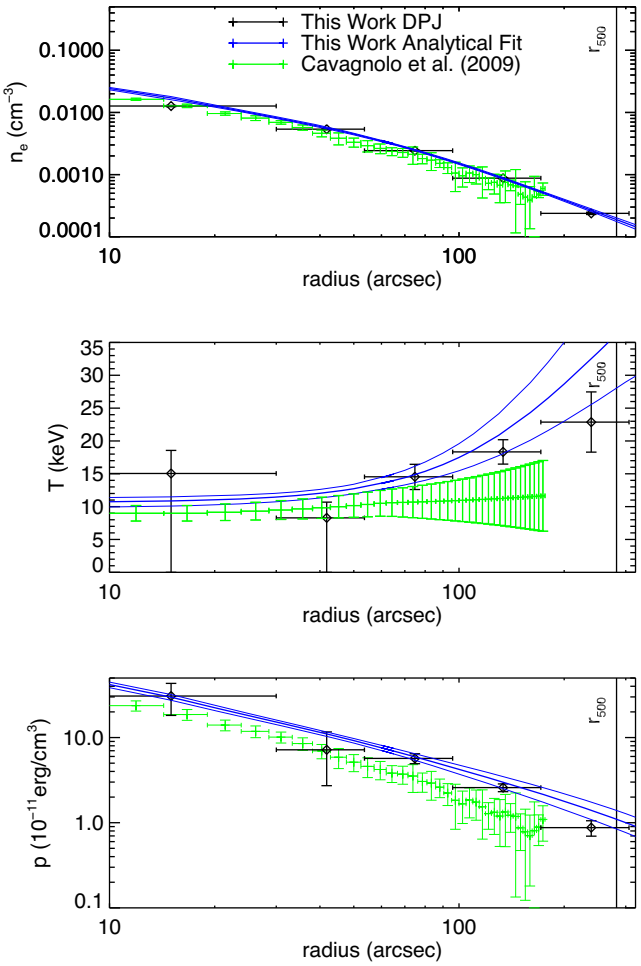

Figure B26. *MACS J1206.2−0847.* Our smooth parametric fits indicate a drop in temperature near the core at a significance of 2.3σ. Donahue et al. (2014) obtained temperature profiles using X-ray spectroscopy from *XMM–Newton* and *Chandra*. The *Chandra* profile has a large temperature peak in the centre (15 keV), dropping to a nearly isothermal profile of 10 keV to the maximum radius probed by the data (1000 kpc or 180 arcsec). The *XMM–Newton* profile, on the other hand, has a cool core of ∼7 keV, which increases with radius to 10 keV before dropping to 5 keV in the outskirts. Our analysis is consistent with these results at intermediate radii, but we find an approximately isothermal profile into the core and a slight temperature increase at large radii. Several studies, using X-ray, optical, and/or lensing data, have found this cluster to be relaxed (Gilmour, Best & Almaini 2009; Mann & Ebeling 2012; Umetsu et al. 2012).

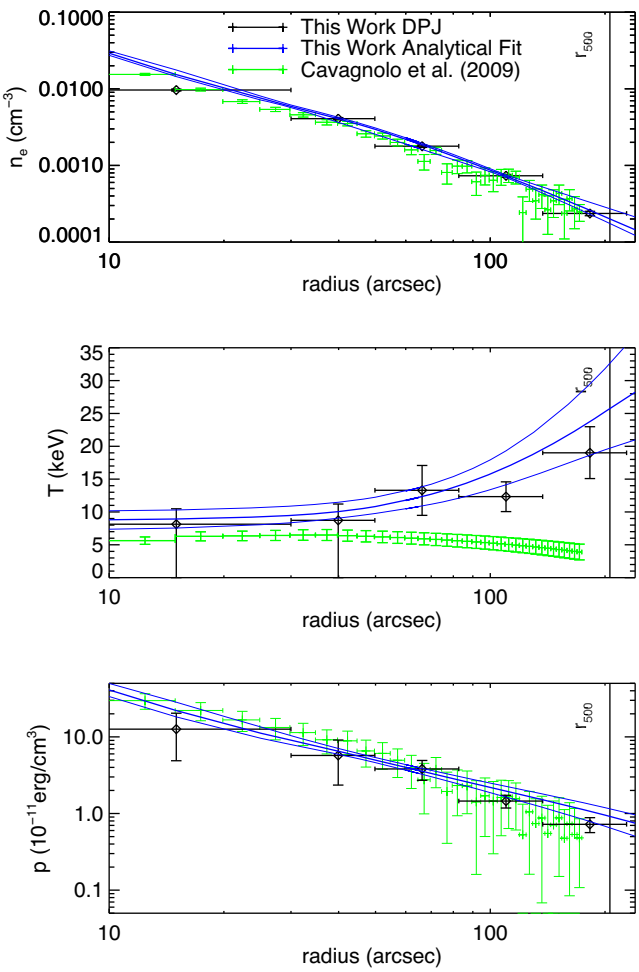

Figure B27. *MACS J0329.6−0211.* Our smooth parametric fit finds a temperature drop in the core at modest significance (2.1σ). Compared to that of ACCEPT, our temperature profile is notably higher outside of the core region. Maughan et al. (2008) found a temperature of 4.5 keV for $r < r_{500}$, and 4.4 keV for radii within $0.15 < r < 1r_{500}$, in good agreement with the ACCEPT results. Mann & Ebeling (2012) found this to be a relaxed cluster according to X-ray and optical alignment. Kotov & Vikhlinin (2006), using *Chandra* and *XMM–Newton* data, found this cluster to follow a standard cool-core temperature profile, except for a dip in temperature at intermediate radii (around 100 kpc), which could hint at some substructure. Giacintucci et al. (2014) found a possible radio minihalo centred in the cluster using VLA data, filling out much of the core to 150 kpc.

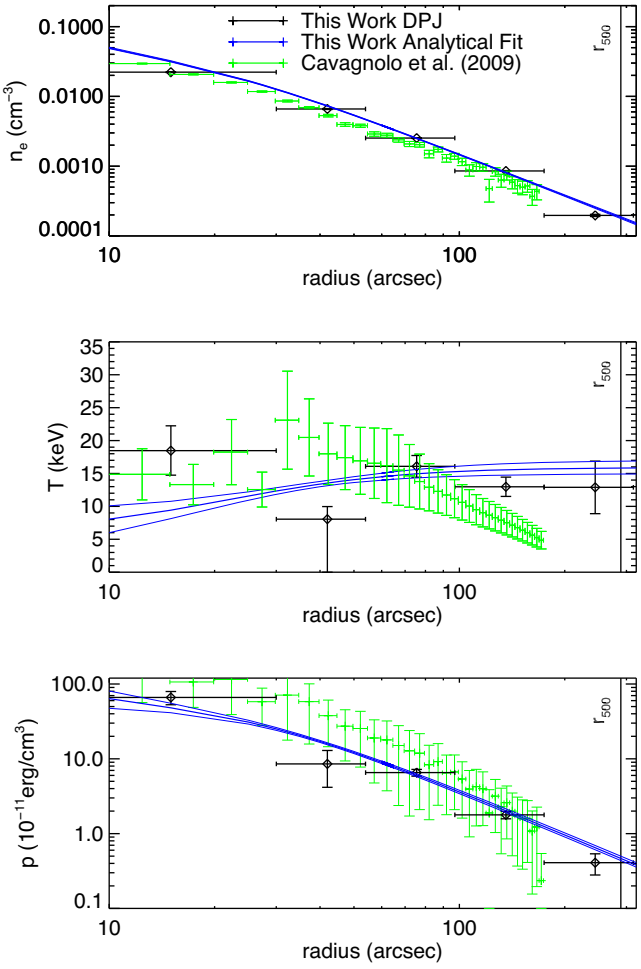

Figure B28. *MACS J1347.5−1144.* We detect a cool core in our smooth parametric fit at a significance of 3.1σ, but we do not find strong evidence for a temperature drop in the outskirts. Compared to the ACCEPT results, our temperature is somewhat higher at large radii. Donahue et al. (2014) obtained temperature profiles with a central temperature of 5 keV, with a peak of 17 keV that decreases in the outskirts, in good agreement with the ACCEPT results. Maughan et al. (2008) used *Chandra* imaging and spectra and assumed isothermal profiles, finding 12.2 keV for $r < r_{500}$, and 11.7 keV for $0.15 < r < 1r_{500}$, roughly consistent with our profiles. Lu et al. (2010) studied this cluster using the optical waveband, and found a possible filament between a cluster 7 Mpc away. This cluster has many SZ-focused studies devoted to it. Ferrari et al. (2011) compared radio GMRT data with MUSTANG, *Chandra*, and *XMM–Newton* X-ray data and found a correlation between the intracluster radio emission and X-ray and SZ emission. Korngut et al. (2011) made a high-resolution SZ map using MUSTANG and were able to find substructure 20 arcsec from the centre in the form of gas that has been heated through shocks caused by mergers. Ferrari et al. (2011) combined X-ray and SZ data to study the cluster, finding substructure near the core and very hot gas in the cluster up to 20 keV without the use of X-ray spectroscopy. Komatsu et al. (2001) mapped the SZ signal at 150 GHz with 13 arcsec resolution using the Nobeyama telescope, and detected the excess SZ emission at 20 arcsec. Pointecouteau et al. (2001) on the other hand, made a similarly resolved map, and could not constrain substructure, although they did observe that the signal was not completely spherical. Most recently, Sayers et al. (2016) were able to place an upper limit on the amplitude of the peculiar velocity of the cluster using five-band SZ measurements.

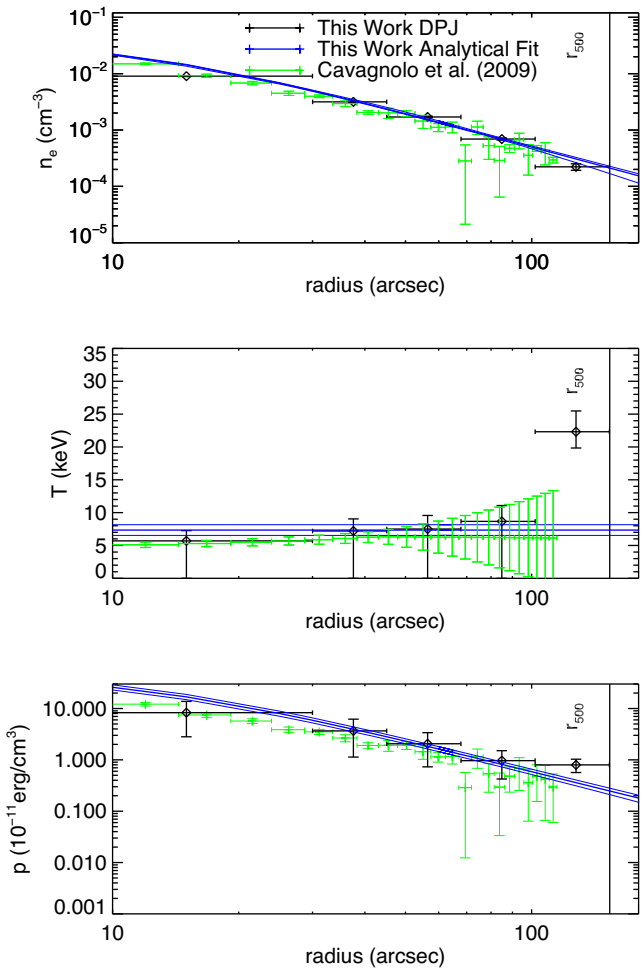

Figure B29. *MACS J1311.0−0310.*

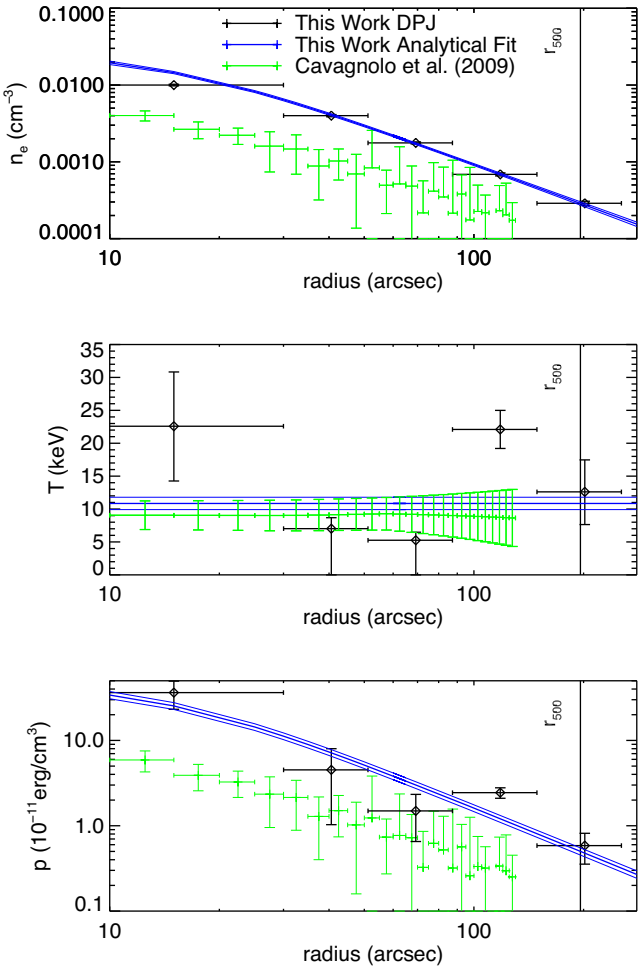

Figure B30. *MACS J0257.1−2325.* The ACCEPT density profile is significantly lower compared to our and other results (Amodeo et al. 2016). Through the optical, Kartaltepe et al. (2008) found that, on large scales, this system has filaments directed into the cluster.

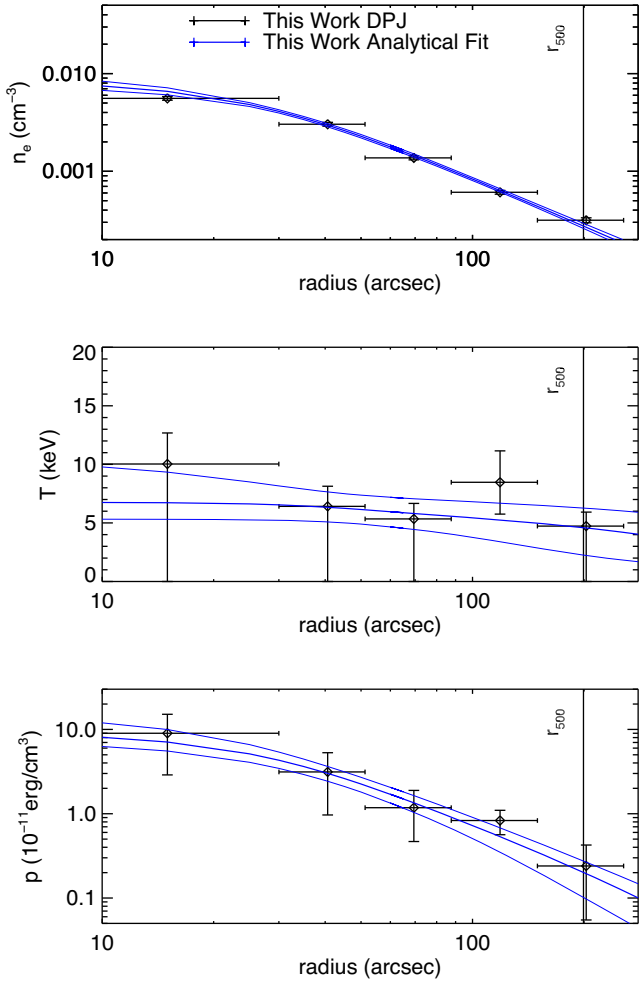

Figure B31. *MACS J0911.2+1746.* Kartaltepe et al. (2008), using optical data, found this cluster consists of two subclusters with different masses separated by 1 Mpc. The X-ray centroid was found to be significantly offset from the galaxy surface density for the smaller subcluster, suggesting that this system has undergone a recent merger.

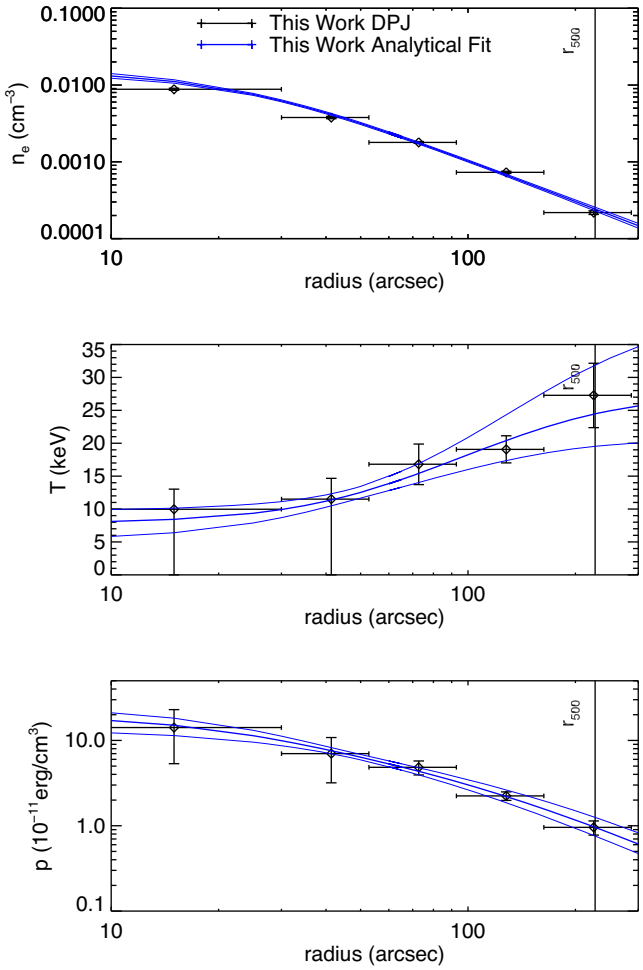

Figure B32. *MACS J2214.9−1359.* The ACCEPT density profile is systematically lower than both ours and that of two other analyses (Bonamente et al. 2006; Amodeo et al. 2016). Our smooth parametric fits indicate a temperature drop in the centre at a significance of 2.2σ. Mann & Ebeling (2012) found this cluster to have the most relaxed morphological denotation, with a prominent cool core and perfect alignment between the X-ray peak and BCG.

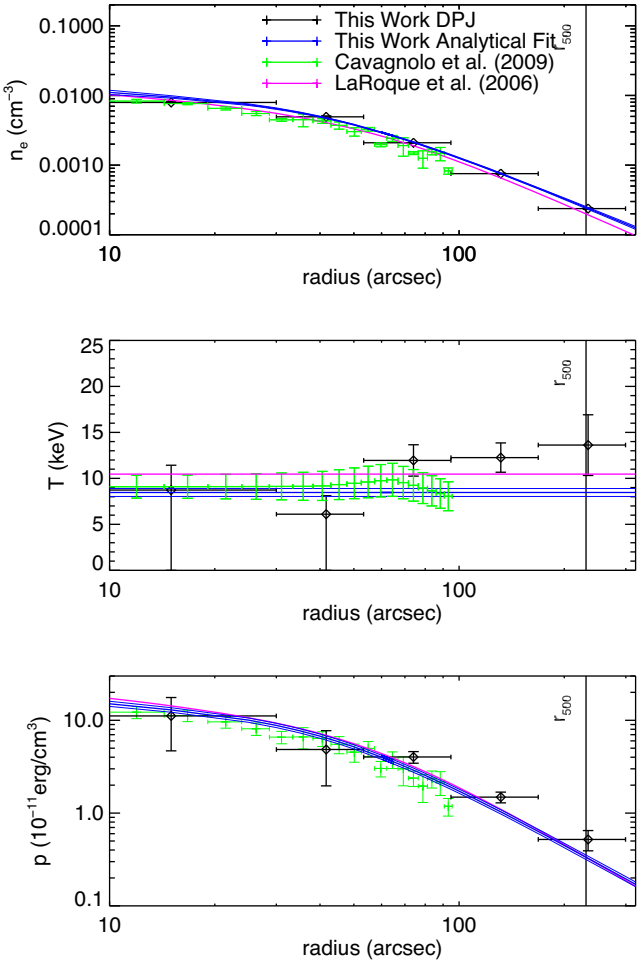

Figure B33. *MACS J0018.5+1626.* The profiles we obtain for this cluster are in excellent agreement with the LaRoque et al. (2006) results. Several studies have found this cluster to be relaxed (e.g. Kotov & Vikhlinin 2005), however, Solovyeva et al. (2007) found evidence for it to be undergoing a merger near the centre of the cluster using *XMM-Newton* observations. They also found a temperature profile out to r_{200}, showing a clear decrease in the outskirts, to 4 keV, which does not match the approximately isothermal profile found in our analysis. Worrall & Birkinshaw (2003) found no evidence of a cool core, but they did find evidence for a merger in the centre of the cluster due to the non-spherical X-ray shape in that region. Overall, they find an isothermal temperature of ∼9.13 keV, consistent with our results.

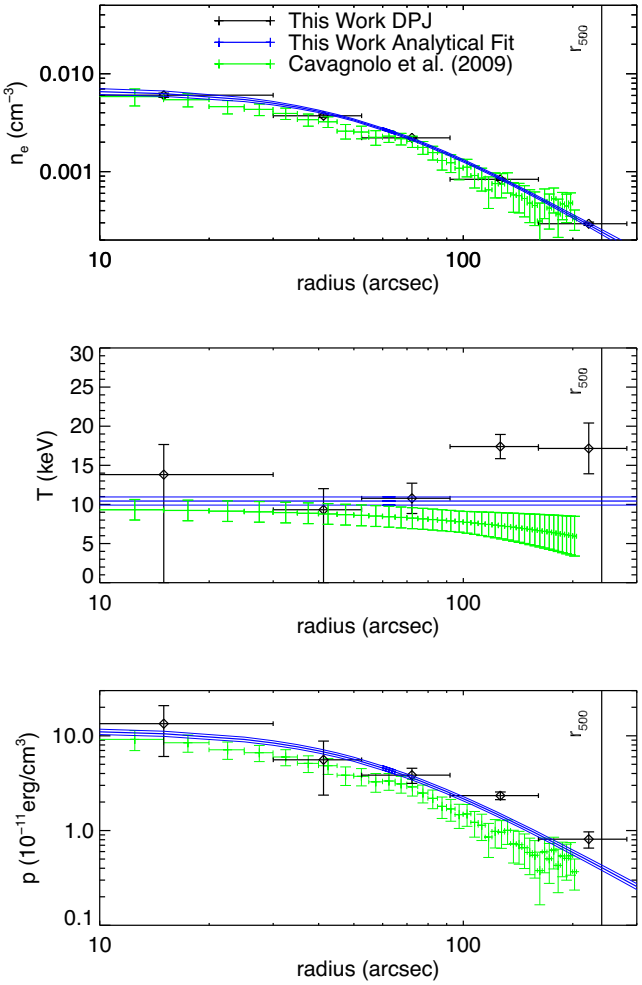

Figure B34. *MACS J1149.5+2223.* Our deprojection indicates a somewhat higher temperature at large radii compared to that of ACCEPT. This massive cluster has been widely studied through gravitational lensing. Using *Hubble* data, Mohammed et al. (2016) constrained the mass distribution of this cluster and found several main peaks and clear non-sphericity, suggesting this is a merging cluster.

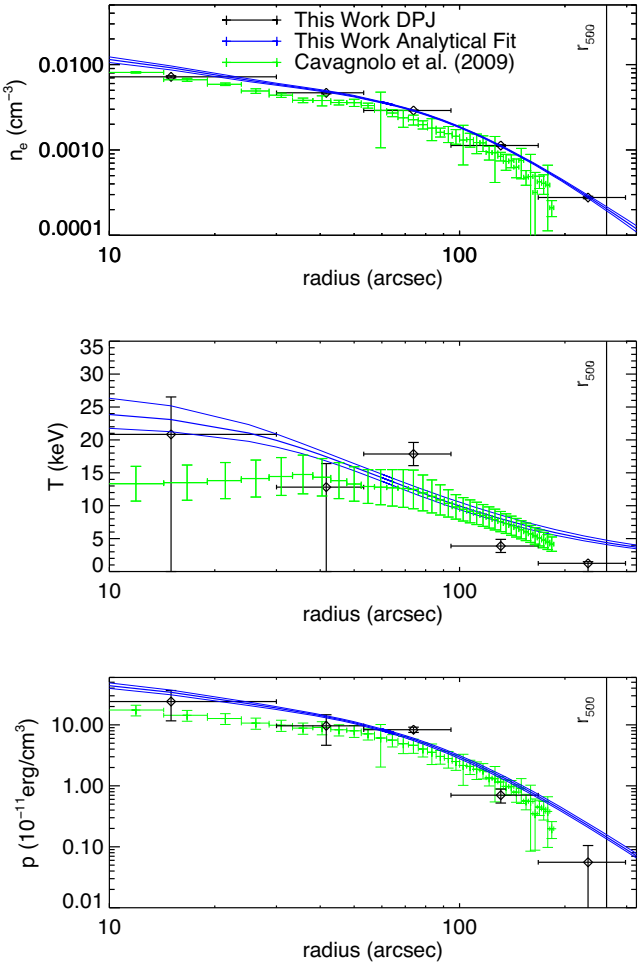

Figure B35. *MACS J0717.5+3745.* Our smooth parametric fit indicates a temperature drop at large radii at a significance of 24σ. This cluster has been studied extensively in different wavelengths. Ma, Ebeling & Barrett (2009) found that the cluster consists of four large subclusters based on X-ray imaging and galaxy positions. Through lensing (Medezinski et al. 2013; Diego et al. 2015; Limousin et al. 2016; Umetsu et al. 2016), four large masses are also clearly found, reflecting that this cluster is a complex merger. Mroczkowski et al. (2012) studied this cluster through the SZ effect and X-ray and lensing observations. They also found very hot gas near 30 keV in some regions of the cluster. A large kSZ signal in one of the subclusters, which has not been accounted for in our analysis, could potentially be a source of bias in our results (Sayers et al. 2013c).

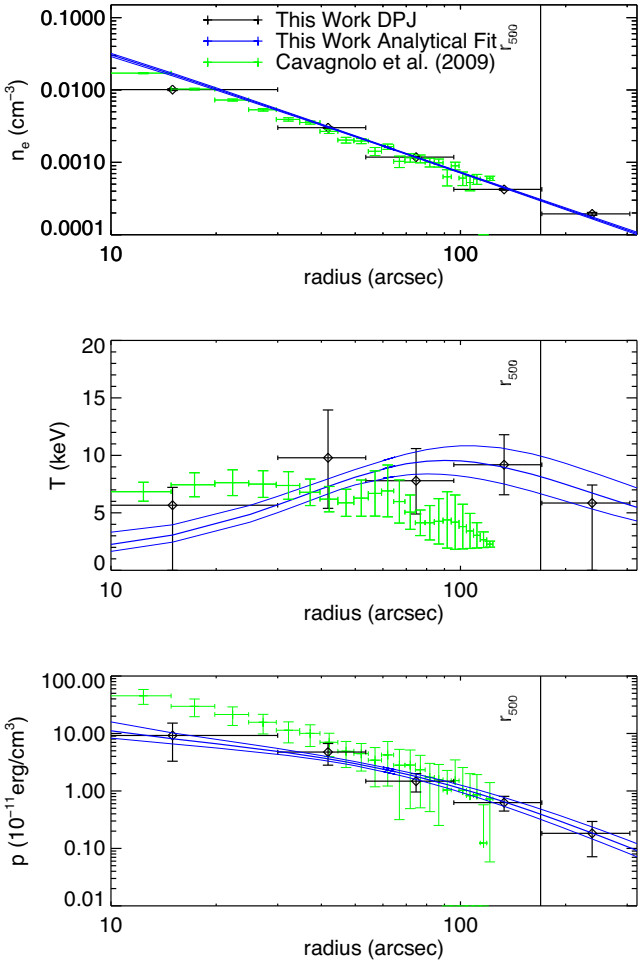

Figure B36. *MACS J1423.8+2404.* Our profile fit detects a cool core at a significance of 3.3σ. Adam et al. (2016) conducted a multiwavelength analysis of the cluster, including X-ray surface brightness and spectroscopy and high-resolution SZ data to jointly constrain smooth ICM profiles that are in good agreement with our results. Kotov & Vikhlinin (2006) used *Chandra* X-ray spectroscopy to constrain the temperature profile, which is again consistent with our results. Morandi, Pedersen & Limousin (2010) used *Chandra* data and found a cool core (3 keV core and 7 keV peak at 300 kpc), again in good agreement with our fits. Based on lensing measurements, this cluster has been found to be slightly elongated and relaxed, with little substructure (Limousin et al. 2010; Zitrin et al. 2011).

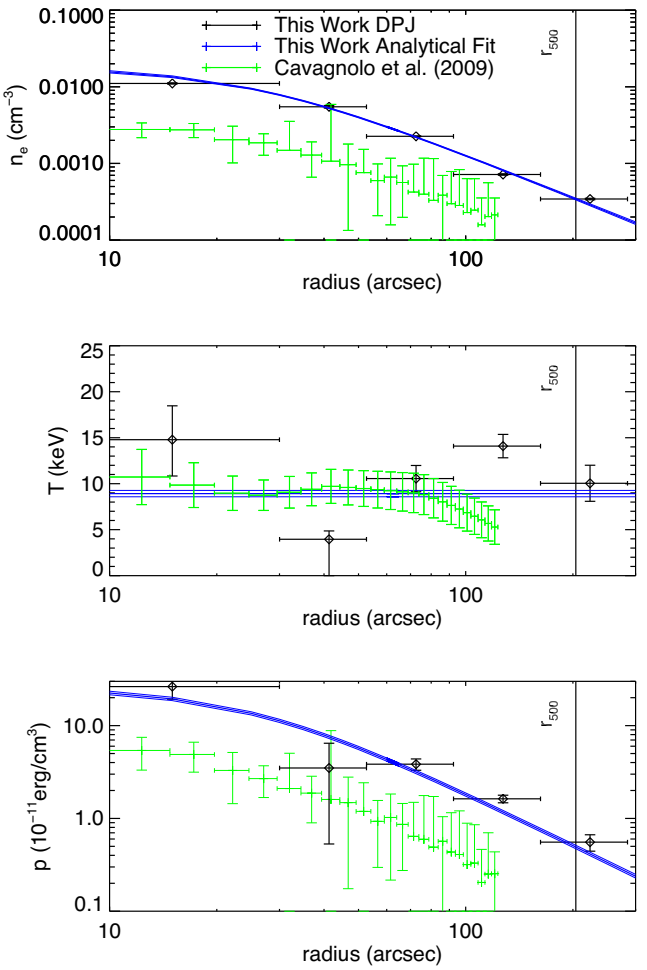

Figure B37. *MACS J0454.1−0300.* The densities from the ACCEPT analysis are systematically lower than ours. However, the ACCEPT results are also inconsistent with two other analyses (Bonamente et al. 2006; Amodeo et al. 2016). Donahue et al. (2003) used *Chandra* X-ray spectroscopy to obtain an isothermal temperature of 10.2 keV, consistent with our results. They also found an elliptical cluster morphology, and a shift in the BCG location and X-ray centroid.

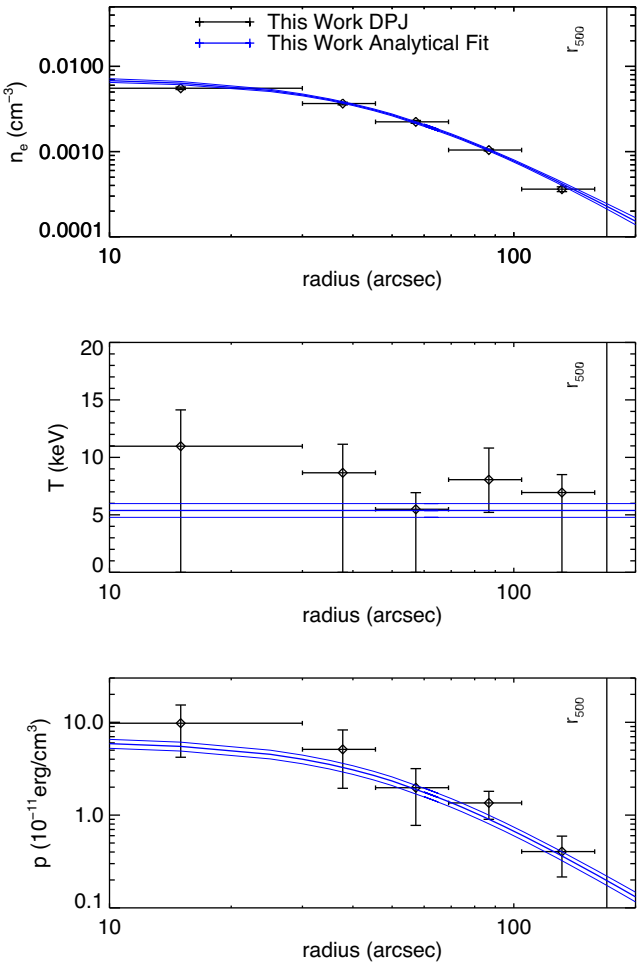

Figure B38. *MACS J0025.4−1222.* Although this cluster is classified as non-disturbed in our analysis, two other studies find that it is clearly a major merger between two clusters of similar masses (Bradač et al. 2008; Kartaltepe et al. 2008). Furthermore, Bradač et al. (2008) found that the cluster total mass distribution is not consistent with the gas distribution.

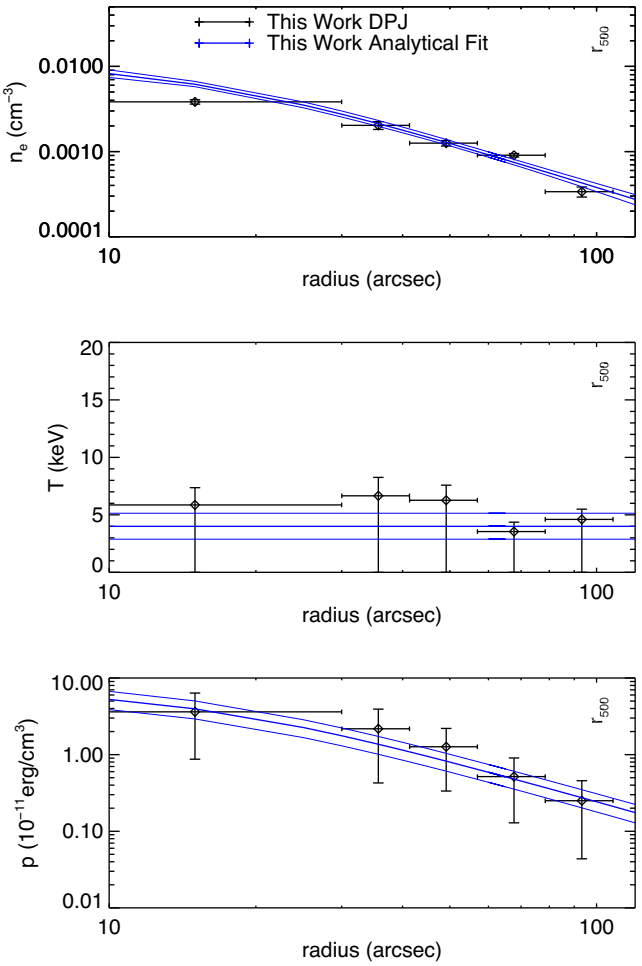

Figure B39. *MS 2053.7−0449.* This is the least massive cluster in our sample, with $M_{500} \approx 3 \times 10^{14}\,\mathrm{M}_{\odot}$, and one of the dimmest clusters in the SZ. The low mass and high redshift also produce a weak X-ray signal. This makes it one of the few clusters in our analysis where the constrains do not extend to r_{500}. Verdugo, de Diego & Limousin (2007) found a bimodal and elongated mass distribution for this cluster using *Hubble* data, indicating a merger.

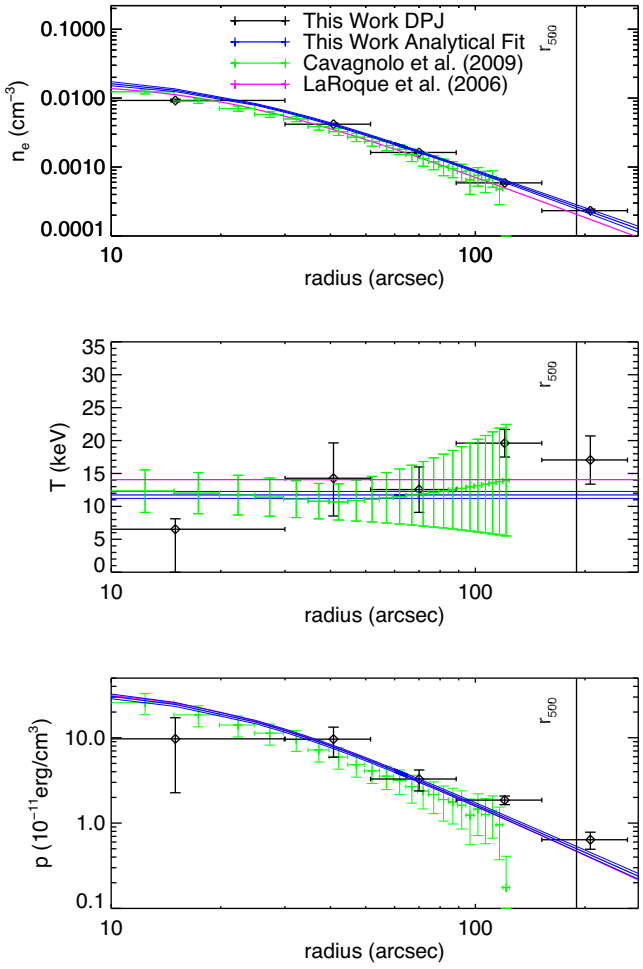

Figure B40. *MACS J0647.7+7015.* Although our smooth parametric density profile shows a statistically significant offset from the LaRoque et al. (2006) results, the absolute magnitude of the offset is modest.

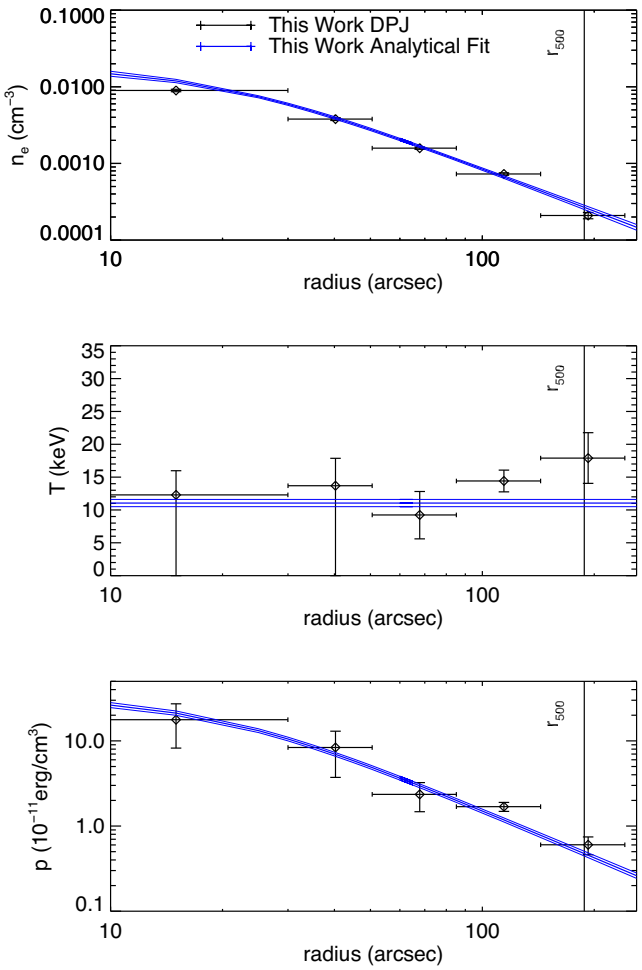

Figure B41. *MACS J2129.4−0741.* Mann & Ebeling (2012) conducted a classification of clusters based on morphology, using a combination of X-ray and optical data. For this cluster they deduced it was a merger because the X-ray centroid location is significantly different from the BCG's.

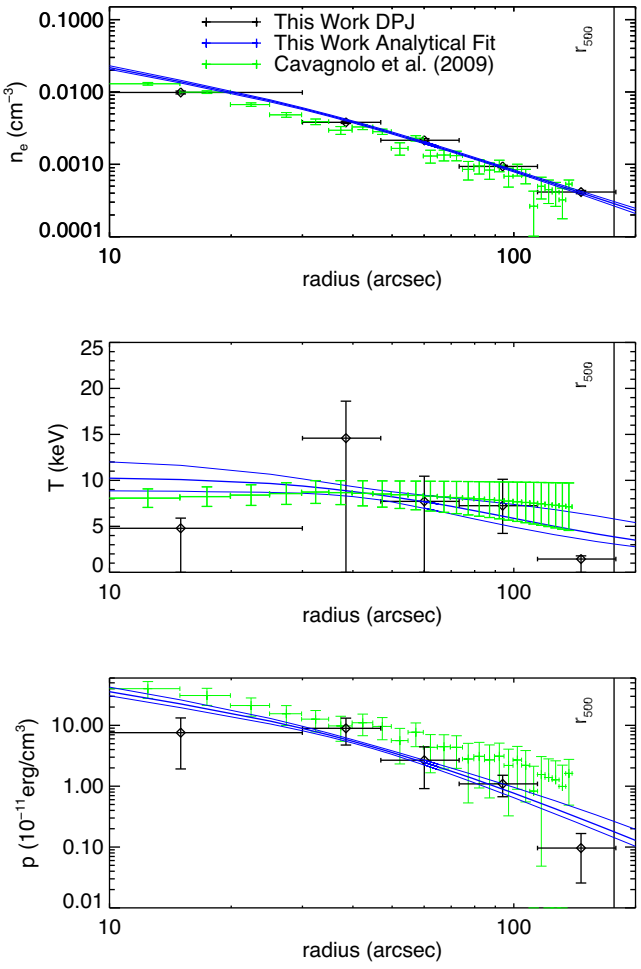

Figure B42. *MACS J0744.8+3927.* LaRoque et al. (2003) studied this cluster using OVRO/BIMA and found an average temperature of 17.9 keV, significantly higher than our results. Korngut et al. (2011) studied this cluster through the high-resolution SZ images from MUSTANG, and compared it with X-ray data, finding evidence of a merger-related shock front.

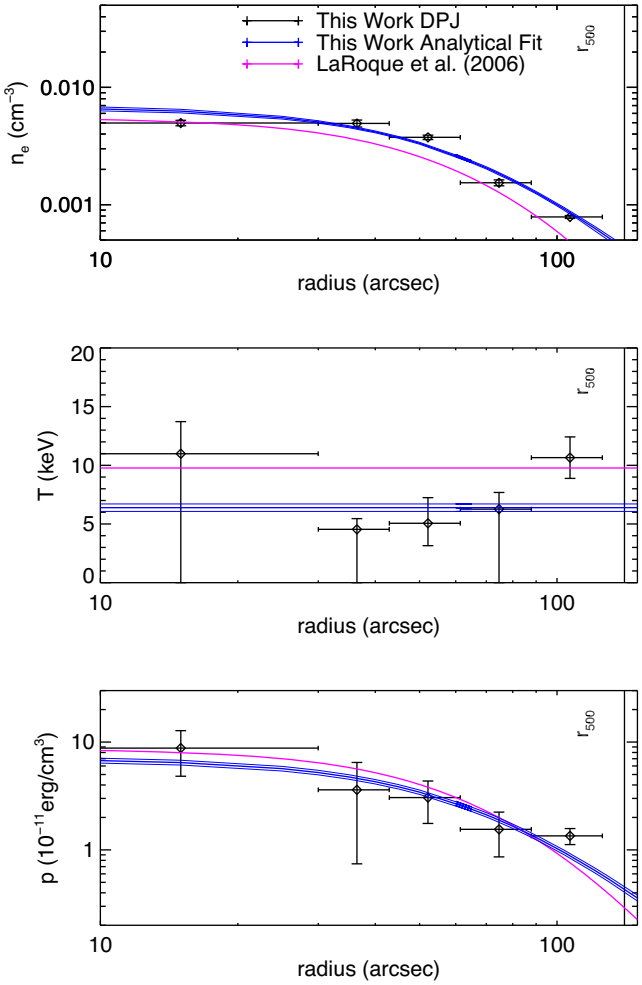

Figure B43. *MS 1054.4−0321.* Compared to the smooth parametric fits of LaRoque et al. (2006), our smooth parametric fits show a significant offset in both density and temperature. Gioia et al. (2004) used *XMM–Newton* to find an average temperature of ∼7keV, in good agreement with our results. Neumann & Arnaud (2000) studied this cluster using the X-ray (*ROSAT*), finding substructure and other signs of recent merging processes (e.g. BCG and X-ray peak offset, X-ray centroid and peak offset).

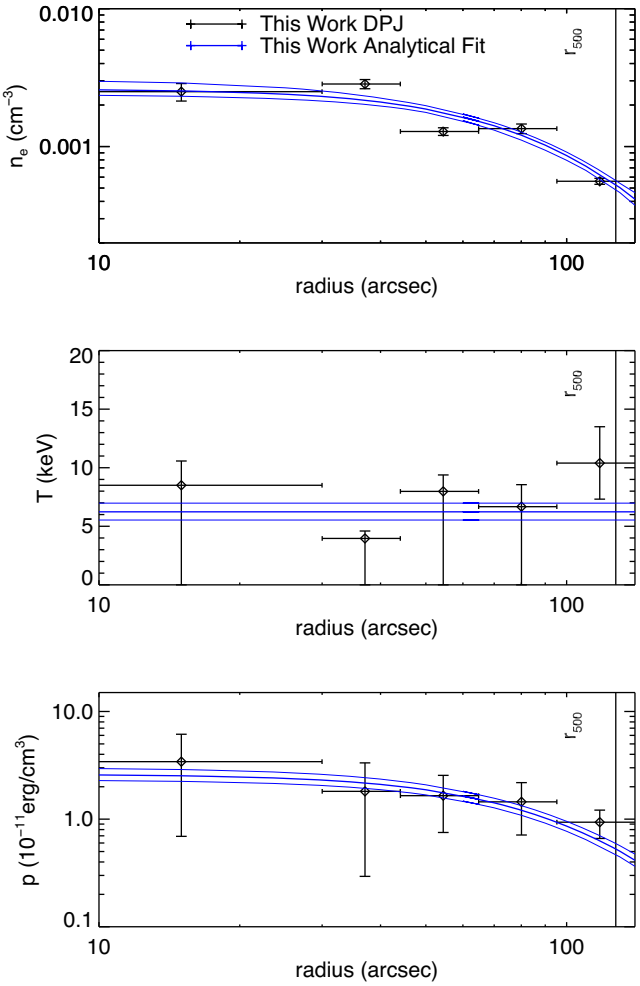

Figure B44. *CL J0152.7−1357.* The irregular shape of our deprojected density profile is possibly due to the disturbed nature of the cluster. Several studies found evidence of subclusters and of merging based on X-ray and optical subclusters (Huo et al. 2004), a high velocity dispersion of galaxy cluster members (Girardi et al. 2005), and an offset between the X-ray and SZ emission peaks (Massardi et al. 2010). Maughan et al. (2006) used *XMM–Newton* to study the X-ray emission distribution in detail, finding many substructures and smaller groups, concluding that the cluster has recently undergone many mergers.

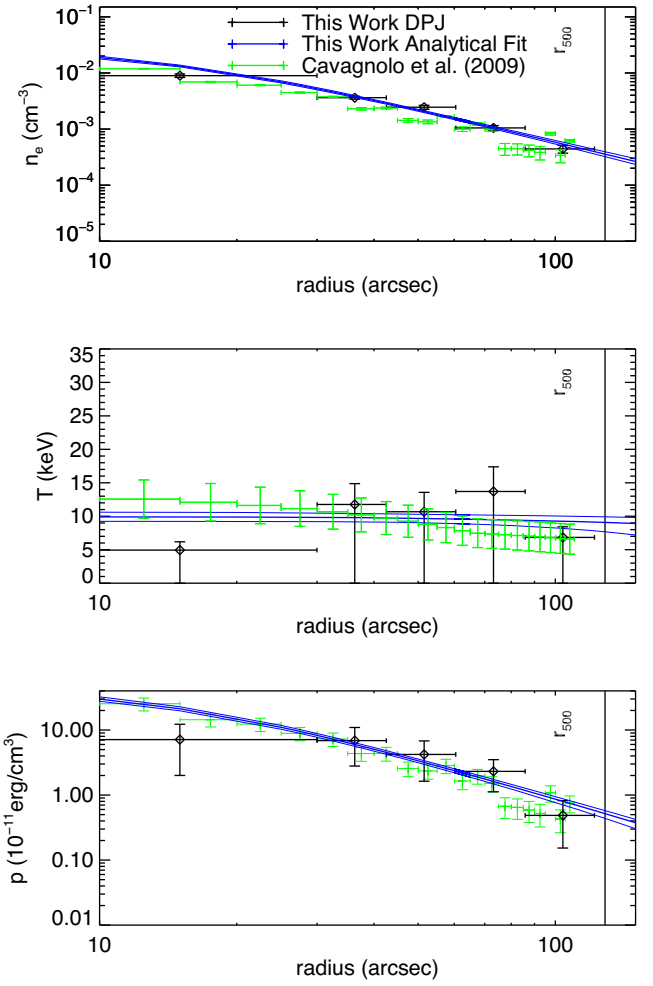

Figure B45. *CL J1226.9+3332.* Although this cluster is classified as non-disturbed in our analysis, several other works have found evidence of merging through X-ray temperature map asymmetries (Maughan et al. 2007), subclumps through weak lensing (Jee & Tyson 2009), and multiple peaks in the SZ through high-resolution MUSTANG maps (Korngut et al. 2011).

This paper has been typeset from a TEX/LATEX file prepared by the author.